A Volumetric Contact Model for Planetary Rover Wheel/Soil Interaction

by

Willem Petersen

A thesis
presented to the University of Waterloo
in fulfillment of the
thesis requirement for the degree of
Doctor of Philosophy
in
Systems Design Engineering

Waterloo, Ontario, Canada, 2012

I hereby declare that I am the sole author of this thesis. This is a true copy of the thesis, including any required final revisions, as accepted by my examiners.

I understand that my thesis may be made electronically available to the public.

Abstract

The main objective of this research is the development of a volumetric wheel-soil ground contact model that is suitable for mobile robotics applications with a focus on efficient simulations of planetary rover wheels operating on compliant and irregular terrains. To model the interaction between a rover wheel and soft soil for use in multibody dynamic simualtions, the terrain material is commonly represented by a soil continuum that deforms substantially when in contact with the locomotion system of the rover. Due to this extensive deformation and the large size of the contact patch, a distributed representation of the contact forces is necessary. This requires time-consuming integration processes to solve for the contact forces and moments during simulation.

In this work, a novel approach is used to represent these contact reactions based on the properties of the hypervolume of penetration, which is defined by the intersection of the wheel and the terrain. This approach is based on a foundation of springs for which the normal contact force can be calculated by integrating the spring deflections over the contact patch. In the case of an elastic foundation, this integration results in a linear relationship between the normal force and the penetration volume, with the foundation stiffness as the proportionality factor. However, due to the highly nonlinear material properties of the soft terrain, a hyperelastic foundation has to be considered and the normal contact force becomes proportional to a volume with a fractional dimension — a hypervolume. The continuous soil models commonly used in terramechanics simulations can be used in the derivation of the hypervolumetric contact forces. The result is a closed-form solution for the contact forces between a planetary rover wheel and the soft soil, where all the information provided by a distributed load is stored in the hypervolume of interpenetration.

The proposed approach is applied to simulations of rigid and flexible planetary rover wheels. In both cases, the plastic behaviour of the terrain material is the main source of energy loss during the operation of planetary rovers. For the rigid wheel model, a penetration geometry is proposed to capture the nonlinear dissipative properties of the soil. The centroid of the hypervolume based on this geometry then allows for the calculation of the contact normal that defines the compaction resistance of the soil. For the flexible wheel model, the deformed state of the tire has to be determined before applying the hypervolumetric contact model. The tire deformation is represented by a distributed parameter model based on the Euler-Bernoulli beam equations.

There are several geometric and soil parameters that are required to fully define the normal contact force. While the geometric parameters can be measured, the soil parameters have to be obtained experimentally. The results of a drawbar pull experiment with the Juno rover from the Canadian Space Agency were used to identify the soil parameters. These parameters were then used in a forward dynamics simulation of the rover on an irregular 3-dimensional terrain. Comparison of the simulation results with the experimental data validated the planetary rover wheel model developed in this work.

Acknowledgements

I would like to express my gratitude to my PhD supervisor, Prof. John McPhee, whose guidance and expertise contributed considerably to my experiences as a grad student. I appreciate his technical and professional support and his assistance in writing this thesis and many other documents.

I would also like to acknowledge my readers Dr. Chad Schmitke, Prof. Gordon Savage, Prof. Amir Khajepour, and Prof. József Kövecses who kindly agreed to be on the examining committee.

I wish to thank Dr. Yves Gonthier from the Canadian Space Agency who not only helped in establishing this project but also assisted this research through technical support.

Thanks also goes out to all my fellow MoRG members. Especially the guys and the girl of the Systems Design Lab, who have helped enrich the experience of my graduating program.

I would like to acknowledge the Canadian Space Agency and the Natural Sciences and Engineering Research Council of Canada for funding this project and for providing the necessary equipment and expertise to realize the research.

I would also like to thank my family for the support they provided me through my life. Lastly, and most importantly, I must thank my wife, Roop, without whose support, encouragement and editing assistance, I would not have finished this thesis.

Table of Contents

List of Tables

List of Figures

Nomenclature

Functions and Scalars

a_0 and a_1	Curve-fit parameters of hypervolume coefficient function
A	Cross section area of tire tread $[m^2]$
A_1	Slope parameter of hypervolume coefficient function
b	Wheel width $[m]$
c	Soil cohesion $[kPa]$
$c_v\,(V)$	Hypervolume coefficient function $[m^{\eta-1}]$
C_f	Non-dimensional foundation damping factor
D	Wheel diameter $[m]$
E	Young's modulus of wheel $[N/m^2]$
f_S	Deformation at a point on the contact surface $\mathbf{S}$ $[m]$
f_n	Normal contact force $[N/m]$
f_t	Tangential contact force $[N/m]$
f_X	Contact force in X-dir $[N/m]$
f_Y	Contact force in Y-dir $[N/m]$
F_{hX}	External wheel hub force in X-dir $[N]$
F_{hZ}	External wheel hub force in Y-dir $[N]$
F_{trac}	Wheel/soil traction force $[N]$
F_x	Wheel/soil contact force in longitudinal direction $[N]$
F_z	Wheel/soil contact force in vertical direction $[N]$
$g(X)$	Road profile $[m]$
h	Ground profile height $[m]$
h_f	Depth of the foundation $[m]$
H	Heaviside step function
I	Second order moment of the area $[m^4]$
j_x	Shear deformation $[m]$

J	Moment of inertia of wheel $[kg\,m^2]$
k	Soil stiffness modulus $[N/m^{n+2}]$
k_{Bekker}	Combined Bekker soil stiffness modulus $[N/m^{n+2}]$
k_c	Cohesive soil stiffness modulus $[N/m^{n+1}]$
k_c'	Dimensionless frictional soil stiffness modulus
k_f	Elastic modulus of the foundation $[N/m^2]$
k_h	Hyperelastic modulus of the foundation $[N/m^{\eta+2}]$
k_{relax}	Soil stiffness modulus in relaxation $[N/m^{n+2}]$
k_V	Volumetric stiffness $[N/m^3]$
k_ϕ	Frictional soil stiffness modulus $[N/m^{n+2}]$
k_ϕ''	Dimensionless cohesive soil stiffness modulus
K	Radial spring stiffness $[N/m]$
K_x	Shear deformation modulus $[m]$
K_f	Foundation stiffness $[N/m]$
K_{v_x}	Volumetric wheel/soil traction modulus
L	Lagrangian $[Nm]$
m	Wheel diameter exponent
M	Mass of rigid wheel hub $[m]$
n	Soil sinkage exponent
p	Normal stress in wheel/soil interface $[MPa]$
Q	Generalized forces/moments $[N]/[Nm]$
res	Residual of kinematic data
R	Wheel radius $[m]$
R_c	Soil compaction resistance $[N]$
R_l	Loaded wheel radius $[m]$
S_{long}	Longitudinal wheel slip
T	Kinetic energy $[Nm]$
T_h	Driving torque $[Nm]$
T^*	Time scaling factor $[s]$
v_x	Longitudinal wheel velocity $[m/s]$
V	Potential energy $[Nm]$
V	Penetration volume of contact problem $[m^3]$
V_h	Penetration hypervolume of contact problem $[m^{\eta+2}]$
V_{int}	Intersection volume in hypervolume coefficient function $[m^3]$
$V_{int,hcx}$	Hypervolume centroid shift parameter $[m^3]$
$V_{int,plastic}$	Plastic hypervolume shift parameter $[m^3]$
w	Radial wheel deformation $[m]$

z	Soil sinkage $[m]$
z_{max}	Maximum penetration depth of wheel $[m]$
z_{reb}	Soil rebound $[m]$
α	Energy scaling factor $[Nm]$
γ	Dimensionless soil rebound parameter
Γ	Shear velocity of flexible wheel/soil contact $[m/s]$
Δ	Wheel sinkage of flexible wheel $[m]$
$\dot{\Delta}$	Wheel sinkage rate of flexible wheel $[m/s]$
η	Nonlinearity exponent
θ	Wheel contact patch angle $[rad]$
θ_s	Static wheel/soil interaction angle $[rad]$
ρ	Density of wheel $[kg/m^3]$
τ	Shear stress in wheel/soil interface $[MPa]$
τ_{max}	Soil shear strength $[MPa]$
ϕ	Internal friction angle $[rad]$
φ	Normal direction angle $[rad]$
ψ	Wheel domain angle $[rad]$
ω_y	Wheel spin $[rad/s]$
Ω	Cost function

Matrices and Vectors

$\mathbf{a}$	Vector of wheel/soil contact model parameters to be identified
$\mathbf{F}_C$	Forces applied to the wheel center $[N]$
$\mathbf{F}_n$	Contact normal force $[N]$
$\mathbf{F}_P$	Forces acting in the contact patch $[N]$
$\mathbf{I}$	Identity matrix
$\mathbf{M}_C$	Moments applied to the wheel center $[Nm]$
$\mathbf{M}_P$	Moments acting in the contact patch $[Nm]$
$\mathbf{n}$	Vector of contact normal
$\mathbf{p}$	Location vector of Point P $[m]$
$\dot{\mathbf{p}}$	Velocity vector of Point P $[m/s]$
$\mathbf{r}_{hc}$	Vector of the hypervolume centroid position $[m]$
$\mathbf{r}_{P/C}$	Vector between contact patch and wheel center $[m]$
$\mathbf{R}$	Rotation matrix
$\mathbf{S}$	Contact surface domain

Chapter 1

Introduction

Since the 1970s, mobile robotic vehicles have been used in lunar and planetary exploration missions to either assist astronauts or autonomously perform scientific tasks. The early designs of these planetary rovers were inspired by terrestrial automobiles with wheeled or tracked locomotion systems. Over the years, suspension designs specifically developed for space exploration have been proposed involving legged walking robots or hybrid systems. To date, the most successful designs are wheeled systems in combination with independent rocker suspensions and it is expected that further developments in mobility technology will have a major impact on future surface exploration missions. For the development of such planetary rovers, modelling and simulation of these vehicles is required not only to assist engineers in the design process but also for the development of control algorithms or path planing strategies. A crucial factor in these simulations is the contact model that represents the interaction between the rover wheel and the terrain material. The contact model defines the performance of the vehicle and the power required to perform certain manoeuvres. The main objective of this thesis is the development of a terramechanics contact model that is suitable for efficient multibody dynamics simulations of the rover locomotion system.

1.1 Background

Terramechnics is the application of soil mechanics theories to vehicle and terrain interaction problems such as a planetary rover operating on compliant soil. A terramechanics model of interaction between a rover wheel and the soil can be used to accurately simulate the performance of such off-road vehicles. Due to large deformations in the terrain, distributed

forces are required to represent the stresses in the contact patch. Lumped forces provided by a point contact model commonly used in on-road vehicle simulations fail to sufficiently capture the contact dynamics between a wheel and soft soil. Hence, the tire reactions are often calculated by integrating the stress distributions over the contact patch which is a time consuming process with respect to simulations of multibody systems. In this work, a hybrid contact modelling approach based on volumetric properties of the contact geometry is proposed. Assuming that the soil can be represented by a foundation of continuously distributed springs, the integration of the normal stress due to the soil deformation (or spring deflection) leads to an expression of the normal force as a function of the volume of penetration. This volumetric approach results in a single expression for the contact normal force with the information of the distributed force stored in the properties of the penetration volume.

1.2 Motivation

Early terramechnics soil models used to calculate the stress distribution in the contact patch were developed with respect to large off-road vehicles. In fact, the Bekker pressure-sinkage relation is still the most commonly used soil representation in simulations of various types of vehicles operating on soft and rough terrains ranging from small-scale rovers to heavy-duty trucks. However, the assumptions about the contact patch geometry made in Bekker's model are not applicable for light weight vehicles with small diameter wheels. The volumetric properties used in the contact modelling approach proposed in this thesis carry accurate information about the shapes of the contacting bodies which can be used to improve on the classical terramechnics modelling approaches. In addition, the volumetric closed-form expression of the contact forces provides a sufficient representation of the integrated stress distributions which allows for faster simulations. Furthermore, implemented on parallel computing systems to support the calculation of the volumetric properties, this modelling approach can be used to simulate complex wheel designs in contact with rough terrains.

1.3 Challenges

Due to the highly nonlinear terrain material properties, the soil has to be represented by a foundation of hyperelastic springs which can be modelled using an exponential relation between the spring compression and the force. The integration of the nonlinear spring

deflections results in the contact force expression as a function of a volume of fractional dimensions which requires the introduction of the hypervolume of penetration. The solution of these integrals provides a major challenge. In fact, for most nonlinearity exponents, an analytical solution for the hypervolume does not exist. Furthermore, the application of this approach to planetary rover wheels in contact with soft soil requires the consideration of soil plasticity. A common representation of plasticity is the assumption that the soil does not relax after compression. This means that all of the energy that is needed to compact the soil dissipates. Even if most soils show very little relaxation, a small amount of recoil in the hyperelastic foundation springs can affect the forces predicted by the contact model. With the definition of the soil rebound parameters, the compression of the foundation can be calculated which leads to an equivalent hypervolume that is required to determine the contact forces. When modelling flexible wheels, the determination of the deformed state of the planetary rover wheel is necessary. The assumption of quasi-static conditions can be made to simplify the solution of the deformed geometries so that the developed volumetric models can be applied.

Including a curve-fit parameter for the friction like soil traction model, the proposed wheel/soil contact model utilizes the following four parameters to represent the hyperelastic soil foundation and soil plasticity.

1. k_h hyperelastic stiffness
2. η nonlinearity exponent
3. γ soil rebound (plasticity)
4. k soil shear modulus (traction coefficient)

Additionally, the remaining contact model parameters are all dependent on the assumed geometry of the wheel and its inertia properties. While these wheel parameters can be easily measured, the soil parameters of wheel/soil contact models have to be determined through rigorous experiments such as Bekker's compression test with a BeVameter. In this work, a drawbar pull test is used to identify the model parameter values using experimental data from a prototype of the Juno rover of the Canadian Space Agency (CSA). Moreover, to validate the implementation of the volumetric approach in a rover simulation on 3-dimensional terrain, the simulation results are compared against corresponding experiments of the CSA Juno rover on the same irregular terrain.

1.4 Applications

One of the major advantages of the proposed hypervolumetric contact model is the reduced computational effort required to calculate the forces and moments generated in the wheel/soil interface. This allows for simulations with near real-time performance which makes this approach applicable to online path planing or soil parameter identification problems. Online simulations of planetary rovers are required when the complete information of environmental factors influencing the performance of the rover are not provided a priori. Path planing in planetary rover missions is used to find the most efficient path as power is a critical asset. Although these simulations are not required to run in real-time, improved efficiency is desired since path planning algorithms perform multiple iterations of rover simulations.

Another application of the proposed contact model is for the development of control algorithms for which hardware-in-the loop (HIL) simulations are commonly used. It should be mentioned, that these simulations require real-time performance. Finally, additional potential applications include design optimization, general parameter identification, and sensitivity studies which also require a large number of evaluation iterations.

1.5 Thesis Structure

A brief description of the contents of this thesis is provided here. In Chapter 2, a review of previous contributions to the literature is provided, where the main topics that are significant to the work are surveyed: multibody dynamics and contact mechanics with respect to linear graph theory, terramechnics in wheel/soil interaction modelling, and planetary rovers. In Chapter 3, a novel contact modelling approach based on hypervolumes is proposed and compared with classical terramechnics wheel/soil interaction models. The three subsequent chapters show the application of the proposed approach to planetary rover modelling. Chapter 4 provides a formulation of the volumetric approach in rigid planetary rover wheels and compares single wheel simulation results with experimental data. In Chapter 5, a distributed parameter modelling approach based on continuous beam theory is proposed for the application of the volumetric contact model to flexible rover wheels. These models are implemented into a full vehicle model of the Juno rover using the simulation toolbox MapleSim. In Chapter 6, the simulation results are discussed and compared against experimental results obtained from a Juno rover prototype. The significant contributions of this work are highlighted in Chapter 7, where recommendations for future research are also provided.

Chapter 2

Literature Review

The goal of this project is to develop wheel and terrain interaction models that can be used in multibody dynamics simulations of planetary rovers. For the derivation of the vehicle dynamics equations, a symbolic modelling method based on graph theory is used. The forces between the wheel and the soft soil are calculated by applying terramechanics theories to a volumetric contact modelling approach. The following sections provide a thorough survey of past contributions to the literature of the topics related to this project.

2.1 Analytical Multibody Systems Modelling

The first textbook on mechanical multibody dynamics was written by Wittenburg (1977) starting with the kinematics and dynamics of rigid bodies. A textbook published by Schiehlen (1986) presents multibody systems, finite element systems and continuous systems as equivalent models for mechanical systems. The computer-aided analysis of multibody systems was considered in 1988 by Nikravesh (1988) for the first time. Basic methods of computer aided kinematics and dynamics of mechanical systems are shown by Haug (1989) for planar and spatial systems. In his first textbook, Shabana (1989) deals in particular with flexible multibody systems, whereas he concentrates on computational dynamics of rigid multibody systems in his second book (Shabana 1994). Kecskeméthy and Hiller (1994) introduced an object-oriented formulation to model the dynamics of multibody systems. Contact problems in multibody dynamics were highlighted by Pfeiffer and Glocker (1996). The symbolic modelling approach of multibody systems was described in the book of Samin and Fisette (2003), while the application of multibody formulations to vehicle dynamics was discussed in the textbook by Blundell and Harty (2004).

As the demand for multi-disciplinary modelling and simulation tools increases, especially in the area of automotive engineering, the development of formulations that automatically generate the governing equations of such systems has become a research field of growing importance. Such formulations create models of the overall system given the constitutive models of system components, or even entire subsystems, and a representation of the system topology (Samin and Fisette 2003). In this project, linear graph theory is used to represent the system topology and symbolic computing is exploited to generate the system equations of the full planetary rover model.

2.1.1 Graph-Theoretic Modelling

Linear graphs directly reflect the system topology and, due to their domain independency, the graphs can be easily applied to hybrid systems consisting of components from multiple domains, e.g. mechanical, electric, hydraulic (Sass et al. 2004; McPhee et al. 2004), and even flexible mechanical systems with rigid and compliant contacts (Sandhu, Millard, McPhee and Brekke 2010; Sandhu and McPhee 2010). The unique topology representation with linear graphs allows one to conveniently model 3D mechanical system (McPhee et al. 2004), which can be a tedious process using other graph-based modelling approaches (Samin et al. 2007). Also, the linear graph representation of the system allows for easy generalized coordinate selection as shown in the work of McPhee and Redmond (2006); McPhee (1997).

Linear graph theory provides the theoretical foundation to this project as it has a long history in the modelling and simulation of engineering systems (Chandrashekar, Roe and Savage 1992). Leonhard Euler is widely regarded as the originator of graph theory (Hopkins and Wilson 1997), as his article about a particular bridge connectivity problem in Königsberg from 1736 is of considerable importance to the development of graph theory (Biggs et al. 1998). Since then, linear graph theory has gone through enormous development driven by a wide variety of applications. Developed for engineering applications to model electrical systems (Seshu and Reed 1961), linear graph theory was first applied to a general group of lumped-parameter models in electrical and mechanical domains by Koenig and Blackwell (1960), which is based on the work of Trent (1955).

Andrews and Kesavan (1973b) introduced a "vector-network model", which was used by Baciu and Kesavan (1995) to model the interaction between multiple rigid bodies in 3D space. McPhee generalized this work to model planar (McPhee 1998) and three-dimensional multibody systems using absolute and joint coordinates (McPhee 1996), which was extended for the use of indirect coordinates by McPhee and Redmond (2006). Savage (1997) has shown the advantage of subsystem models when modelling large systems using linear

graph theory. Furthermore, Shi, McPhee and Heppler (2001) have shown that the concept of virtual work can also be included in graph-theoretic formulations that also allow the user to choose a desired set of coordinates.

The development in these modelling methods for either electrical or mechanical systems consequently lead to the combination of the two domains, and Muegge (1996) was the one to first model planar electromechanical systems using linear graph theory. This research was further developed and generalized for 3D systems by Scherrer and McPhee (2003). Examples for modelling multi-physical systems are shown in the work of Sass et al. (2004) and Samin et al. (2007). In these approaches, different formulations were used to model 3D mechanical systems and 1D electrical lumped-parameter systems. The method suggested by Schmitke and McPhee (2005) allowed one to model complex multibody multi-domain systems using a single unified formulation based on linear graph theory and the principle of orthogonality.

The simulation of many tasks in multibody dynamics require the modelling of contacts, which has been done in a number of projects within the Motion Research Group at UW using linear graph theory. Hirschkorn et al. (2006) have modelled a piano hammer mechanism in which the contact was treated as coupled applied forces. Another example of contact modelling using linear graph theory is given in the work of Millard, McPhee and Kubica (2008) in which a volumetric contact model was chosen to represent the soft-hard contact between the foot tissue and the hard floor. Finally, the ability of graph theory to be used in modelling the interaction between a tire and the road can be reviewed in Schmitke et al. (2008).

2.1.2 Volumetric Contact Modelling

As Gilardi and Sharf mentioned in their literature survey on contact dynamics modelling, two different approaches can be chosen to model the contact between two objects. One approach is based on discrete or impulse-momentum methods, whereas the other approach is referred to as the continuous or force-based method. Since the former is generally used to model impact in which the contact time is very brief and rapid energy dissipation due to high accelerations and decelerations occur, continuous methods are normally used to model the contact between tires and roads or even soft soils. These continuous methods, also referred to as regularized or compliant contact models, include the models of Hertz, Hunt-Crossley and simple linear spring-dashpots (Gilardi and Sharf 2002); however, a contact detection algorithm has to be implemented for the application in tire modelling.

Unlike the previously stated compliant contact models, which calculate the normal

contact force based on the penetration depth, the tire model proposed in this project determines contact forces based on volumetric properties of the contact problem. This contact model has been recently developed by Gonthier et al. (2005) and has proven to be valid for various examples of modelling contacts between two hard objects (Gonthier 2007). Furthermore, this contact modelling approach has been experimentally validated for normal force (Boos and McPhee 2011, 2013) and frictional force calculations (Boos and McPhee 2012) in hard-hard contacts. The required volumetric properties of the interpenetration volume of the given contact problem are shown in Figure 2.1.

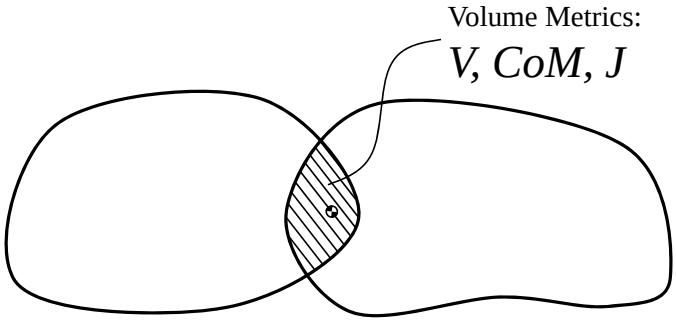

- penetration volume V,
- center of mass CoM,
- interia tensor $\mathbf{J}$.

Figure 2.1: Penetration Volume of Contact

The volume metrics are obtained either analytically or numerically depending on the geometries of the object that are in contact (Gonthier et al. 2008a). The volumetric contact model is based on a Winkler foundation model as proposed by Johnson (1985), and one of the big advantages of this approach is that it can handle multiple contacts and contacts with sharp edges Gonthier (2007). Furthermore, it automatically leads to the consistent selection of the point of action and the calculation of the rolling resistance moment (Gonthier et al. 2008b).

There already exists a precedent for a volumetric based tire contact model in the modelling of tires on hard 3D roads used by the MSC.Adams software package. In the "3D Equivalent-Volume Road Model", MSC.ADAMS computes an approximate volume of intersection between a tire and a 3D surface represented by triangular patches. However, instead of using the volume metrics directly, the volume is converted into an equivalent depth of penetration using empirical look-up tables. The penetration, which represents the tire deflection, is then used to calculate the normal load by considering a linear spring-damper tire model (MSC.Software Corp. 2005).

2.2 Terramechanics

Terramechanics is the application of soil mechanics theories to model the interaction of vehicle systems with terrain. Most commonly that involves modelling the contact between soft soil and locomotion systems of wheeled or tracked vehicles. For simulation purposes, normal and tangential soil contact models have been developed and applied to these types of vehicles.

2.2.1 Normal Contact Force Models

The interaction of a vehicle with the terrain causes large deformations in the compliant ground. Due to the large deformation in the interface, a point contact model as it is often used in on-road vehicle dynamics is not sufficient to represent the normal pressure distribution in the contact patch of a tire or rigid wheel rolling over soft soil. A distributed force is required and the fundamental soil model applied in terramechincs is the Bernstein-Goriatchkin model, which can be described as a continuum with a hyperelastic pressure-sinkage relation. All of the soil models used in off-road tire and planetary rover wheel modelling are based on the Bernstein-Goriatchkin model for contact pressure p:

$$p = k\, z^n \tag{2.1}$$

where k is the stiffness modulus, z is the sinkage and n the sinkage exponent. This model is a result of the experimentally obtained hyperelastic relationship between the normal contact pressure and the sinkage of a flat plate. The stiffness modulus k and sinkage exponent z can then be used to curve fit this characteristic model to the experimental data. Assuming this model is distributed over a planar area results in a foundation of hyperelastic springs. This leads to the idea of applying a volumetric modelling approach to the contact problem of planetary rover wheels on soft terrain. Hence, the Bernstein-Goriatchkin relation and any of the other normal soil models can be applied to the theory proposed in this thesis.

Since Bekker first applied this nonlinear pressure-sinkage relation to off-road tire modelling in 1956, many soil models have been proposed for use in terramechanics. The research on wheel-soil interaction models was then further motivated by the establishment of the International Society of Terrain-Vehicle Systems (ISTVS) in 1962.

The most commonly used pressure-sinkage relation is Bekker's soil equation (Bekker 1969, 1962, 1960), which is an extension to the Bernstein-Goriatchkin model. Bekker separated the stiffness k and introduced two parameters by distinguishing between a cohesive

k_c and a frictional soil stiffness modulus k_ϕ. This added an extra parameter to the curve-fit model that is based on vertical soil compression experiments:

$$p = \left(\frac{k_c}{b} + k_\phi\right) z^n \tag{2.2}$$

where b is the width of the plate used in the experiments, which should be correlated to the size of the tire contact patch. It should be noted that, for soils in which friction is the main structural mechanism such as dry sand, the cohesive stiffness modulus can often be neglected. Vice versa, for terrain materials such as saturated clay, cohesion is the dominant mechanism defining the contact forces and the friction modulus can be assumed to be negligible. In 1965, Reece proposed an extension to this model by improving upon the relationship of k_c and b. The proposed pressure-sinkage relations becomes:

$$p = \left(ck'_c + \gamma k''_\phi\right) \left(\frac{z}{b}\right)^n \tag{2.3}$$

where c is the soil cohesion and γ is the specific weight of the soil. This adjustment to the equation allows for dimensionless curve-fit parameter k'_c and k''_ϕ. Although this slight alteration to the model only differs from Bekker's equation in the response to the plate width b, Reece's proposed model shows significant improvement.

In 2007, Ishigami et al. proposed an improved version of Reece's model to include the curvature of the wheel by modifying the equation to account for the semi-elliptical stress distribution beneath the wheel circumference.

$$p(\theta) = \left(ck'_c + \gamma k''_\phi\right) \left(\frac{z}{b}\right)^n (\cos\theta - \cos\theta_s) \tag{2.4}$$

where θ_s is the static wheel/soil interaction angle and θ is an arbitrary angle defining the wheel contact patch. This pressure-sinkage model first accounted for the geometry of the object interacting with the terrain by introducing the necessary distinction between the stress distribution beneath a wheel and a flat plate.

Even though Ishigami's model showed significant improvement, just as in Bekker's and Reece's models, the pressure-sinkage model is a curve-fit to data obtain from a flat plate experiment. As a result, these models are sufficiently accurate for large diameter wheels only. For wheels with smaller diameters, the curvature of the wheel circumference becomes more prominent in the contact patch which makes it difficult to relate the contact forces to vertical compression measurements. Therefore, (Meirion-Griffith and Spenko 2011) recently published a pressure-sinkage relation for small diameter wheels that appears to be more suitable for modelling planetary rover wheels. Assuming the most fundamental

soil model, Meirion-Griffith introduced the curvature of the wheel into the Bernstein-Goriatchkin pressure-sinkage relation which then yields:

$$p = kD^m z^n \tag{2.5}$$

where D is the diameter of the wheel and m the diameter exponent. This exponent is an added soil parameter that can be used to add extra fidelity to the curve-fit of the sinkage experiments that now have to be performed on actual cylinders rather than flat plates. Even by assuming the Bernstein-Goriatchkin model, this slight alteration showed significant improvement which allows for the prediction of small diameter wheels as they are often used in planetary rover designs.

To calculate the wheel forces from these soil models, the pressure-sinkage equation is usually numerically integrated over the contact patch and then split into two components according to the ISO wheel frame: the vertical force supporting the weight of the vehicle and the longitudinal force representing the compaction resistance. Bekker proposed an analytical solution in which the compaction resistance leads to the exact solution and the vertical force is approximated by further compromising the fidelity of the model with respect to the wheel curvature.

All of the soil models discussed in this section are based on the assumption of a continuum of hyperelastic springs. As a result of the foundation characteristics, a volumetric approach seems appropriate and it can be shown that the discussed pressure-sinkage equations can all be used in such an approach. However, the theory has to be extended to a hypervolumetric contact model to predict the normal contact force due to the large deformation of nonlinear soil. The result is an explicit wheel-soil interaction model that includes the information of the contact geometry and therefore is able to handle different curvature wheels or complex wheel geometries.

2.2.2 Tangential Contact Force Models

To calculate the tangential forces in the wheel soil interface, a number of friction-like tangential force models have been proposed (Janosi and Hanamoto 1961; Oida 1979; Wong 1993). These models are derived from experimental results in which the shear stress is a function of the shear deformation. All of these models use an upper shear stress limit that is related to the soil shearing capacity. A number of failure criteria of soils or other terrain materials have been proposed. However, the most commonly used is the Mohr-Coulomb failure criterion which is described by the following soil failure condition:

$$\tau_{max} = c + p \tan\phi \tag{2.6}$$

where τ_{max} is the shear strength and ϕ is the angle of internal friction of the soil. Wong mentions that for highly cohesive terrain materials such as clay, internal friction can be neglected, whereas for dry sands the frictional component is dominant and the cohesion can be neglected. Wong further clarifies that most terrestrial soils generally possess both cohesive and frictional properties and their shear bearing strength can be described by Eqn 2.6. However, in planetary rover modelling, the dry lunar or Martian terrains are often simulated by neglecting the impact of cohesion.

To further explain the Mohr-Coulomb failure criterion, the Mohr circles of different stress states in a soil specimen can be plotted as shown in Figure 2.2.

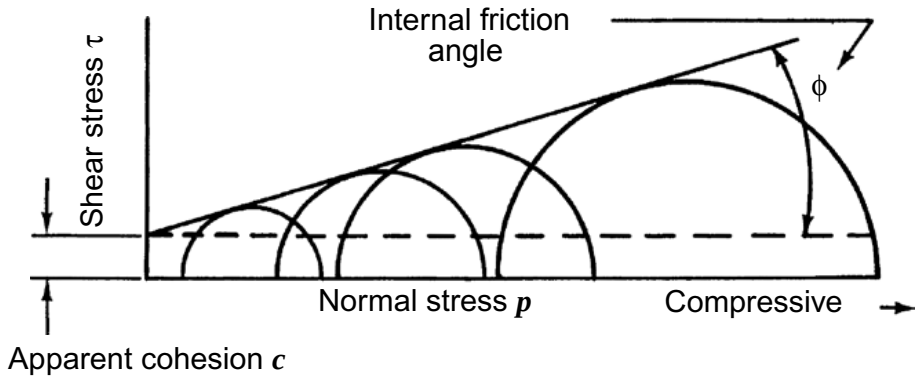

Figure 2.2: Mohr-Coulomb failure criterion (Wong 1993)

Eqn 2.6 then simply defines the linear curve that envelopes the set of Mohr circles for different stress states, where the slope and the intercept with the shear stress axis define the internal friction angle ϕ and cohesion c of the terrain, respectively. Soil failure will occur when the Mohr circle representing a certain stress state exceeds the Mohr-Coulomb envelope. Hence, this failure condition provides the upper bound of the shear stress — the shear strength. However, to represent soil behaviour under shearing, a characteristic model as a function of shear displacement has to be developed. Different shearing behaviour for different soils can be observed from experiments. Most mineral terrain materials can be categorized into two types of shearing response with respect to shear deformation. In the first category, the shear stress asymptotically approaches the shear strength limit, whereas in the second type it initially increases up to a maximum shear stress peak and then drops until it reaches a residual state (see Figure 2.3).

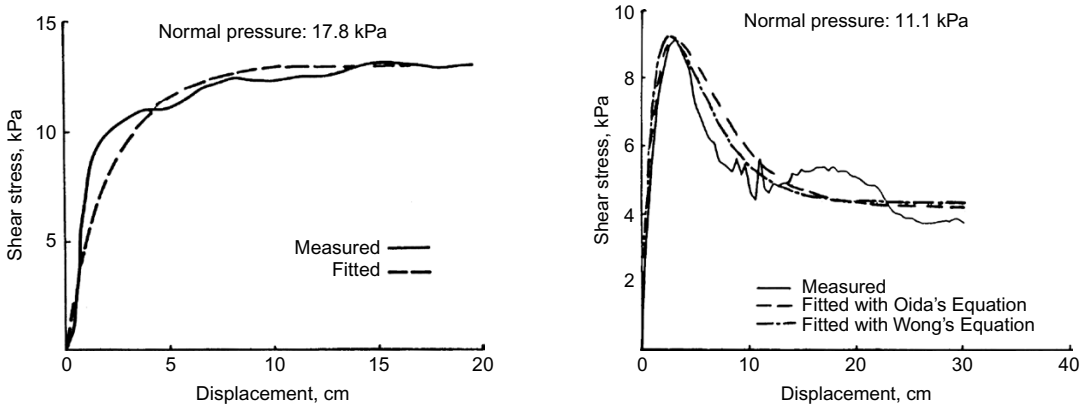

(a) Type 1 (b) Type 2

Figure 2.3: Soil categories with different shearing behaviour (Wong 2010)

Janosi and Hanamoto (1961) first proposed an empirical model from such experiments assuming a soil of the first category. The following exponential model was used to describe the shear stress-strain curve of soil, where τ_{max} is calculated using the Mohr-Coulomb failure criterion.

$$\tau_x \quad (\theta) = \tau_{max} \left(1 - e^{-\frac{j_x(\theta)}{K_x}}\right) \tag{2.7}$$

where j_x is the shear deformation that can be calculated by integrating the shear velocity over the contact patch and K is the shear deformation modulus that is used as the curve-fit parameter is this model. The tangential contact force can be calculated by simply integrating the resulting shear stress distribution over the contact patch between the wheel and the soil. Janosi and Hanamoto proposed an analytical solution for the longitudinal force assuming a uniform normal pressure distribution under a track, which was also applied to deformable wheels with a flat bottom contact patch (Janosi 1961).

For the second type of soil, Oida (1979) and Wong (1993) proposed equations using two parameters to empirically curve-fit the models to the shear experiments.

These models were all developed with respect to heavy duty off-road vehicles, and Senatore and Iagnemma (2011) pointed out that these models are not necessarily suitable for the application of small scale and light weight planetary rovers driving on dry, granular soils. Also, in case of large shear deformations occurring at high contact velocities, the shear stress approaches a constant distribution over the contact patch. Hence, for these types of vehicles, appropriate experiments on single wheels or a full rover have to be performed to which traction force models can be fitted.

2.2.3 Application to Tire Modelling

Modelling methods for tires can be numerical, empirical or purely symbolical. Numerical models such as finite element tire models are of very high fidelity (as in the work of Fervers (2004)) but are often computationally too expensive for multibody vehicle simulations. Empirical models can be of symbolic nature; these models require experimental data, which is used to curve-fit functions for tire parameters as in the case of the tire model by Pacejka (2006). The data collection can be tedious and often requires expensive equipment such as tire test benches. Therefore, a purely symbolic model with fewer parameters such as the Fiala tire model (also used in the work of Morency (2007)) is often the best choice for vehicle dynamics simulations. However, when it comes to uneven and soft terrain, the tire model needs to be extended to include the dynamics of the compliant ground. Moreover, the transverse tire dynamics change depending on the compound of the soil. A review of such tire models including the interaction with soft soil in given in Wong (1991).

For tires on hard surfaces, Sayers and Han (1996) listed a number of tasks that need to be completed to properly calculate the tire forces and moments that can be applied to the multibody system model of the vehicle:

1. Define acting location of tire force
2. Determine vertical force
3. Define local tire coordinates
4. Determine tire kinematics

Following these tasks, the tire forces can be calculated with the tire model. Using the following equations (Schmitke et al. 2008), those calculated tire forces and moments can then be applied to the desired frame (usually at the wheel center) on the multibody system:

$$\mathbf{F}_C = \mathbf{F}_P \tag{2.8}$$

$$\mathbf{M}_C = \mathbf{M}_P + \mathbf{r}_{P/C} \times \mathbf{F}_P \tag{2.9}$$

where $\mathbf{F}_C$ and $\mathbf{M}_C$ are the forces and moments applied to the wheel center, respectively, $\mathbf{F}_P$ and $\mathbf{M}_P$ are the forces and moments acting in the contact patch, respectively, and $\mathbf{r}_{P/C}$ is the vector from the wheel center to the contact patch. Schmitke, Morency and McPhee (2008) have implemented these tasks into a symbolic environment, DynaFlexPro, which has since become the multibody engine for the simulation toolbox MapleSim. To extend

the implementation of tire models for planetary rover application capabilities, a model for the soft soil has to be considered before proceeding with the tasks listed above.

Most soil models discussed in the following were developed with respect to heavy duty off-road vehicles as that defined the main application in the early years of research in terramechanics. Similarly to the tire models, these soil models inherit different levels of fidelity depending on the approach. These approaches include finite element methods (FEM), granular models using distinct element methods (DEM), and various continuous models with hyperelastic and hyper-viscoelastic properties. Yong and Fattah (1967) first used finite elements to determine the soil deformation under a rigid wheel. This model was further developed by Boosinsuk and Yong (1984), and the most recent finite element models of soil/tire interaction include a deformable tire and inflation pressure distribution as in the work by Fervers (2004). A similar approach to FE models is the distinct element method. In the DEM approach, the compliant ground is modelled with small granular soil elements, each of which interacts with its adjacent elements. Most recent work has been published by Khot et al. (2007) and by Nakashima and Oida (2004), who combined a FE model of the soil with a top layer of distinct elements that directly interact with the tire.

For multibody systems, the most commonly used model to represent the soil in a tire/soil interaction model is based on the pressure distribution by Bekker (1962) as presented in section 2.2.1. Bekker's model is a continuous model with hyperelastic properties for the vertical compaction of the soil (Bekker 1960). This soil model includes three Bekker parameters (k_c, k_ϕ and n) that can be obtained from experiments with a BeVameter or a simple cone penetrometer (Bekker 1969). The Bekker model has been improved and extended by contributions of many researchers such as Reece (1964) who suggested a similar model with slightly different parameters. Later, Wong (1993) introduced different models for different sections over the tire in which the load on the soil can be different. Further developments were made by others to include the effects of viscoelasticity (Grahn 1992) or soil deposition (Krenn and Hirzinger 2008b, a; Schäfer et al. 2010).

Considering the previously listed task suggested by Sayers and Han (1996), the Bekker model is used to calculate the normal force which is then applied to the tire model to calculate the tire forces and moments. In many applications of off-road vehicles, the tire is significantly stiffer than the soil. Therefore, the tire is often assumed to be rigid which simplifies the tire/soil interaction model to be only dependent on the soil dynamics and the tire geometry. Thus, the contact behaves like a hyperelastic spring, where the spring stiffness and the exponent representing the hyperelasticity are defined by Bekker's soil parameters. Early contributions to rigid tire models were made by Bekker himself and Janosi (1961). By improving the expressions of the tire kinematics used in the model, Onafeko and Reece (1967) extended the previous work of Janosi and Hanamoto. That

the assumption of a rigid tire is sufficient enough in many cases is also shown by Wong (1993) who distinguished between towed (Wong and Reece 1967a) and driven wheels (Wong 1991). In fact, prototypes of planetary rovers are often designed to run on aluminum or even titanium tires for which this assumption of rigid tire properties has been proven to be valid by Bauer et al. (2005a). This is also shown in their extended work (Bauer et al. 2005b).

Early work on contact models including deformable tires and Bekker soil has also been done by Janosi and Hanamoto (1961). A summary of 10 years of research on vehicle and terrain interaction is given by Schmid (1995), including several analytical soil contact models. For the normal force calculation in these models, the interpenetration area of a thin disc in contact with the deformed soil profile is determined by using different approaches (Schimd and Ludewig 1991). In those models the penetration area is converted into a representative tire deflection so that a conventional spring tire model can be used to calculate the normal force. Harnisch et al. (2005) used one of Schmid's approaches to develop the commercially available tire model ©AS2TM for implementation in ORSIS (Harnisch and Lach 2002), a simulation platform for heavy military trucks (Harnisch et al. 2003). Finally, Abd El-Gawwad et al. (1999d) implemented the previously discussed continuous soil models into a multi-spoke tire to calculate the normal force.

Whereas the FE models calculate the total force vector directly, the tangential forces in the symbolic modelling approach have to be calculated separately from the normal force (Sayers and Han 1996). In that case, the longitudinal force, which defines the traction on the tire, and the lateral force that defines the transverse dynamics of the vehicle are often calculated using a similar approach based on the horizontal soil strength. Therefore, Janosi and Hanamoto curve-fitted the shear tension-displacement relations that were obtained experimentally. They used exponential functions that start from zero, increase rapidly and approach a maximum shear stress value. The maximum stress can be mathematically described using the Mohr-Coulomb shear failure criterion (Janosi and Hanamoto 1961). This approach has been investigated and especially improved for lateral forces by Schwanghart (1968).

The Janosi and Hanamoto approach works fine on most sands, saturated clay and fresh snow. An alternative description of the relation between deformation and shear stress was published by Wong (1993). This approach was developed to include "Type 2" soils in which the stress-displacement curve reaches a maximum shear stress and decreases again after the "shear-off" of the surface mat is initiated (Wong 1993). By relating the shear displacement of the soil in the tire contact patch to the tire kinematics, i.e. longitudinal slip and slip angle, one can calculate the longitudinal and the lateral force respectively. Grecenko (1967) suggested an alternative kinematic relation that can be used for such calculations.

Recent developments in predicting the traction force of a heavy off-road vehicle have been performed by Li and Sandu (2007). In addition, Schreiber and Kutzbach (2007) have investigated zero-slip effects of an off-road tire and proposed methods to incorporate these into traction force models. Due to the sinkage of the wheel into the ground and the resultant enlarged contact patch, there is still slipping between the wheel and the soil when the zero slip state used in conventional on-road tire models is reached (Schreiber and Kutzbach 2007). Since the same soil stress relation is used to model the lateral and longitudinal tire forces, Crolla and El-Razaz (1987) have suggested a method to combine the calculation of these forces and Li and Sandu (2008) further developed this idea.

In their series on tire/soil interaction modelling, Abd El-Gawwad, Crolla, A. and El-Sayed (1999a) discuss modelling methods and the effect of straight (Abd El-Gawwad et al. 1999a) as well as angled lugs (Abd El-Gawwad et al. 1999c). Additionally, Abd El-Gawwad et al. (1999b) investigate the effect of camber on the tire performance.

A common shortcoming of analytical off-road tire models is that they can not handle multiple contacts. Also, they lack an accurate prediction of the tire forces when they are in contact with sharp edges (Harnisch 2005). However, these are both likely scenarios for a planetary rover considering the surface of the Moon or Mars. The volumetric contact model, which will be used for the normal contact force calculation of the off-road tire model proposed in this project, has been proven valid for these type of contacts.

2.3 Planetary Rovers

Planetary rovers have been an essential element of space exploration to perform scientific tasks on distant lunar and planetary surfaces. The Lunar Roving Vehicle (LRV) was developed for NASA's Apollo program in the 1970s and was one of the first mobile rovers designed to assist astronauts on space exploration missions. Since then, 13 surface missions have been reported using rovers, most of which are wheeled designs (Seeni et al. 2010). The most prominent projects include the Mars exploration missions (MER) of Spirit and Opportunity in 2003 and the most recent mission with Curiosity, which landed on the Martian surface in 2012.

For a majority of planetary rover projects in the past, rigid wheels were implemented for reasons of robustness and reliability. For example, all three of NASA's MER rover wheels are rigid wheel designs that resemble a nearly cylindrical shape. However, due to the tractive advantage over rigid tires, various types of flexible tires have been engineered and tested on recent exploration vehicles. An example is the Goodyear woven wire spring

tire which is based on the original LRV wheel design. Also among the more popular designs are the Michelin Tweel, which consists of a composite material, and the flexible metal wheel used for the ExoMars rover as presented in Barnes et al. (2006) and Patel et al. (2010). A picture of the rigid MER wheels and the flexible ExoMars rover wheel design is shown in Figure 2.4.

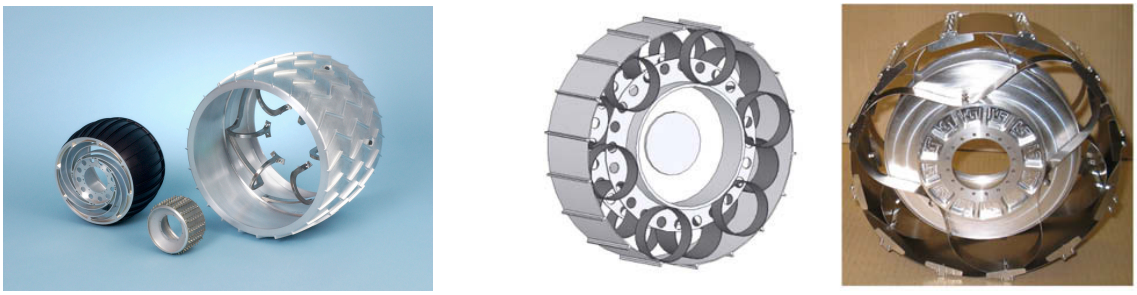

(a) MER wheels

(b) ExoMars wheels

Figure 2.4: Rigid and flexible rover wheel designs (Favaedi et al. 2011)

For the design of all of these rovers, vehicle mobility simulations were performed for which models representing the rigid and flexible wheels were required.

2.3.1 Rigid Planetary Rover Wheel Models

The foundation for the work of rigid planetary rover wheels was done in the early years of terramechanics when the theories were initially developed for large scale off-raod vehicles. Wong (1967) further studied the soil behaviour under a rigid tire and Onafeko and Reece (1967) determined the soil stresses based on the soil deformation caused by the undeformable geometry of a wheel. From a tire dynamics point of view, the rigid tire/soil interaction was studied in the segmented work by Wong and Reece in which the performance of the driven wheel was compared against the performance of a towed wheel (Wong and Reece 1967a, b). Within this work, the authors also discussed slip lines and the point of maximum radial pressure in the contact patch. The movement of soil particles under the impact of a driven wheel was also studied by Yong and Fattah (1975). Due to the plastic deformation in the soil caused by the wheel rolling over soft soil, Wong (1993) proposed to separate the contact patch into sections depending on whether the soil is in compression or relaxation. With a focus on planetary exploration rover projects, the rigid tire models regained popularity. A summary of these methods can be found in Wong's

textbooks (Wong 1993, 2010) in which he applied terramechanics theories to engineering problems in off-road vehicle designs. Also, Iagnemma and Dubowsky (2004a) summarized and discussed a number of methods directly applied to planetary exploration rovers. Shibly et al. (2005) proposed a wheel model based on these theories that the authors later used for traction control and for on-line parameter identification (Iagnemma and Dubowsky 2004b; Iagnemma et al. 2004). Azimi et al. (2011b) proposed a rigid rover wheel model from a continuum mechanics point of view which is based on infinitesimal plasticity theory. When no analytical approach is used to determine the contact forces, the soil in the contact region is often discretized. As in the work of Krenn and Hirzinger (2008b) in which a grid of point contacts based on Bekker's theory was introduced. The resulting normal force was calculated by summing up the point contact models over the contact patch.

For all of these models, experimental results are required to determine parameters and/or to validate these models. Often a single wheel test bed is utilized for this purpose as shown by Bauer et al. (2005b) as well as Scharringhausen et al. (2009a) who used the experiments to validate their proposed models.

2.3.2 Flexible Planetary Rover Wheel Models

Besides the work on analytical rigid tire models, a number of deformable tire theories have been proposed. Again, fundamentals of the developed theories are based on the application of the models to heavy duty vehicles. For the calculation of the forces generated by a flexible tire in contact with soft soil, the deformed contact geometries have to be determined by solving the force equilibrium with respect to the distributed contact forces. Harnisch et al. (2005) developed a flexible semi-empirical tire model that was implemented in a simulation tool for heavy duty vehicles for military solutions. Chan and Sandu (2007) improved upon the semi-empirical approaches for their off-road tire model, whereas Pinto (2012) proposed a lumped parameter model to represent the tire deformation.

For the application to a relatively slow moving robotics vehicle, a quasi-static approach is commonly implemented as the transient response of the soil can often be neglected. Based on this principle, the models developed by Scharringhausen et al. (2009b) and Favaedi et al. (2011) were designed for application in planetary rover simulations. These models were both validated through single wheel experiments on the flexible wheels designed for the ExoMars rover mission (Scharringhausen et al. 2009a).

2.4 Planetary Rover Simulation and Experiments

For the design of planetary rovers and development of simulation platforms including sophisticated wheel models, prototypes and test vehicles have been designed and built. Ishigami et al. (2007) presented the "Dune" rover that was simulated and used to experimentally validate the proposed rover wheel models. Another rover designed for testing purposes is NASA's "Rocky 7" that has been used since its initial design to test control algorithms of various robotic tasks (Volpe, Balaram, Ohm and Ivlev 1996). Finally, the Juno rover from the Canadian Space Agency (CSA) was designed and built in a joint effort by Neptec Design Group Ltd., Ontario Drive and Gear Ltd. (ODG) and the CSA to test possible planetary locomotion designs and also to develop and validate new wheel soil contact models. These three rover prototypes were simulated and compared with respect to their tractive efficiency in a study by Azimi et al. (2011a). Finally, Krenn and Hirzinger (2008b) have used full vehicle simulation and experiments of the ExoMars rover to develop new high-fidelity contact models for the application to terramechanics problems.

Chapter 3

Nonlinear Volumetric Contact Model

For the development of a novel rover wheel/soil interaction model that provides a closed-form solution for the contact forces, the normal stress distribution is assumed to be a nonlinear function of the soil compression. The soil foundation with which the wheels of a robotic vehicle may interfere is represented by a continuum of hyperelastic springs. A linear version of this representation of the contact interface as a mattress of springs has been used and validated for the simulation of the interaction between two incompliant objects (Boos and McPhee 2013). However, for contacts involving large deformations, the nonlinear material properties have to be considered. In this chapter, a brief summary of the elastic foundation model is given and the extension of the model to a hyperelastic foundation is provided so that it can be used for the intended purpose of modelling rover wheels in contact with soft terrain. A solution for the integral of the normal stress distribution of the rover wheels is proposed and verified in a number of numerical experiments. A comparison against other analytical solutions is also made.

3.1 Elastic Foundation Model

When a nearly rigid object interferes with a compliant medium, it is assumed that deformation only occurs in the flexible contact partner. Moreover, the normal stress distribution can then be directly related to this deformation. Assuming that the compliance is represented by a foundation of linear springs, it has been shown that the resultant contact normal force is proportional to the volume of penetration (Gonthier et al. 2005).

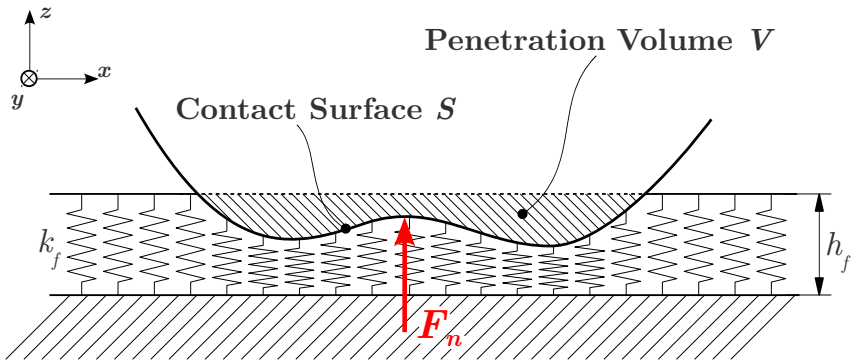

Figure 3.1: Schematic of Winkler foundation model

The proposed model is an extension of the theory of the Winkler foundation (Johnson 1985). This linear elastic foundation can be imagined as a mattress of linear elastic springs. When a body comes in contact with this foundation, the contact pressure is assumed to be proportional to the depth of deformation of the surface of the body, see Figure 3.1, where k_f is the elastic modulus of the foundation and h_f is the arbitrarily chosen depth of the foundation mattress (Johnson 1985).

By integrating the normal stress distribution of the elastic foundation over the contact surface, a general form of the normal force $\mathbf{F}_n$ may be described as a function of the penetration volume V (Gonthier 2007; Gonthier et al. 2008b).

$$\mathbf{F}_n = k_V V \, \mathbf{n} \quad \text{with } k_V = \frac{k_f}{h_f} \tag{3.1}$$

$$V = \iint_S f_S(\mathbf{S}) \, dS \tag{3.2}$$

where $\mathbf{S}$ describes the contact surface, f_S is the depth of deformation at a point on the contact surface $\mathbf{S}$, k_V is the volumetric stiffness and $\mathbf{n}$ is the vector defining the contact normal. Knowing the deformed geometries of the colliding bodies, closed-form solutions for the penetration volume V can be found. Hence, the computationally time-consuming integration of the contact volume can be replaced by a volume expression which only has to be evaluated once every time step.

When calculating the contact forces between a planetary rover wheel and a soft terrain, the linear elastic foundation has to be updated by hyperelastic springs and the stress distribution of Eqn 3.2 becomes nonlinear. The following section discusses the extension

of the foundation model that is necessary to represent the contact between a planetary rover wheel and soft terrain. In addition, a closed-form solution for the contact forces for a nonlinear foundation is also presented.

3.2 Hyperelastic Foundation Model

Due to the highly nonlinear material of soft soils, the linear elastic foundation has to be replaced by a bed of hyperelastic springs. This is equivalent to representing the pressure distribution in the foundation interface with the pressure-sinkage relations of one of the terramechincs soil models discussed in section 2.2.1. The integration of the updated hyperelastic stress distribution over the contact surface results in Eqn 3.3 for the normal force $\mathbf{F}_n$:

$$\mathbf{F}_n \;=\; k_h \iint_S f_S^{\eta}\left(\mathbf{S}\right) dS \; \mathbf{n} \tag{3.3}$$

where η is the nonlinearity exponent and k_h is the hyperelastic foundation stiffness. By solving the integral of the hyperelastic spring displacements, it can be shown that the normal contact force is now proportional to an $(\eta+2)$-dimensional hypervolume with the hyperelastic foundation stiffness k_h as the proportionality factor. As there is no damping considered in the Bernstein-Goriatchkin model, from which all other pressure-sinkage relations are derived, no velocity component is included in the normal force. Eqn 3.3 can therefore be simplified to Eqn 3.4:

$$\mathbf{F}_n = k_h V_h \; \mathbf{n} \quad \text{with} \quad V_h = \iint_S f_S^{\eta}\left(\mathbf{S}\right) dS \tag{3.4}$$

where V_h is the hypervolume of penetration. Once this hypervolume is determined for a contact problem, the normal force can be calculated using the relation shown in Eqn 3.4. It should be noted that the hypervolume is a function of the contact geometry and the material nonlinearity exponent η. For a general form of this contact model, the interdependence of the geometry and material parameters should be resolved.

3.2.1 General Hypervolume Calculation

By introducing the definition of the hypervolume, the challenge is to solve the integral of Eqn 3.4. In fact, for most nonlinearity exponents η, an analytical solution does not exist

even under the assumption of very basic contact geometries. However, it is necessary to find the solution of the following integral assuming that the contact region S lies in the horizontal x-y-plane:

$$V_h = \iint_S f^{\eta}(x,y)\,dx\,dy$$

To find an approximation for the integral, the hypervolume V_h is assumed to be a function of the penetration volume V. The mean value theorem is used to find a weighted averaging function of the penetration volume that shows an initial relation between the hypervolume and the penetration volume. Inspired by said mean value theorem of a surface integral over a region D:

$$\iint_D h(x,y)\,g(x,y)\,dxdy = c\iint_D g(x,y)\,dxdy$$
$$\text{where} \quad \inf\ h(D) \le c \le \sup\ h(D),$$

where $\inf\ h(D)$ and $\sup\ h(D)$ are the infimum and supremum of the values attained by the function h over the region of D, respectively. The value c then is the average of $h(x,y)$ over the region D weighted by the function of $g(x,y)$. With this definition and by separating the hyperelastic penetration function in the hypervolume integral, the following expression for the hypervolume as a function of the penetration volume can be derived:

$$\begin{aligned} V_h &= \iint_S f^{(\eta-1)}(x,y)\,f(x,y)\,dxdy \\ &= c_v(V)\iint_S f(x,y)\,dxdy \\ &= c_v(V)\,V \qquad (3.5) \\ \text{with} \qquad c_v(V) &= \frac{\iint_S f^{\eta}(x,y)\,dxdy}{\iint_S f(x,y)\,dxdy} \qquad (3.6) \end{aligned}$$

where $c_v(V)$ is the hypervolume coefficient. If evaluated numerically for different nonlinearity exponents η, the defined hypervolume coefficient is only dependent on the contact geometry. To show the relation of the hypervolume coefficient to the penetration volume, the solution of Eqn 3.6 is determined by numerically integrating the illustrated integrals.

The following equations representing a vertical torus penetrating the horizontal x-y plane are considered:

$$\begin{aligned} x(\zeta,\xi) &= (R + r\cos(\zeta))\cos(\xi) \\ y(\zeta,\xi) &= r\sin(\zeta) \\ z(\zeta,\xi) &= (R + r\cos(\zeta))\sin(\xi) + (R + r - z_{max}) \end{aligned}$$

for $\zeta, \xi \in [0, 2\pi)$. The parameters R and r are the major and minor radius of the torus respectively, and z_{max} is the maximum penetration depth measured along the z-axis. The penetration function $f(x, y)$ is defined by comparing the z-component of the parametric torus equations against the plane $z(x, y) = 0$. Assuming the penetration of $z_{max} = [0..r]$, the hypervolume coefficient is calculated and plotted over the penetration volume on a double logarithmic scale (see Figure 3.2). The curves in the plot show the results of seven different nonlinearity exponents η within the interval of $0.25 \leq \eta \leq 1.75$, which is assumed to cover a range of most commonly found soils (Wong 2010).

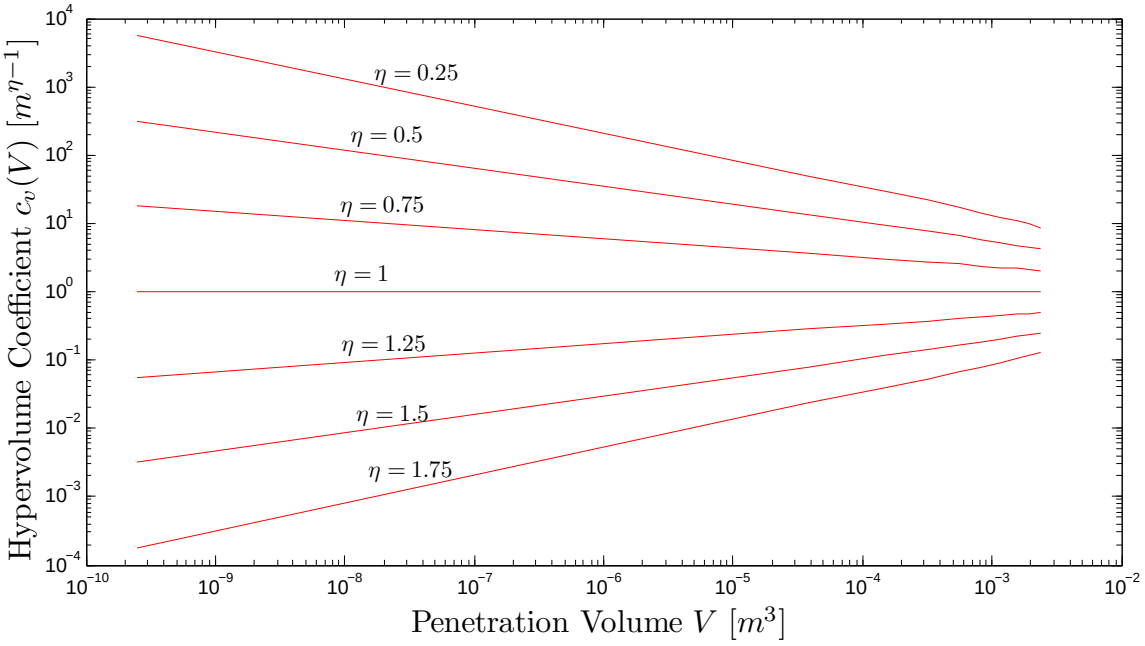

Figure 3.2: Log-log plot of the hypervolume coefficient $c_v(V)$ for a rigid torus on flat ground

The curves in Figure 3.2 show a linear characteristic within the logarithmic scale with an increasing and decreasing trend for $\eta > 1$ and $\eta < 1$, respectively. This is due to the fact

that the numerator of the fractional function in Eqn 3.6 rises faster for $\eta < 1$ and slower for $\eta > 1$ as the function approaches the asymptote where the penetration volume V equals zero. Moreover, the illustrated curves suggest that linear curve fits within the logarithmic scales can be used to approximate the solution for $c_v(V)$ so that the hypervolume can be expressed as a function of the penetration volume:

$$V_h = e^{a_0 + a_1 \ln(V)} V \tag{3.7}$$

where a_0 and a_1 are the linear curve fit parameters and have to be determined for each value of the nonlinearity exponent η. For simplified geometries, a parametric expression for these curve fit parameters can be found which results in a hypervolumetric normal force model with separated geometry and material parameters. The derivation of such a model is shown in the following section for cylindrical wheels of constant width.

3.2.2 Hypervolume for Wheel with Constant Width

Although the presented hypervolume model is generally capable of handling complex geometries, the derivation of such a model is shown below. A wheel profile with constant width is assumed so that the surface integral of Eqn 3.4 can be simplified to:

$$\begin{aligned} V_h &= \iint_S f^{\eta}(\mathbf{S})\, dS \\ &= b \int f^{\eta}(x)\, dx \end{aligned}$$

where b is the wheel width and $f(x)$ is the displacement of the nonlinear foundation. Considering the mean value theorem for a single integral, the following expression for the hypervolume of constant width objects can be derived. It is a function of the penetration volume, similar to the previously shown derivation of the general hypervolume function.

$$\begin{aligned} V_h &= b \int f^{(\eta-1)}(x)\, f(x)\, dx \\ &= c_v(V)\, b \int f(x)\, dx \\ &= c_v(V)\, V \end{aligned} \tag{3.8}$$

$$\text{with} \qquad c_v(V) = \frac{\int f^{\eta}(x)\, dx}{\int f(x)\, dx} \tag{3.9}$$

For the following derivation, a perfect cylinder profile with a constant width b and radius R is considered. The hypervolume coefficients of a cylinder penetrating a flat ground are numerically calculated considering the following equation.

$$V_h = b \int_{-a}^{a} \left(\sqrt{R^2 + x^2} - (R - z_{max}) \right)^{\eta} dx$$
$$\text{with} \quad a = \sqrt{2Rz_{max} - z_{max}^2}$$

where z_{max} is the maximum penetration depth.

Again, the results of seven different nonlinearity exponents η within the interval of $0.25 \leq \eta \leq 1.75$ are calculated and plotted over the penetration volume. Moreover, a linear curve fit for each of the hypervolume coefficient functions is performed and also included in the plot. The comparison is shown in Figure 3.3. The solid lines represent the numerical solution, where linear curve fits that are used for the derivation of the hypervolumetric model are illustrated as dotted lines.

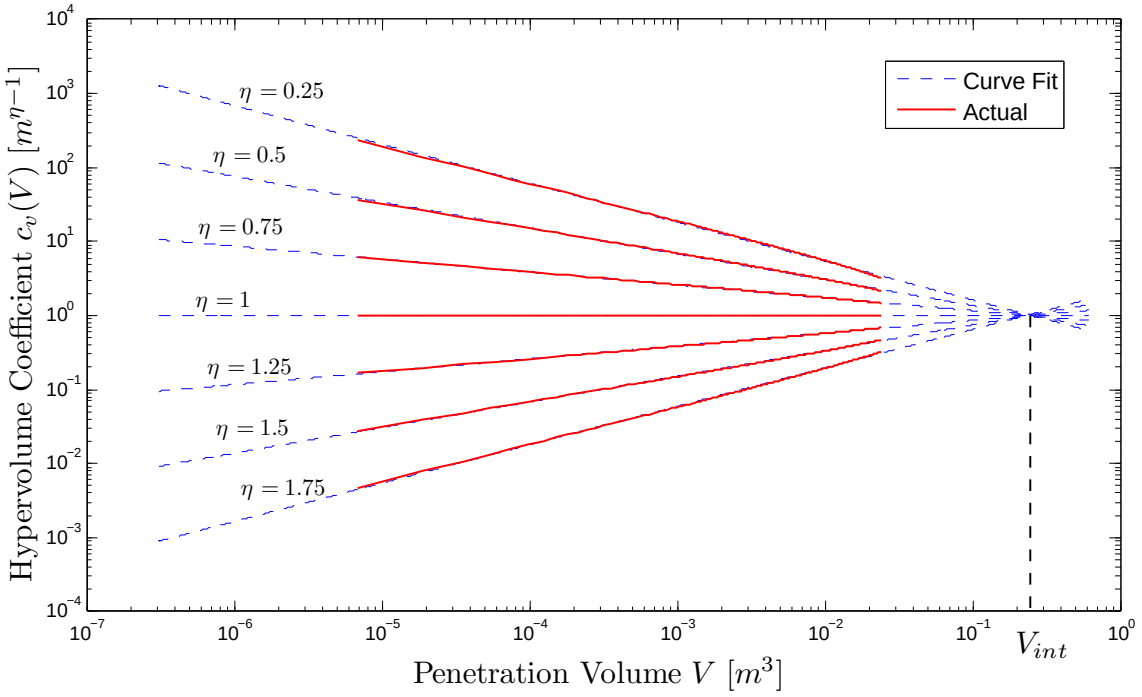

Figure 3.3: Log-log plot of hypervolume coefficient $c_v\,(V)$ for a rigid cylinder on flat ground

The direct comparison against the actual $c_v\,(V)$ function confirms the choice of the linear model with the double logarithmic scale. It can also be noticed that the curves

of the hypervolume coefficient models with the different nonlinearity exponents intersect at one point that represents a certain penetration volume. This intersection volume V_{Int} can be used to further identify the relationship between the hypervolume coefficient and the penetration volume. This crossing point is determined by taking into account the curves of at least two nonlinearity exponents for which the solution of the hypervolume coefficient $c_v(V)$ is known. It should be noted that the intersection volume depends on the size of the penetrating object and the calculation is discussed in detail later in this section. Before defining characteristic parameters such as the intersection volume, the linear interpolation parameters a_0 and a_1 of the exponential hypervolume model have to be investigated. For that purpose, the numerical experiment illustrated in Figure 3.3 is performed for a number of different cylinder sizes by varying both the radius and thickness of the cylinder from $5cm$ to $30cm$. These cylinder sizes taken into consideration for the derivation of this hypervolumetric model are assumed to cover the range of most small-size robotic vehicles up to large-scale planetary rovers (Juno rover wheel radius is $28cm$). For each for the penetration tests, the hypervolume coefficients are determined using the exponential model shown in Eqn 3.7 and the resulting interpolation parameters are plotted over the nonlinearity exponent η. The results can be seen in Figure 3.4.

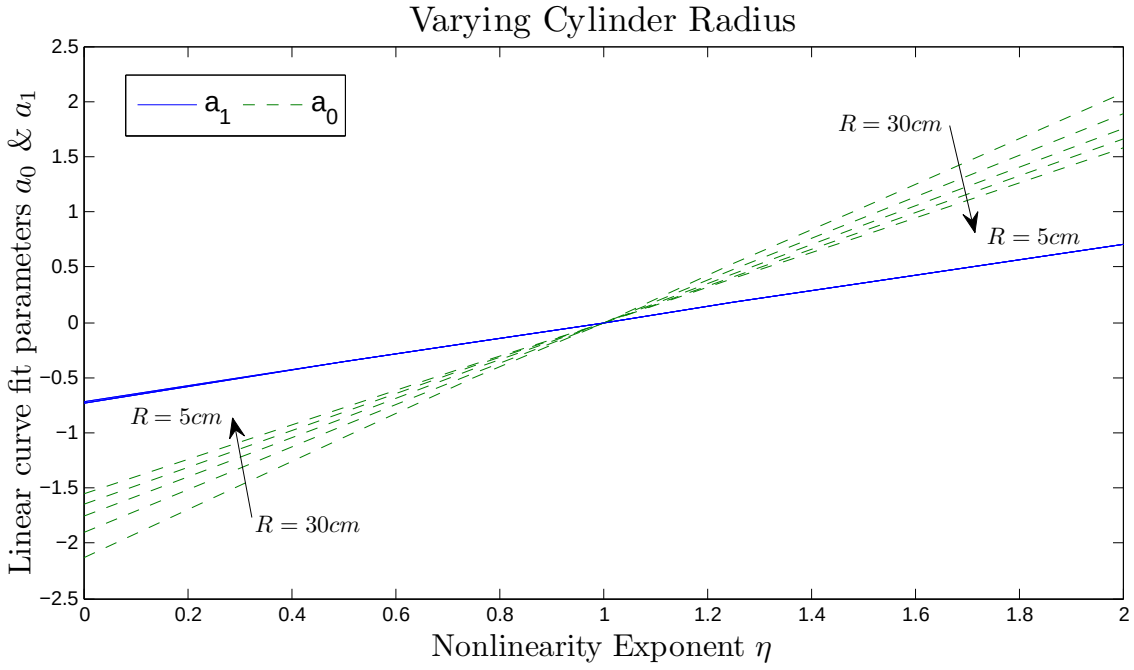

Figure 3.4: Interpolation parameter of exponential hypervolume coefficient model

The dashed curves illustrated in the plot represent the parameter a_0, where the solid curves that all coincide with each other represent the slope parameter of the linear curve fit a_1. It is evident that both parameters change in nearly linear fashion with respect to the nonlinearity exponent. As it is necessary by definition of the problem, the illustrated curves of these interpolation parameters show a root considering a linear elastic foundation with an exponent of $\eta = 1$ for which $V_h \equiv V$. Parameter a_1 remains the same for all different cylinder sizes, whereas parameter a_0 changes with respect to the change in geometry size. Regarding the latter parameter, the quantitative change of the cylinder geometry can be equalized by the use of a scaling factor. This factor is the intersection volume V_{int} discussed previously. It can be shown that by scaling the curves of the parameter a_0 with $\ln V_{Int}$, they can be made to coincide with the curves of the parameter a_1. Defining A_1 as the slope of these linear functions of η, leads to the following simplification of the hypervolume coefficient model.

$$\begin{aligned} c_v(V) &= e^{a_0 + a_1 \ln V} \\ \text{with} \quad & a_1 = A_1(\eta - 1) \\ \text{and} \quad & a_0 = -A_1(\eta - 1)\ln V_{int} \\ c_v(V) &= \left(\frac{V}{V_{int}}\right)^{A_1(\eta-1)} \end{aligned}$$

where the remaining parameters are A_1 and V_{int} which are related to the contacting geometries. The geometry parameter A_1 is constant for each geometric pairing, whereas V_{int} is dependent on the size of the colliding objects.

3.2.3 Geometry Parameter Calculation

The intersection volume V_{int} and the geometry parameter A_1, can be calculated by considering the curves of the hypervolume V_h for at least two nonlinearity exponents for which the solution is known. For that purpose, the solutions of the integral $b \int f(x)^\eta dx$ for $\eta = 1$ as well as the trivial solution for $\eta = 0$ are considered. Taking the geometry of a perfect cylinder into account, the following solutions for two different hypervolumes can be found:

$$\begin{aligned} \text{For } \eta = 1: \quad & b \int_{-a}^{a} f(x)dx = V \quad \text{(Penetration volume)} \\ \text{For } \eta = 0: \quad & b \int_{-a}^{a} f(x)^0 dx = b \int_{-a}^{a} 1dx = 2\,b\,a \\ \text{with} \quad & a = \sqrt{2Rz_{max} - z_{max}^2} \end{aligned} \tag{3.10}$$

Knowing these solutions, the following hypervolume coefficients can be found.

$$C_v(V(\eta = 1)) = 1 \tag{3.11}$$

$$C_v(V(\eta = 0)) = \frac{2\sqrt{2Rz_{max} - z_{max}^2}}{V} \tag{3.12}$$

With these solutions of the coefficient functions, one could theoretically calculate the intersection volume for the hypervolume model as the intersection point of these curves. However, the intersection volume does not actually exist; in the case of the cylinder, the square root of $C_v(V(\eta = 0))$ becomes negative before the two curves intersect. Therefore, the intersection volume has to be determined numerically by finding the linear curve-fit function of C_v on the double logarithmic scale. Due to the linear approximation on the double logarithmic scale, the two resulting lines of $C_v(V(\eta = 1))$ and $C_v(V(\eta = 0))$ have to intersect. For that purpose, a linear regression to find $C_v(V(\eta = 0))$ is performed.

Knowing the solutions of two hypervolume coefficient functions, the intersection volume can be found by curve-fitting the solutions. One can then extrapolate the curve-fitted solutions to find the point of intersection of the two lines. Assuming a linear solution, the hypervolume coefficient function on the double logarithmic scale yields to

$$\ln\left(C_v\left(V\left(\eta = 0\right)\right)\right) = e^{(a_0 + a_1 \ \ln(V))} \tag{3.13}$$

where a_0 and a_1 are the linear curve-fit coefficients. It should be noted that the solution for $C_v(V(\eta = 1))$ is still equal to 1 even on a logarithmic scale. To find the coefficients a_0 and a_1, a linear regression is calculated by evaluating the true solution of $\ln(C_v(V(\eta = 0)))$ at a certain number of evaluation points (the penetration volume) using the following equation.

$$\ln\left(C_v(V(\eta = 0))\right) = \ln\left(\frac{2\sqrt{2Rz_{max} - z_{max}^2}}{V}\right) \tag{3.14}$$

$$= \ln(2\sqrt{2Rz_{max} - z_{max}^2} - \ln(V(z_{max})) \tag{3.15}$$

$$\text{with} \qquad z_{max} = 0..R \tag{3.16}$$

The equation above for $\ln\left(C_v(V(\eta = 0))\right)$ represents the y-values, where $\ln(V(z_{max}))$ represents the x-values for the linear regression procedure. With this definition, the curve-fit

coefficients a_0 and a_1 can be calculated using the following equations:

$$a_0 = \frac{(n\ Sxy - Sx\ Sy)}{(n\ Sxx - Sx^2)} \tag{3.17}$$

$$a_1 = \frac{(Sy\ Sxx - Sx\ Sxy)}{(n\ Sxx - Sx^2)} \tag{3.18}$$

$$\text{with} \quad Sx = \sum_{i=1}^{n} \ln(V)_i$$

$$Sy = \sum_{i=1}^{n} \ln(C_v(V(\eta = 0)))_i$$

$$Sxx = \sum_{i=1}^{n} \ln(V)_i^2$$

$$Syy = \sum_{i=1}^{n} \ln(C_v(V(\eta = 0)))_i^2$$

$$Sxy = \sum_{i=1}^{n} \ln(C_v(V(\eta = 0)))_i\ \ln(V)_i$$

where n is the number of evaluation points over the interval $z_{max} = 0..R$. With these coefficients, the intersection volume can be calculated as the crossing point of the curves $\ln(C_v(V(\eta = 1)) = 1$ and $\ln(C_v(V(\eta = 0))) = \exp(a_0 + a_1\ \ln(V))$ using the following expression:

$$V_{int} = e^{\left(\frac{(\ln(1) - a0)}{a1}\right)} \tag{3.19}$$

It should also be noted that the coefficient A_1 can be directly calculated as a byproduct of the linear regression method. Due to the fact that we calculated the solution for the hypervolume coefficient of $\eta = 0$, the expression of $a_1 = -A_1(\eta - 1)$ becomes $a_1 = A_1$. As a result, the two parameters of the hypervolumetric contact model can both be calculated using this one linear curve-fit of the trivial solution of the hypervolume coefficient function.

Once the hypervolume function $c(V)$ is determined, the normal contact force can be calculated using the following equation.

$$F_n = k_h c_v(V)\, V\mathbf{n} \tag{3.20}$$

This model can now be used for the calculation of the normal forces between the wheel and the soil. Examples and comparison of this model against other normal wheel/soil force models are shown in the following section 3.3.

3.3 Model Comparison

To compare the hypervolumetric contact force model with traditional normal force models for wheel/soil interaction, the methodology proposed by Bekker (1962) is considered for which the geometry in Figure 3.5 is assumed.

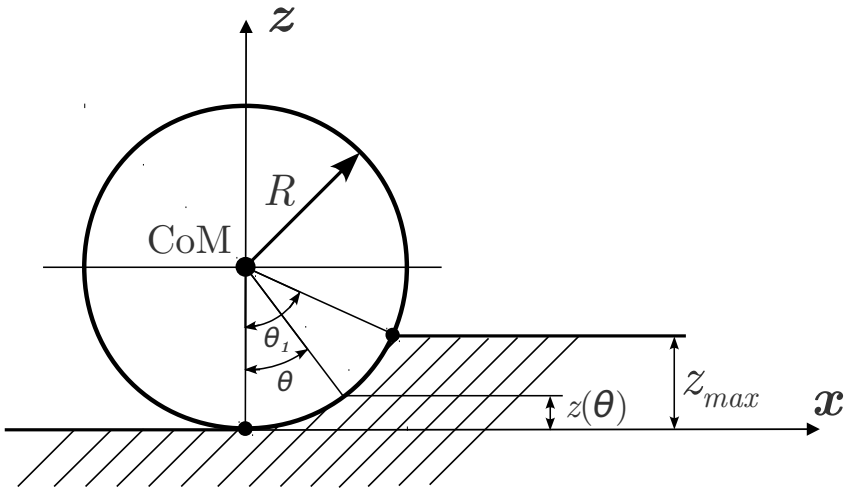

Figure 3.5: Rigid wheel schematic as proposed by Bekker

Under the assumption that there is no soil rebound as it is implied by the illustrated wheel/soil contact schematic, the contribution of the normal force in z-direction that supports the weight of the vehicle can be calculated using Eqn 3.21.

$$F_{z,n} = b \int_0^{\theta_1} \sigma(\theta)\, r \cos\theta d\theta \tag{3.21}$$

where σ is the normal stress distribution over the contact patch and r is the undeformed radius of the wheel. To verify the numerical advantage of the hypervolumetric contact force model, two different pressure-sinkage models are used and the vertical wheel load model as proposed by the corresponding researchers is compared against the volumetric approach and the numerical solution of the integral in Eqn 3.21. First of all, the wheel load is calculated by assuming a traditional Bernstein-Goriatchkin pressure-sinkage model and Bekker analytical approach that is validated for larger diameter wheels. As the curvature of the wheel is not represented in an exact manner, the hypervolumetric model is assumed to perform better in this test. For that reason, a second modified pressure-sinkage relation that takes wheel curvature into account is also utilized for comparison purposes.

3.3.1 Model comparison with traditional pressure-sinkage relation

Assuming the most basic soil model that is based on the Bernstein-Goriatchkin pressure-sinkage relation, the vertical wheel load is calculated by considering Eqn 3.22.

$$\begin{aligned} F_{z,n} &= bk \int_0^{z_{max}} z\,(x)^n\, dx \\ \text{with} \quad & p = kz^n \end{aligned} \tag{3.22}$$

where b is the wheel width, z_{max} is the wheel sinkage, and the material constants k and n are the sinkage modulus and exponent respectively. Assuming Bekker's analytical approach, the solution for the integral in Eqn 3.22 can be approximated using Eqn 3.23.

$$F_{z,n} = \sqrt{2R}\frac{bk}{3} z_{max}^{\left(n+\frac{1}{2}\right)} (3-n) \tag{3.23}$$

Assuming the same pressure-sinkage soil model, the hypervolumetric model is used to calculate the vertical wheel load. By substituting the Bernstein-Goriatchkin into the proposed volumetric model for cylindrical wheels in contact with soft soil, the wheel load yields to Eqn 3.24.

$$\begin{aligned} F_{z,n} &= bkc_v\,(V)\,V \\ &= bk \left(\frac{V}{V_{int}}\right)^{-0.673(n-1)} V \end{aligned} \tag{3.24}$$

where the foundation stiffness is replaced by the sinkage modulus k and the nonlinearity exponent with the sinkage exponent n. As this model is intended to simulate a large diameter wheel, the dimensions shown in Table 3.1 are considered for the following wheel soil compression simulation that is implemented to compare the two different approaches. Moreover, dry sand is considered for this test and the corresponding material parameters can be seen in Table 3.1.

Table 3.1: Foundation and wheel parameters for a large diameter wheel

Sinkage Modulus $k\ [N/m^{2+\eta}]$	Sinkage Exponent n	Wheel Radius $R\ [m]$	Wheel Width $b\ [m]$
$1.783E10^6$	0.75	0.265	0.22

Assuming the listed material and geometrical parameters, the vertical wheel load is calculated for the sinkage interval of $z_{max} = 0..0.1\ m$. The results for Bekker's analytical approach, the hypervolumetric model and the numerical solution of the integral in Eqn 3.22 are shown in the plot of Figure 3.6.

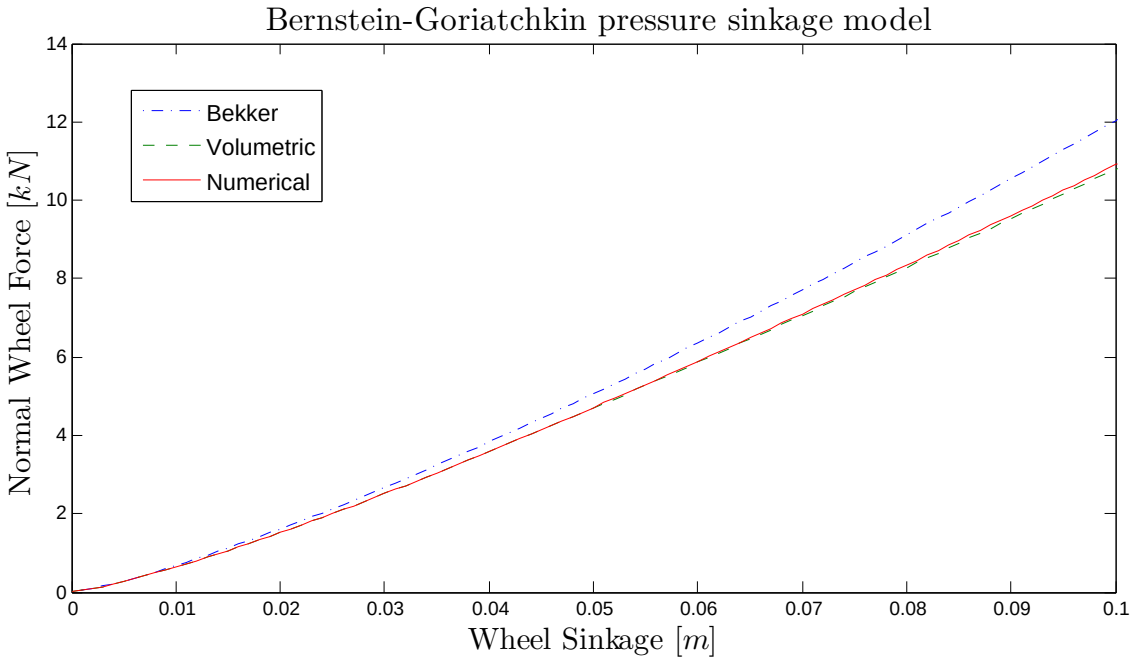

Figure 3.6: Normal force model comparison assuming Bernstein-Goriatchkin pressure-sinkage relation

By comparing the vertical wheel loads shown in the plot, it can be concluded that the volumetric approach is a good approximation for the solution of the integral of the normal pressure distribution. Furthermore, it can be seen that it is closer to said integral solution than the wheel load calculated with Bekker's analytical approach. However, as Bekker's model is developed for the use of large diameter wheels for which the curvature of the wheel is less prominent, it was expected that the Bekker's analytical solution would deviate from the actual solution with increased sinkage. Therefore, a second analytical wheel load model for small diameters is implemented and compared with the volumetric approach.

3.3.2 Model comparison with modified pressure-sinkage relation

To compare the hypervolume model against a normal force model that is developed specifically for use in small-scale robotic vehicle simulations, Eqn 3.25 is used to calculate the vertical wheel load.

$$\begin{aligned} F_{z,n} &= bkD^m \int_0^{z_{max}} z^n dx \\ &\text{with} \quad p = k\,(2R)^m\, z^n \end{aligned} \tag{3.25}$$

where m is the diameter exponent. Taking Bekker's analytical approach into account, Meirion-Griffith and Spenko (2011) proposed Eqn 3.26 for the calculation of the vertical wheel load.

$$F_{z,n} = D^{m+\frac{1}{2}} \frac{bk}{3} z_{max}^{\left(n+\frac{1}{2}\right)} (3-n) \tag{3.26}$$

With the assumption that the foundation is represented by the soil model shown in Eqn 3.25, using the volumetric approach, the vertical wheel force can be calculated with Eqn 3.27.

$$\begin{aligned} F_{z,n} &= D^m bkc_v\,(V)\,V \\ &= D^m bk \left(\frac{V}{V_{int}}\right)^{-0.673(n-1)} V \end{aligned} \tag{3.27}$$

For this sinkage test, a smaller diameter wheel and the same soil as in the previous comparison is used. Due to the use of an additional parameter in the pressure sinkage model, the parameters representing the soil are slightly different from the parameters of the Bernstein-Goriatchkin relation. The geometry parameters of the wheel and material parameters of the soil for this comparison test are listed in Table 3.2.

Table 3.2: Foundation and wheel parameters for a small scale wheel

Sinkage Modulus $k\ [N/m^{2+\eta+m}]$	Sinkage Exponent n	D-Exponent m	Wheel Radius $R\ [m]$	Wheel Width $b\ [m]$
$1.604E10^6$	0.8	0.39	0.085	0.085

Assuming the listed material and geometry parameters, the vertical wheel load is calculated for the sinkage interval of $z_{max} = 0..0.1\ [m]$. The results for the updated analytical approach assuming the modified soil model, the hypervolumetric model and the numerical solution of the integral shown in Eqn 3.25 are shown in the plot of Figure 3.6.

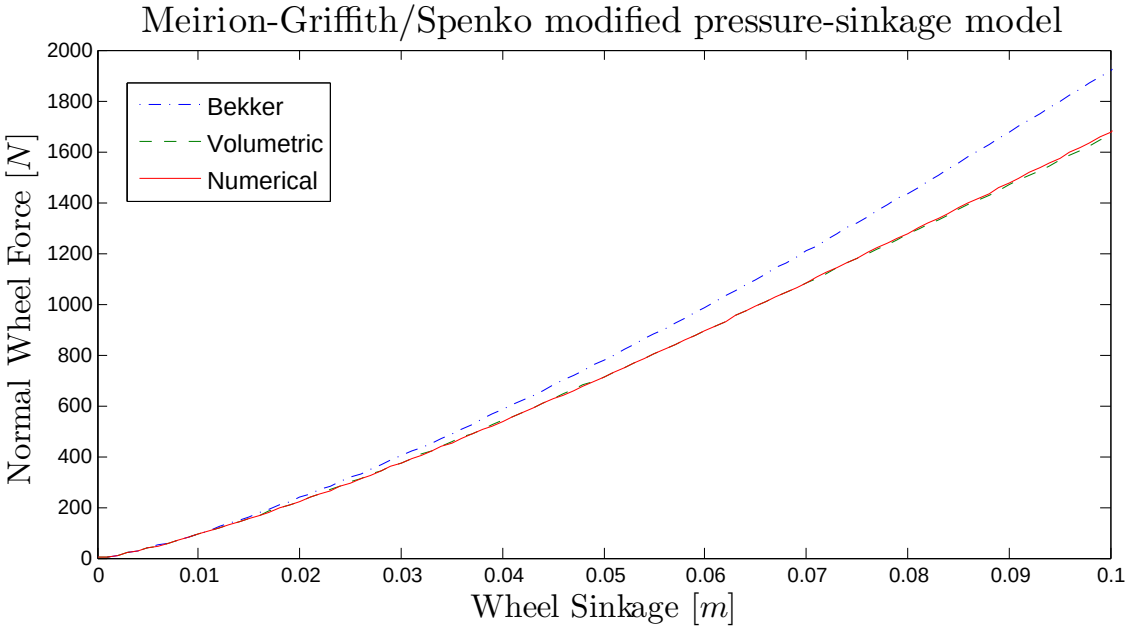

Figure 3.7: Normal force model comparison assuming MeirionGriffith/Spenko pressure-sinkage relation

The direct comparison of the curves illustrated in the plot of the vertical wheel force over the penetration depth show an advantage of the hypervolumetric contact model over the analytical Bekker approach. It can be seen that the analytical approach again deviates more and more with increased wheel sinkage. It shows that the advantage gained from using an extra parameter in the soil model is diminished by using Bekker's analytical approach for the solution of the normal force. To fully use the increased accuracy of the modified pressure-sinkage model, one would have to numerically integrate or use a better model for the contact force such as the hypervolumetric approach.

Chapter 4

Rigid Planetary Rover Wheel Model

To determine the contact force of a rigid wheel rolling on a compliant terrain, the soft soil must be represented by a deformable material model that is in contact with the undeformable shape of the wheel. The geometry of said wheel defines the shape of the soil compaction during impact and the level of this deformation depends on the soil properties as well as the wheel kinematics. Figure 4.1 shows a schematic of the described contact problem which is commonly used to model a rover wheel on soft planetary surfaces.

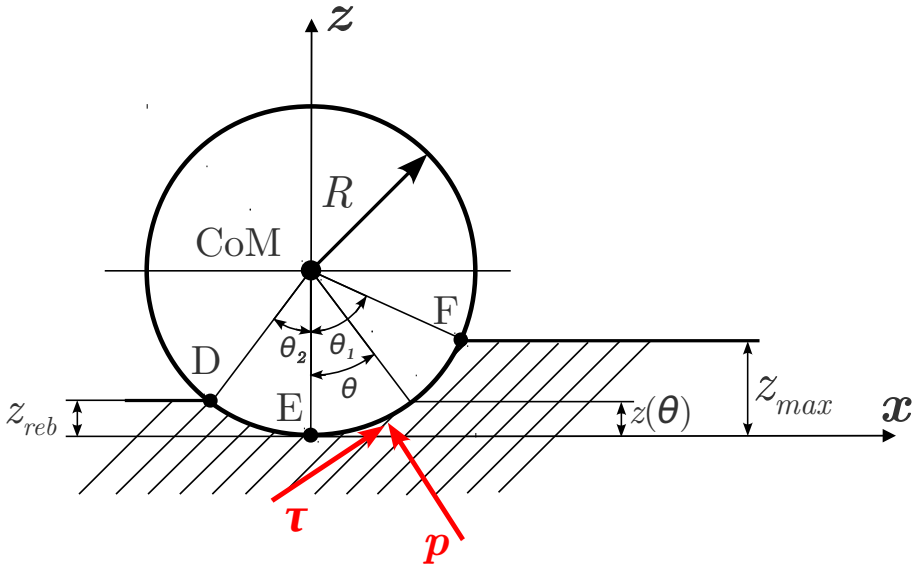

Figure 4.1: Schematic of rigid wheel model

where z_{reb} is the soil rebound occurring in the rear end of the wheel.

4.1 General Rigid Tire Models

The resultant contact forces of the rigid wheel rolling on a compliant terrain are defined by the properties of the soft soil. Hence, the representation of the soft soil is a crucial component in such off-road tire models and the most commonly used soil model is based on Bekker's pressure-sinkage relation shown in Eqn 2.2 (Bekker 1962). With this Bekker soil model, the normal contact pressure that acts along the contact patch can be calculated assuming that the soil deformation under the wheel is known.

Due to the soil plasticity and the fact that the tire is rolling forward, the terrain does not bounce back to its original position when losing contact with the wheel. This means that the contact force calculation has to be broken down based on the division of the contact patch into two sections. As can be seen in Figure 4.1, the rigid wheel compresses the soil up to a maximum sinkage z_{max} represented by section EF. After going through the compression phase and reaching the maximum compression, the soil passes through the elastic rebound phase in which the elastic soil relaxes up to a certain soil rebound z_{reb} which is represented by the contact patch section DE (Wong 2010). The contact patch geometry and therefore the contact dynamics are highly dependent on this soil rebound and it can be used to model energy losses due to the plastic behaviour of the soil. These dependencies are studied and presented in the following sections.

With the assumption of a perfect cylinder as tire geometry and a contact geometry as seen in Figure 4.1, the normal stress distribution p under the wheel can be calculated using the Bekker soil model (Bekker 1962):

$$\begin{aligned} p(\theta) &= \left(\frac{k_c}{b} + k_\phi\right) z(\theta)^n \\ &\text{with} \quad z(\theta) = z_{max} + R(\cos\theta - 1) \end{aligned} \tag{4.1}$$

where k_c and k_ϕ are the cohesive and the frictional soil modulus, respectively, and n is the soil deformation exponent. The tire width is represented by b and z is the soil deformation over the contact patch. R is the tire radius and z_{max} the maximal soil deformation for the corresponding section of the contact patch.

As in the case of the vertical force, the longitudinal force that defines the tractive effort of a vehicle is limited by the soil mechanics. The tangential forces in the soil and tire interface can be calculated by integrating the shear stress over the contact area. The following exponential model can be used to describe the shear stress-strain curve of the

soil (Wong 1993), where τ_{max} is calculated using the Mohr-Coulomb failure criteria.

$$\begin{aligned} \tau(\theta) &= \tau_{max}\left(1 - e^{-\frac{j_x(\theta)}{K_x}}\right) \\ \text{with} \quad \tau_{max} &= c + p(\theta)\ \tan\phi \\ \text{and} \quad j_x(\theta) &= \int_{-\theta_2}^{\theta_1} R\left[1 - (1 - S_{long})\cos\theta\right] d\theta \end{aligned} \tag{4.2}$$

where j_x is the shear deformation or shear strain and K_x is the shear deformation modulus. The parameters c and ϕ represent the soil cohesion and the internal frictional angle, respectively, and S_{long} is the longitudinal tire slip which is defined as shown in Eqn 4.3.

$$S_{long} = 1 - \frac{v_x}{R\,\omega_y} \tag{4.3}$$

where v_x is the longitudinal velocity and ω_y is the wheel spin. The resultant contact forces in longitudinal and vertical directions can be calculated by integrating the normal and tangential stress distributions over the contact patch. Since both of these stress distributions possess parts in both longitudinal and vertical directions, these parts have to be taken into account and added up accordingly for each of the tire forces. The results are the longitudinal and vertical tire forces which can be calculated as shown in Eqn 4.4 and 4.5, respectively.

$$F_x = b\ R \int \tau(\theta)\cos\theta d\theta - b\ R \int p(\theta)\sin\theta d\theta \tag{4.4}$$

$$F_z = b\ R \int p(\theta)\cos\theta d\theta + b\ R \int \tau(\theta)\sin\theta d\theta \tag{4.5}$$

To generate closed-form expressions for these integrals, the volumetric contact model can be used for normal force calculation as explained in the following section. The resulting lumped normal force will allow for faster simulation times, where all the information given by the distributed normal force is now stored in the properties of the penetration volume. These properties are then used to locate the point of action of the contact forces and therefore to calculate the direction of the contact normal.

4.2 Volumetric Tire Model Approaches

Assuming a perfectly linear-elastic soil that fully rebounds back to its original position, the Bekker model resembles an elastic foundation with hyperelastic spring properties. However,

the soil does not behave the same way in rebound as it does when being compacted. In fact, soils show highly plastic behaviour. As a result, the majority of energy that is used to compress the terrain dissipates due to the plastic deformation caused in the soil continuum. The dissipated energy can then be related to the difference between the maximum sinkage of a wheel and the amount the soil rebounds in relaxation. Note that the soil properties under relaxation differ from those when soil is in compression.

When modelling the plastic behaviour of the soil under a rigid wheel, the contact patch is often separated into two different regions which means that not one but two separated integrals have to be solved to calculate the normal force from the normal stress distribution. Therefore, the volumetric model is used to replace the integral of the pressure-sinkage relation such as Bekker's model to find a closed form solution for the normal contact force. The advantage is that if the geometry of each colliding body is known, the volume can be easily calculated. Also, using the hypervolumetric contact model discussed previously, an extension to the model is proposed that can handle plastic behaviour of a hyperelastic foundation in a single volume expression including differing properties for compressive and relaxing states. Replacing the normal force integrals from a Bekker model with closed-form expressions of the volumetric model can significantly reduce computational time of vehicle dynamics simulations.

A number of different soil models can be suggested according to Wong's method (Wong 1993), in which the tire contact patch is separated into front and rear sections and the soil is compacted up to a maximum compression and relaxed up to a certain rebound. In this section, three different tire models with various volumetric contact models are tested with respect to the soil plasticity:

1. **Tire Model I:** same soil properties in compression and relaxation modes
2. **Tire Model II:** different soil properties with same characteristic model for compression and relaxation modes
3. **Tire Model III:** different soil properties with different characteristic model for compression and relaxation modes

In the following sections 4.2.1 to 4.2.3, these wheel models are derived and discussed using an example of a perfect cylinder in contact with smooth and soft terrain. This assumption is chosen for simplicity of representing the results, but is not a restriction to the volumetric contact model.

Centroid of Hypervolume

As stated previously, the volumetric model is used to replace the normal contact force. However, with the introduction of soil plasticity, the dissipated energy is modelled and represented by the soil compaction resistance. With the assumption of the hypervolume centroid as the point of application of the contact forces, this resistive force can be directly derived from the volumetric approach. This means that the normal force is separated into a longitudinal and vertical component based on the normal vector. The normal force can be calculated with the hypervolumetric approach as presented earlier and the contact normal vector is determined using Eqn 4.6.

$$\begin{aligned} \mathbf{n} \quad &= -\frac{\mathbf{r}_{hc}}{|\mathbf{r}_{hc}|} \\ &\text{with} \quad \varphi = \arctan \frac{r_{hc,x}}{r_{hc,z}} \end{aligned} \tag{4.6}$$

where φ is the angle between the normal vector and the vertical direction as can be seen in Figure 4.2. $\mathbf{r}_{hc}$ is the position vector of the hypervolume centroid with respect to the wheel hub frame. The normal force component in x-direction is the soil resistance due to compaction and the component of the normal force in z-direction represents the vertical tire force which supports the wheel load given by the weight and the dynamics of the rover. Assuming a hyperelastic foundation, the hypervolume centroid coordinate in x-direction $\mathbf{r}_{hc,x}$ can be calculated using Eqn 4.7.

$$\mathbf{r}_{hc,x} = \frac{\iint\limits_{S} x_h c\,(S)\ \ f\,(S)^{\eta}\,dS}{V_h}\ \hat{\imath} \tag{4.7}$$

where $x_{hc}\,(S)$ is the x-component of the centroid of the partial volumes under the integral. It is function of the contact patch coordinates. Similarly to the hypervolume problem discussed in the previous chapter, there is no analytical solution for the integral in the numerator of the centroid equation. However, it can be shown that the quotient of

$$\frac{\iint\limits_{S} x_h c\,(S)\ \ f\,(S)^{\eta}\,dS}{\iint\limits_{S} x_c\,(S)\ \ f\,(S)\,dS}$$

behaves in a similar manner as the hypervolume coefficient $c_v(V)$ when plotted over the penetration volume on a double logarithmic scale. In fact, through slight adjustments by introducing a shift factor for the intersection volume V_{int}, the same model can be used to

represent the solution for the x-coordinate of the hypervolume centroid coefficient and Eqn 4.7 yields

$$\mathbf{r}_{hc,x} = \frac{1}{V_h}\left(\frac{V}{V_{int,hcx}}\right)^{A_1(\eta-1)} \iint_S x_c\left(S\right)\ f\left(S\right) dS\ \hat{\imath} \tag{4.8}$$

where $V_{int,hcx}$ is the shift parameter and a function of the intersection volume V_{int} and the nonlinearity exponent η of the hyperelastic foundation. Through substitution of the solution of hypervolume suggested earlier, Eqn 4.8 can be further simplified.

$$\begin{aligned}
\mathbf{r}_{hc,x} &= \frac{1}{c_v(V)}\left(\frac{V}{V_{int,hcx}}\right)^{A_1(\eta-1)} \frac{\iint_S x_c\left(S\right)\ f\left(S\right) dS}{V}\ \hat{\imath} && (4.9)\\
&= \frac{1}{c_v(V)}\left(\frac{V}{V_{int,hcx}}\right)^{A_1(\eta-1)} \mathbf{r}_{c,x} && (4.10)\\
&= \left(\frac{V_{int}}{V_{int,hcx}}\right)^{A_1(\eta-1)} \mathbf{r}_{c,x} && (4.11)
\end{aligned}$$

where $\mathbf{r}_{c,x}$ is the centroid of the penetration volume and the exponential function in front represents the shift of the centroid of the hypervolume caused by the nonlinear properties of the foundation. Assuming a cylinder on flat ground and a fully plastic soil in which the rear end of the wheel does not contact the terrain, the shift parameter $V_{int,hcx}$ can be identified as

$$V_{int,hcx} = \left(1 + (\eta - 1)^2\right)\ V_{int}.$$

For the calculation of the z-coordinate of the hypervolume centroid, Eqn 4.12 has to be considered.

$$\mathbf{r}_{hc,z} = (z_{max} - R) + \frac{\iint_S z_h c\left(S\right)\ f\left(S\right)^{\eta} dS}{V_h}\ \hat{k} \tag{4.12}$$

where $z_{hc}\left(S\right)$ is the z-component centroid of the partial volumes. With the assumption of a homogeneous hypervolume of penetration, the z-centroid can be calculated with Eqn 4.13.

$$\begin{aligned}
\mathbf{r}_{hc,z} &= (z_{max} - R) + \frac{\iint_S \frac{f(S)^{\eta}}{2}\ f\left(S\right)^{\eta} dS}{V_h}\ \hat{k}\\
&= (z_{max} - R) + \frac{\iint_S f\left(S\right)^{2\eta} dS}{2\ V_h}\ \hat{k} && (4.13)
\end{aligned}$$

Through substitution of the proposed solution of hypervolume, Eqn 4.13 yields

$$\mathbf{r}_{hc,z} = (z_{max} - R) + \frac{c_v(V, 2\eta)}{2\ c_v(V, \eta)}\ \hat{k}. \tag{4.14}$$

Once the centroid of the hypervolume of interpenetration is determined, the normal direction vector can be calculated using Eqn 4.6 and the normal force is separated into a vertical and longitudinal component.

To determine the tire forces, the components of the normal force have to be summed up with the components of the tangential force, which is still calculated by integrating the shear stress distribution as explained earlier. The x-component of the tangential force represents the traction force generated in the contact patch and the tangential force component in z-direction also supports the load of the wheel. Moreover, due to the fact that the normal direction is already calculated with the volumetric contact model, the components of the tangential force can be directly projected onto the longitudinal and vertical directions. As a result, the tangential stress distribution has to be integrated only once. Finally, Eqn 4.4 and Eqn 4.5 of the complete tire forces in longitudinal and vertical directions can be replaced by Eqn 4.15 and Eqn 4.16, respectively.

$$\begin{aligned} F_x &= F_{trac} - R_c \ = \ \text{Drawbar Pull} \\ &\text{with } F_{trac} = \int \tau\,(\theta)\, d\theta \sin\varphi \quad \text{and} \quad R_c = k_v V_h \sin\varphi \end{aligned} \tag{4.15}$$

$$F_z = k_v V_h \cos\varphi + \int \tau\,(\theta)\, d\theta \cos\varphi \tag{4.16}$$

where F_{trac} is the generated traction force and R_c is the soil compaction resistance. This method can be used for all three tire models. However, the variations in the described volumetric rigid wheel representations are modelled using different contact geometries for each of the tire models. The difference is simply the shape of the interpenetration volume and its centroid. Both of these together define the absolute value and direction of the normal contact force. The soil plasticity is caused by the compaction due to the rover wheel rolling on the soft soil. The amount of plastic deformation left behind the tire is represented by the soil rebound whose impact on the traction forces as well as the soil resistance is evaluated in the following section using different rigid volumetric wheel models. It should be noted that the presented models do not predict the plastic deformation of the soil, but the soil rebound is assumed to be given and varied to evaluate its impact on the tire dynamics. Also, the three different tire models are explained in detail in the following sections and compared against experimental data from a single wheel testbed (Scharringhausen et al. 2009a). A rigid smooth wheel (radius $R = 125\ mm$, width $b = 100\ mm$) with a vertical

wheel load of 70 N was translated at a velocity of $v_x = 10\ mm/s$ through fine and dry quartz sand. Numerous measurements were taken by prescribing the angular velocity of the tested wheel in order to create wheel slip varying from 5% to 95%. For the experiments, the same slip definition as used in the calculation of the tangential forces of the presented tire models was assumed. The following sections discuss how the volumetric model can be utilized to calculate the normal forces generated in the wheel/soil interface for the three different tire models.

4.2.1 Tire Model I

The first version of the volumetric rigid tire model is based on the assumption that the soil possesses the same properties along the full extent of the contact patch. A schematic of this tire model I can be seen in Figure 4.2.

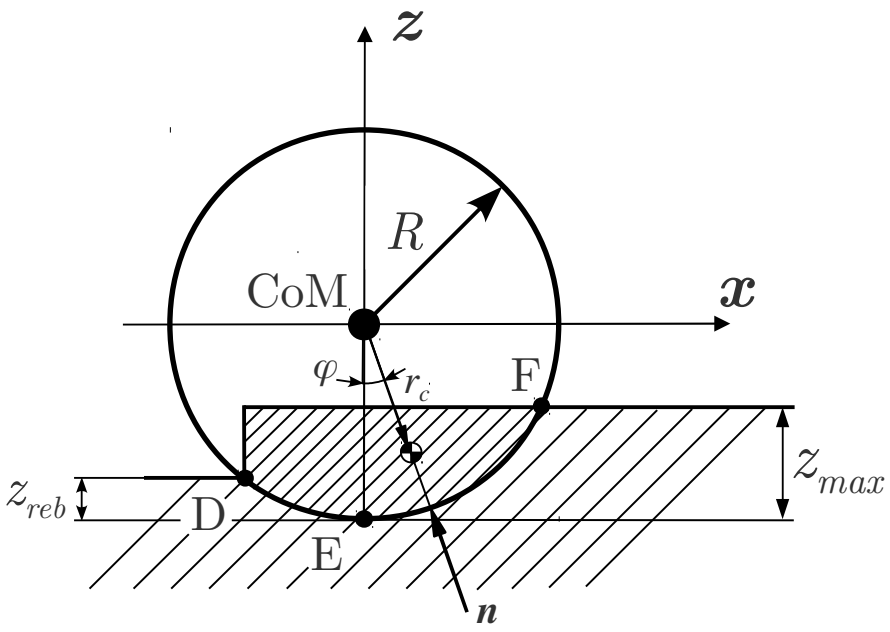

Figure 4.2: Schematic of tire model I

It can be seen that the soil is compressed all the way from the original soil position throughout the entire contact patch even after it passes through the maximum sinkage z_{max}. The soil rebound then influences the normal contact force in such a way that the remaining

penetration volume is cut off when the tire loses contact with the soil. This also means that the normal pressure distribution suddenly jumps to zero after losing contact with the rebounding soil. With the assumption of a perfect cylinder and Bekker pressure-sinkage relation, the normal stress distribution in the contact patch is

$$\begin{aligned} p\left(z\right) = \quad & k_{Bekker}\ z\left(x\right)^{n} \quad \text{for} \quad x_D \leq x \leq x_F \\ & \text{with} \quad z\left(x\right) = \sqrt{R^2 + x^2} - \left(R - z_{max}\right) \end{aligned} \tag{4.17}$$

where x_F and x_D are the integration limits based on the contact point in the front and the rear of the wheel, respectively (see Figure 4.2). The normal force contributions to the tire forces can then be calculated by integrating Bekker's pressure-sinkage relation

$$\mathbf{F}_{n,Bekker} = k_{Bekker}\ b \int_{z_D}^{z_F} z\left(x\right)^{n}\, dz\ \hat{\imath} + k_{Bekker}\ b \int_{x_D}^{x_F} z\left(x\right)^{n}\, dx\ \hat{k}$$

or by using the hypervolumetric contact model and Eqn 4.18.

$$\mathbf{F}_{n,vol} = k_{Bekker}\ V_h\ \sin\varphi\ \hat{\imath} + k_{Bekker}\ V_h\ \cos\varphi\ \hat{k} \tag{4.18}$$

To test the volumetric rigid tire model for different soils, the resultant drawbar pull F_x for this tire model is evaluated for various amounts of soil rebound using Eqn 4.15, and the penetration volume indicated in the schematic of Figure 4.2. For this version of the tire, the volume and the centroid are calculated numerically for the purposes of the simulation. The drawbar pull is the effective driving force that is generated in the contact patch. It is calculated by summing up the traction and resistance forces, as shown in Eqn 4.15. For the measured tire states, the soil compaction resistance R_c is the dominant dissipative force. Therefore, other resistive forces, e.g. a bulldozing force, are not considered in this section. The results are plotted and compared against experimental data retrieved from (Scharringhausen et al. 2009a) and can be seen in Figure 4.3.

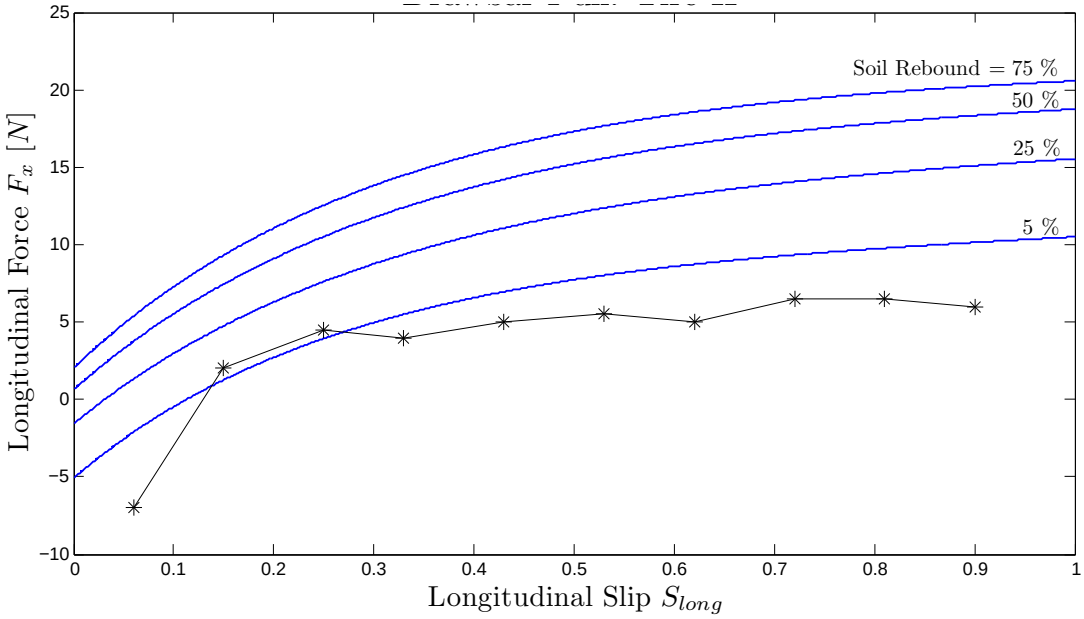

Figure 4.3: Tire I: Drawbar Pull vs. Slip with respect to various soil rebounds in comparison with a tested rigid tire

In the plot seen in Figure 4.3, the continuous lines illustrate the drawbar pull as predicted by this tire model and the measurements are noted by the asterisks. The results show a significant impact of the soil rebound on the effective traction force that can be generated in the contact patch. The impact of the soil rebound in this tire model appears to be more significant in the lower soil rebound region. This is due to the fact that the penetration volume barely changes for small variations in soil rebound for higher amounts of rebound. Also, the results of this tire model do not agree very well with the experimental results. This suggests that treating the soil as a material with unchanged properties over the entire contact patch may not lead to realistic results.

4.2.2 Tire Model II

This version of a rigid rover wheel model is based on the fact that the soil properties differ when the soil is in relaxation mode compared to soil under compression. A schematic of the resulting penetration volume is illustrated in Figure 4.4.

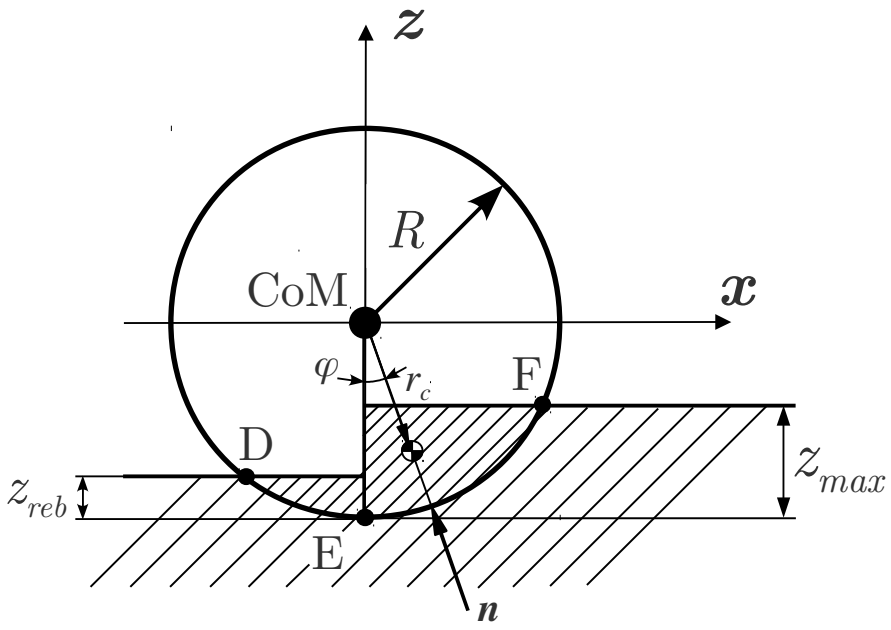

Figure 4.4: Schematic of tire model II

The schematic shows that the soil is compressed up until the maximum sinkage z_{max} (shown in the front section of the tire) from which it rebounds up to a certain soil rebound z_{reb} (shown in the rear section of the tire). This means that the normal force under the rear section is based on pressure distribution where the maximal soil displacement is equal to the soil rebound z_{reb}. With the assumption of the perfect cylinder and Bekker pressure-sinkage relation, the normal stress distribution can be expressed as a piecewise function.

$$p(z) = \begin{cases} k_{Bekker}\, z_1(x)^n & \text{for } 0 \le x \le x_F \\ k_{Bekker}\, z_2(x)^n & \text{for } x_D \le x \le 0 \\ 0 & \text{otherwise} \end{cases} \tag{4.19}$$

$$\text{with } z_1(x) = \sqrt{R^2 + x^2} - (R - z_{max})$$
$$\text{and } z_2(x) = \sqrt{R^2 + x^2} - (R - z_{reb})$$

and normal force contributions to the tire forces can be calculated by integrating Bekker's pressure-sinkage relation over the piecewise contact patch

$$\mathbf{F}_{n,Bekker} = k_{Bekker}\, b \left(\int_{z_D}^{z_E} z_2(x)^n\, dz + \int_{z_E}^{z_F} z_1(x)^n\, dz \right) \hat{\imath}$$
$$+ \; k_{Bekker}\, b \left(\int_{x_D}^{x_E} z_2(x)^n\, dx + \int_{x_E}^{x_F} z_1(x)^n\, dx \right) \hat{k}$$

or by using the hypervolumetric contact model and Eqn 4.20.

$$\mathbf{F}_{n,vol} = k_{Bekker}\, V_h\, \sin\varphi\, \hat{\imath} + k_{Bekker}\, V_h\, \cos\varphi\, \hat{k} \tag{4.20}$$

For this piecewise volume, explicit solutions can be found using the hypervolume coefficient and the hypervolume centroid model as derived previously. The hypervolume for this particular tire model can be calculated using

$$\begin{aligned} V_h &= \sum_{i=1}^{2} V_{h,i} = V_{h,1} + V_{h,2} \\ &= \frac{1}{2}\, c_v\left(V\left(z_{max}\right)\right) V(z_{max}) + \frac{1}{2}\, c_v\left(V\left(z_{reb}\right)\right) V(z_{reb}). \end{aligned} \tag{4.21}$$

The components of the hypervolume centroid vector are

$$\begin{aligned} \mathbf{r}_{hc} &= \frac{\sum_{i=1}^{2} \mathbf{r}_{hc,i}\, V_{h,i}}{\sum_{i=1}^{2} V_{h,i}} \\ &= \frac{\mathbf{r}_{hc,1}\, V_{h,1} + \mathbf{r}_{hc,2}\, V_{h,2}}{V_{h,1} + V_{h,2}}. \end{aligned} \tag{4.22}$$

The components of the volumetric normal tire force are calculated using the closed-form expressions in Eqns 3.20 and 4.6.

To evaluate the influence of the soil rebound of this type of volumetric tire model, the resultant drawbar pull is calculated with Eqn 4.15 by assuming the volume of interpenetration and its centroid according to the tire schematic shown in Figure 4.4. The closed-form solution of the hypervolume and its centroid are calculated using Eqns 4.21 and 4.22, respectively. The different results for various amounts of soil rebound are plotted and also compared against the previous experiments (see Figure 4.5).

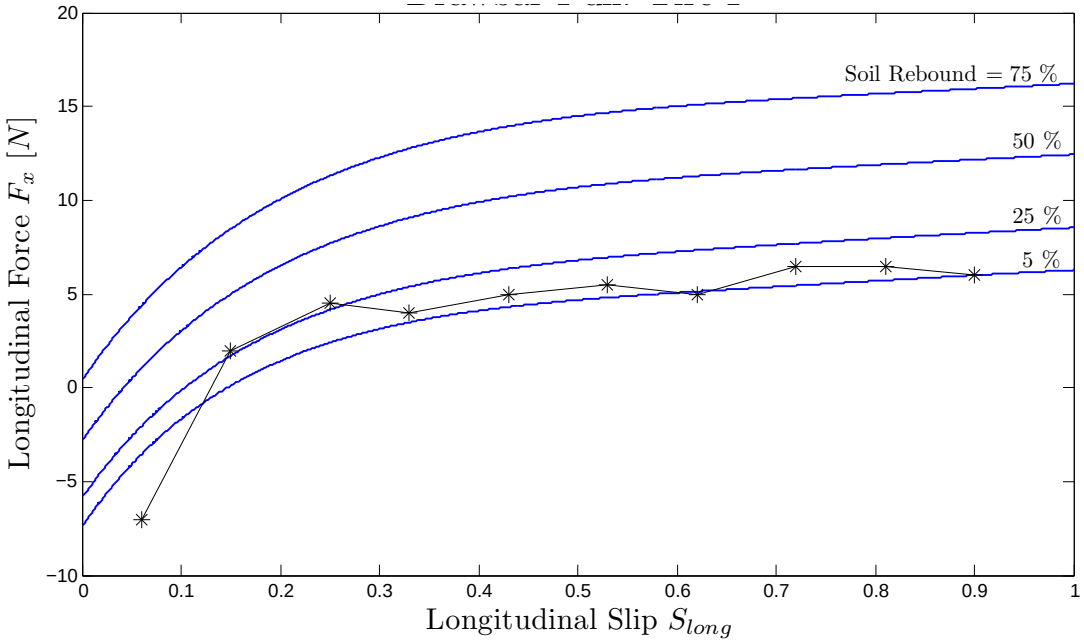

Figure 4.5: Tire II: Drawbar Pull vs. Slip with respect to various soil rebounds in comparison with a tested rigid tire

In the results plot shown in Figure 4.5, it can be seen that the soil rebound significantly impacts the effective traction force generated in the contact patch. Also, the tire model considering a rather low amount of soil rebound is in best agreement with the experimentally gained results. This was expected due to the naturally low rebound properties of the dry quartz sand. As a result of the assumption made in this version of the rigid wheel model, the normal stress distribution is discontinuous in the lowest point on the wheel circumference where the soil switches from compression to relaxation. To prevent this unnatural behaviour, the following volumetric contact model is proposed.

4.2.3 Tire Model III

In this particular implementation of the volumetric rigid wheel model, it is assumed that not only the material properties but also the characteristic material model changes when the soil transitions from compression into relaxation. Again, a piecewise pressure-sinkage relation is chosen to represent the soil under the rigid wheel. Based on a typical response of a mineral terrain to a repetitive loading cycle (as presented by Wong (1993) and shown in Figure 4.6), a nonlinear compression model and a linear relaxation model are chosen.

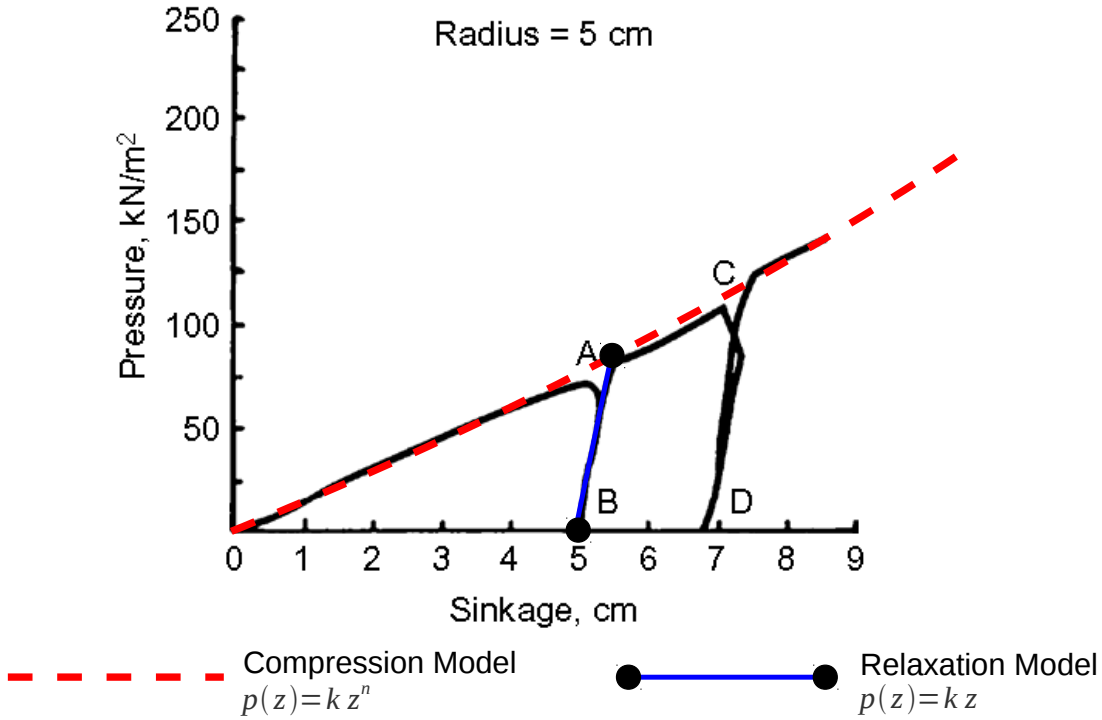

Figure 4.6: Characteristic soil model based on repetitive loading experiments

With the assumption of a perfect cylinder and Bekker soil model for the compression, the normal stress distribution in the contact patch is

$$p(z) = \begin{cases} k_{Bekker}\, z_1(x)^n & \text{for } 0 \le x \le x_F \\ k_{relax}\, z_2(x) & \text{for } x_D \le x \le 0 \\ 0 & \text{otherwise} \end{cases} \tag{4.23}$$

$$\text{with } z_1(x) = \sqrt{R^2 + x^2} - (R - z_{max})$$
$$\text{and } z_2(x) = z_1(x) - z_{reb}.$$

where k_{relax} is the foundation stiffness of the soil in relaxation. Assuming that the plastic behaviour is known, this stiffness can be calculated as the slope of the linear curve connecting the state of the soil under current maximum compression and the state of the soil

in which it has fully relaxed (see Figure 4.6).

$$\begin{aligned} k_{relax} &= \frac{p_1(z_{max}) - \cancelto{0}{p_2(z_{reb})}}{z_{max} - z_{reb}} \\ &= k_{Bekker} \frac{z_{max}^n}{z_{max} - z_{reb}} \end{aligned} \tag{4.24}$$

with the introduction of a soil rebound parameter γ as a percentage representation of the maximum sinkage, the foundation stiffness k_{relax} becomes

$$\begin{aligned} k_{relax} &= k_{Bekker} \frac{z_{max}^n}{z_{max} - (1-\gamma) z_{max}} \\ &= k_{Bekker} \frac{z_{max}^{(n-1)}}{\gamma}. \end{aligned} \tag{4.25}$$

substituting this expression for k_{relax} in Eqn 4.23 yields

$$p(z) = \begin{cases} k_{Bekker}\ z_1(x)^n & \text{for} \quad 0 \le x \le x_F \\ k_{Bekker} \frac{z_{max}^{(n-1)}}{\gamma} \left(z_1(x) - (1-\gamma) z_{max}\right) & \text{for} \quad x_D \le x \le 0 \\ 0 & \text{otherwise} \end{cases} \tag{4.26}$$

$$\text{with} \quad z_1(x) = \sqrt{R^2 + x^2} - (R - z_{max}).$$

By assuming that the relaxation model also behaves in a nonlinear manner like the compression model, the same model for both modes can be assumed when introducing an equivalent sinkage profile $z_{eq}(x)$ for the soil under the rear end of the wheel. The pressure-sinkage relation of Eqn 4.26 then becomes

$$p(z) = \begin{cases} k_{Bekker}\ z_1(x)^n & \text{for} \quad 0 \le x \le x_F \\ k_{Bekker}\ z_{eq}(x)^n & \text{for} \quad x_D \le x \le 0 \\ 0 & \text{otherwise} \end{cases} \tag{4.27}$$

$$\text{with} \quad z_1(x) = \sqrt{R^2 + x^2} - (R - z_{max})$$

$$\text{with} \quad z_{eq}(x) = \left(\frac{z_{max}^{(n-1)}}{\gamma} \left(z_1(x) - (1-\gamma) z_{max}\right) \right)^{\frac{1}{n}}.$$

With the introduction of the equivalent sinkage profile, the same characteristic model can be used again and still obtain a continuous normal pressure distribution under the wheel. A schematic of the equivalent penetration volume of this tire model III is illustrated in Figure 4.7.

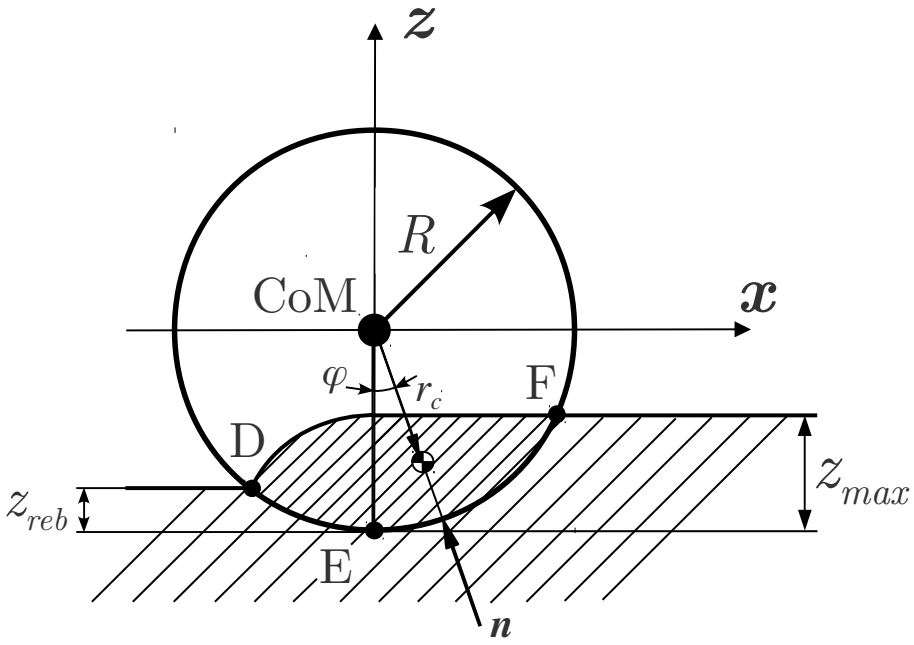

Figure 4.7: Schematic of tire model III

As a result of using the same characteristic model, the closed-form solution of the hypervolumetric contact model as derived earlier for a perfect cylinder on a flat terrain can still be used. However, the soil rebound parameter γ has to be included into the model. It can be shown that this is simply done by introducing another correction function for the intersection volume V_{int}. By replacing the intersection volume with an adjusting parameter $V_{int,plastic}$ that is a function of the plasticity parameter of soil rebound and the intersection volume of the fully elastic model, it can be shown that the new parameter for a cylinder in contact with soft and plastic soil can be calculated using Eqn 4.28 (see Appendix A).

$$\begin{aligned} V_{int,plastic} &= f(\gamma)\, V_{int} \\ &= (-0.345\gamma + 0.897\sqrt{\gamma} + 0.458)\, V_{int} \end{aligned} \tag{4.28}$$

Substituting this parameter into the contact model, the normal force and the normal direction vector can be calculated using Eqns 3.20 and 4.6 of the hypervolumetric approach, respectively. The schematic shows the penetration volume used for this version of the tire model which is defined by sinkage profiles shown in Eqn 4.27. Eqns 4.15 and 4.16 are used to calculate the tire forces based on this particular penetration volume. The results are plotted in Figure 4.8.

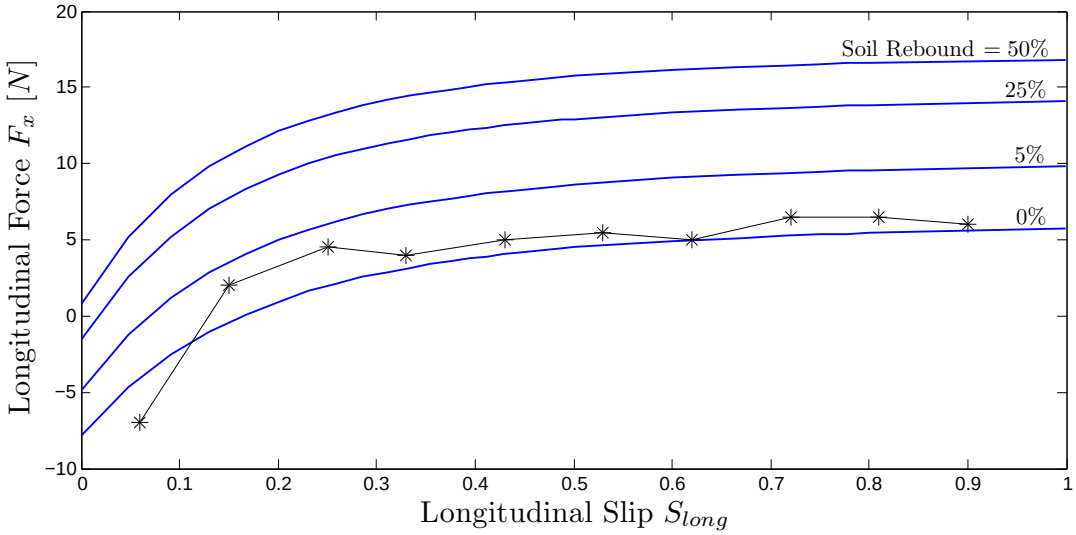

Figure 4.8: Tire III: Drawbar Pull vs. Slip with respect to various soil rebounds in comparison with a tested rigid tire

As in the earlier displayed volumetric tire models, the results of this 3rd version reveal a similar significance of the soil rebound. However, it can be seen that the effective longitudinal force is more sensitive to small changes of the soil rebound for highly plastic soils with lower soil rebound values. This suggests that the longitudinal force components for this tire model are predicted with different sensitivities to soil rebound in the lower region of this parameter. Overall, it can be said that this tire model predicts a slightly lower value of a soil rebound parameter γ compared to the previous tire model II. The impact of the relaxation properties of the soil on each of the components of the longitudinal force and the drawbar pull itself are discussed in more detail in the following section.

4.2.4 Comparison of volumetric approaches

Besides the direct influence of the soil rebound on the normal force calculation in all three of the discussed volumetric rigid tire models, the amount of soil rebound also indirectly impacts the calculation of the tangential forces as shown previously. Therefore, both the soil compaction resistance R_c and the traction force F_{trac}, which are the two force components of the effective longitudinal force F_x, are influenced by the plastic deformation of the soil that remains after the wheel rolls over the soft terrain.

The soil rebound directly influences the normal force calculation by defining the penetration volume and shifting the centroid. Assuming the same wheel load, the soil rebound influences the normal force by changing the direction of the contact normal. The angle between the contact normal and the vertical direction decreases with increasing soil rebound. A smaller angle from the vertical direction means that a larger amount of the normal force supports the wheel load and a smaller soil compaction resistance is the result. Another result of this scenario is the decreasing tire sinkage and thus a smaller contact patch and generated traction force. This tendency is counteracted by the assumption that an increase of soil rebound also increases the contact patch size as a result of the altered contact patch angles θ_1 and θ_2 (see Figure 4.1). To evaluate the compaction resistance and the traction force, these forces are calculated for each of the volumetric tire models at a constant slippage of 25% and by varying the soil rebound from 0% to 100% of the maximum sinkage. The wheel load is kept at a constant value of $70N$ and the results can be seen in Figures 4.9 and 4.10. Finally, the effective driving force F_x, also known as the drawbar pull, is calculated and evaluated under the same conditions. The results can be seen in the plot of Figure 4.11.

Figure 4.9 shows the effect on soil compaction resistance when the soil rebound is increased from 0% to 100% for each tire model.

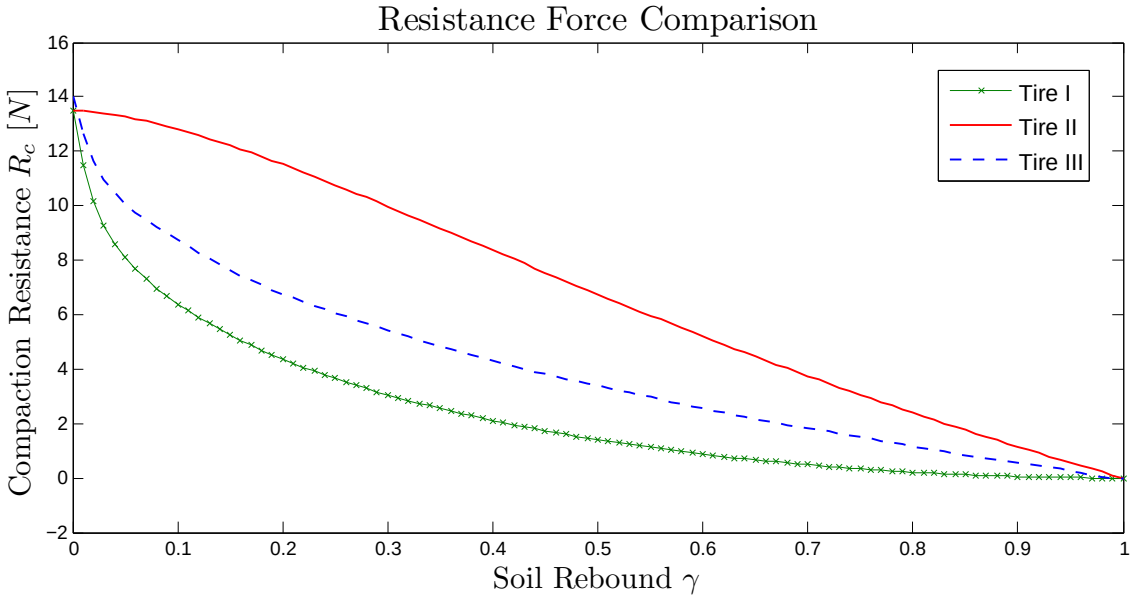

Figure 4.9: Comparison of compaction resistance R_c with respect to soil rebound

As expected from the geometry of the penetration volume, all three models start and finish with the same value. For all three versions of the tire model, the plots depict a decreasing trend with respect to an increasing soil rebound until the soil resistance settles to zero for 100% of soil rebound. This is due to the fact that the contact normals in each tire model are aligned with the vertical direction for this soil state which is a result of the geometry of the penetration volume. Whereas tire model II decreases almost linearly with increasing soil rebound, the plot shows that tire models I and III are more sensitive to changes in the lower soil rebound region as suggested by the results shown in the previous section.

Figure 4.10 shows the effect on the generated traction force when the soil rebound is increased from 0% to 100%.

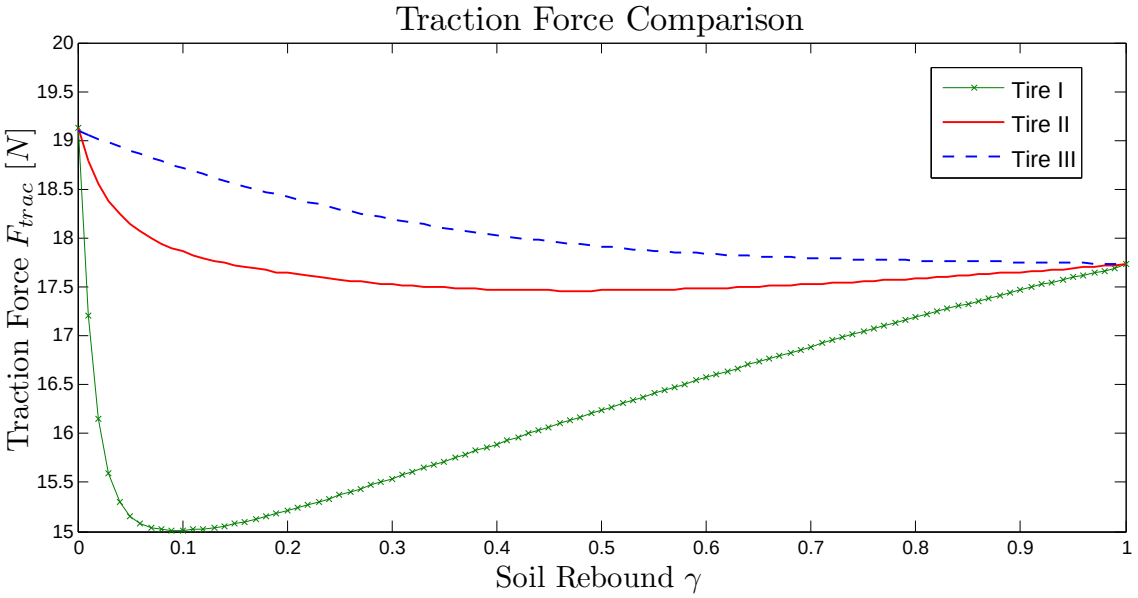

Figure 4.10: Comparison of traction force F_{trac} with respect to soil rebound

It can be seen that the traction force for all three tire models begins with the same force value and decreases afterwards. This drop of traction force is due to the decreasing size of the contact patch due to the increase in soil rebound discussed earlier. This effect appears to have the biggest impact on tire model I. Also, it has less but still substantial impact on tire model II. The third tire model however, shows the least sensitivity to this effect. This is also due to the fact that the three tire models show a reversed sensitivity to the counteracting increase of the contact patch size as a result of the changing penetration

volume geometry. Eventually, this counteracting effect overtakes the decrease in contact patch size and all three tire models settle to the same amount of traction force at a value of 100% of soil rebound. However, it can be observed that the change in traction force is not very significant for any of the three model types compared to the previously observed changes in the soil compaction resistance with respect to the soil rebound parameter γ.

As a conclusive diagram, the drawbar pull is plotted against the soil rebound which can be seen in Figure 4.11. The plot of the drawbar pull shows that the hypervolumetric rigid wheel models II and III predict similar effective longitudinal forces for soil with very high relaxation properties, but diverge significantly for other soils. The predicted drawbar pull in the first version of the volumetric rigid tire model appears to be significantly lower for most soils. It should be mentioned that in the region of 0 to 20% soil rebound that covers most soils, the third tire model, which is expected to be most realistic, appears to be most sensitive with respect to changes in the plastic behaviour of soils.

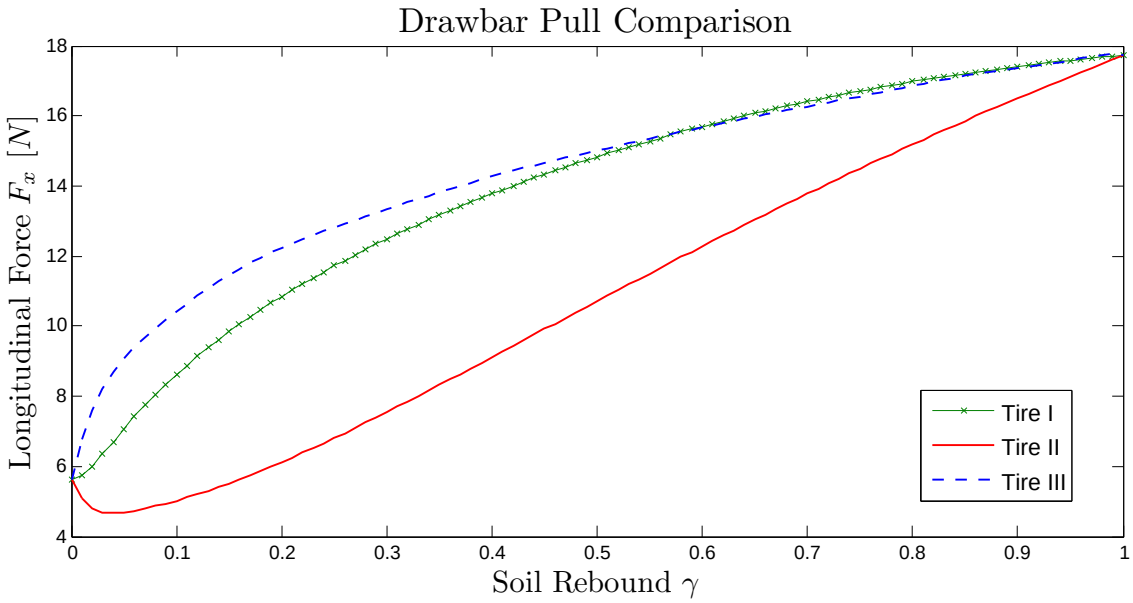

Figure 4.11: Comparison of drawbar pull $F_x$with respect to soil rebound

4.2.5 Volumetric tangential force model

To entirely utilize the computational advantage of the volumetric approach to model the contact between a rigid planetary rover wheel and the soft soil, the calculation of tangential

contact force, which requires the integration of the shear stress distribution, has to be simplified to an explicit expression. Usually determined by integrating the shear stress as a function of the normal stress distribution and the shear displacement over the contact patch, this classical terramechanics approach shows limits for certain contact conditions (Senatore and Iagnemma 2011). In fact, for large contact patches and/or under high slip conditions, the shear limit in the contact patch is rapidly reached and the resultant nearly constant shear stress leads to a tangential force model with the longitudinal velocity and slip as its main influential factors. With that in mind and inspired by tire models commonly used in road vehicle dynamic simulations in which the traction force is a function of longitudinal velocity and slip, a fully volumetric soil shear force model can be achieved by assuming a friction like model with an upper shear force limit as shown in Eqn 4.29.

$$F_t = F_{\tau_{max}} f\left(v_x, S_{long}\right) \tag{4.29}$$

where $F_{\tau_{max}}$ is the shear force limit defined by the Mohr-Coulomb envelope and the function $f\left(v_x, slip\right)$ has to be determined through experimental results. In fact, if single wheel test bed measurements are available, this type of model definition seems more intuitive than curve-fitting the shear stress as a function of the shear displacement. However, the resultant curve-fit requires the use of parameters that are related to the contact pairing rather than to the soil only. For most planetary rover operations, the model can be further simplified with longitudinal slip as the only kinematic dependency variable. Hence, the proposed volumetric tangential force model as a hyperbolic function of longitudinal slip shown in Eqn 4.30 is based on typical single wheel test results (Scharringhausen et al. 2009a).

$$\begin{aligned} F_t &= F_{\tau_{max}} \tanh\left(\frac{S_{long}}{K_{v_x}}\right) \\ \text{with} \quad F_{\tau_{max}} &= AC + F_n \tan\phi \end{aligned} \tag{4.30}$$

where A is the contact patch area, and C and ϕ are the soil parameters of cohesion and internal friction angle, respectively. The only curve-fit parameter used in this representation of the tangential force is the dimensionless shear velocity modulus K_{v_x}. This completes the hypervolumetric model of the tire forces which are now fully represented using the properties of the volume of interpenetration.

$$F_x = F_t \cos\varphi - F_n \sin\varphi \tag{4.31}$$

$$\begin{aligned} F_z &= F_n \cos\varphi + F_t \sin\varphi \\ \text{with} \quad F_n &= k_v V_h \\ \text{and} \quad \varphi &= \frac{\left|\mathbf{r}_{hc,x}\right|}{\left|\mathbf{r}_{hc,z}\right|} \end{aligned} \tag{4.32}$$

Single-Wheel Simulation and Results

To prove that this model can be used to model the contact force between a planetary rover wheel and the soft soil, these equations are implemented in a simulation of a single wheel test with respect to the assumption corresponding to the tire model III as explained earlier. Assuming a soil rebound parameter of $\gamma = 2.5\%$ as identified in earlier simulations using the Janosi-Hanamoto equations, the results of this model are compared against the same experimental results from the DLR single wheel test results (see Figure 4.12).

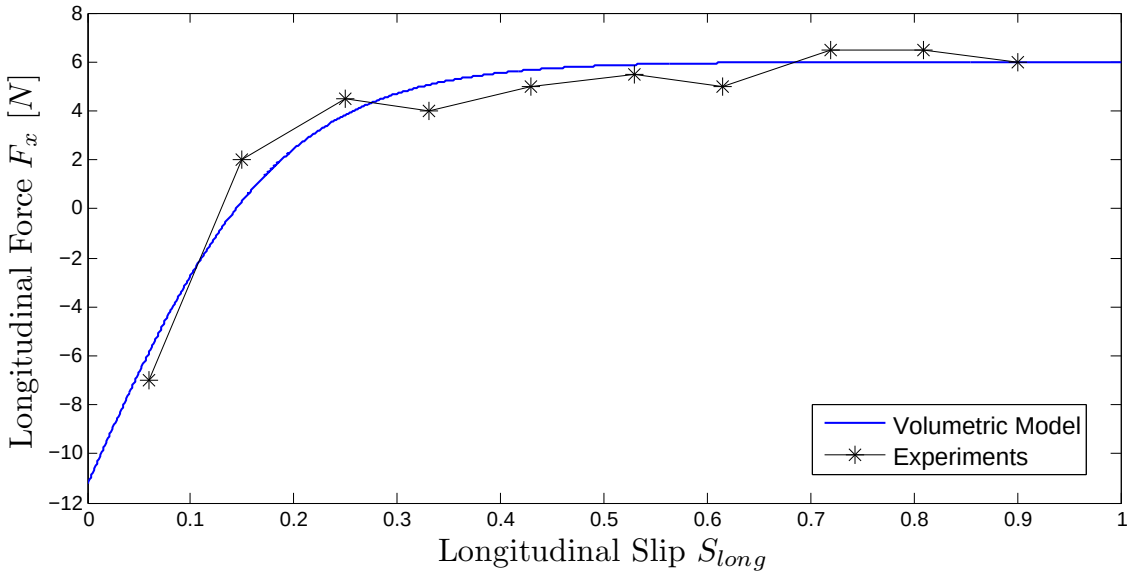

Figure 4.12: Comparison of hypervolumetric drawbar pull force with DLR single wheel test bed experiments

Assuming a shear velocity modulus of $K_{v_x} = 0.185$, the plot in Figure 4.12 compared against the experimental results proves that the proposed hypervolumetric contact model can be used to predict the contact forces in the wheel/soil interface.

Chapter 5

Flexible Planetary Rover Tire Model

The previous chapter shows how a volumetric approach can be used to model the contact forces of a rigid wheel interfering with highly deformable terrain. As a result, a closed-form solution for the contact forces is found which can be applied as a lumped force to the rigid body of the rover wheel. The crucial assumption for that approach is that deformation only occurs on one side so that the penetration volume can be related to the large deformation of one homogenous soil continuum due to the contact with the rover wheel. When assuming a flexible wheel in contact with the soft soil, the assumption of the soil bearing the only deformation is no longer valid. The deformed state of both the wheel and the soil has to be determined before the volumetric contact model can be applied to a contact problem in which both contacting bodies deform and the deformations are governed by different constitutive relations. To calculate the deformation of the flexible wheel, distributed forces generated in the contact with the hyperelastic foundation have to be considered. Once the deformation of the wheel is determined, the new contact interface between the flexible wheel and the soft soil can be defined and the hypervolume model can be applied. For that purpose, a flexible planetary rover wheel model based on a distributed parameter model of a flexible circular beam in contact with a foundation of springs is proposed. The quasi-static analysis of the distributed parameter model of the flexible wheel in contact with the soft soil is performed to find the equilibrium state between the two contacting bodies. The quasi-static solution fully defines the new contact geometry which allows for the use of the hypervolumetric contact model as described in the previous chapter. The following sections present the derivation of the equations of motion of the flexible planetary rover wheel and the necessary steps to be able to apply the volumetric approach to this contact problem.

5.1 Flexible Euler-Bernoulli Tire Model on Soft Soil

The flexible wheel model presented in the following sections is inspired by the ExoMars rover wheel that was designed for a European exploration mission to give the rover a tractive advantage over rigid planetary rover wheels as they are used in most recent North American missions. A picture of the ExoMars rover wheel design is shown in Figure 5.1 as it was tested and presented in (Scharringhausen et al. 2009a, b). These cylindrical flexible wheels are based on a design in which the tire tread is connected to a rigid wheel hub via radially distributed flexible spokes.

Figure 5.1: Flexible metal wheel used in ExoMars (Patel et al. 2010)

To model the dynamics of such a flexible wheel design, a distributed parameter approach is chosen to represent the deformations of the cylindrical wheel with flexible spokes. Using Euler-Bernoulli circular beam equations (Nelson 1962), the treadband of the rover wheel is modelled as a thin elastic ring with evenly distributed mass and material properties. The sheet metal spokes are represented with radial and horizontal springs that connect the rigid wheel hub and inner circumference of the ring. A schematic of the developed tire model can be seen in Figure 5.2.

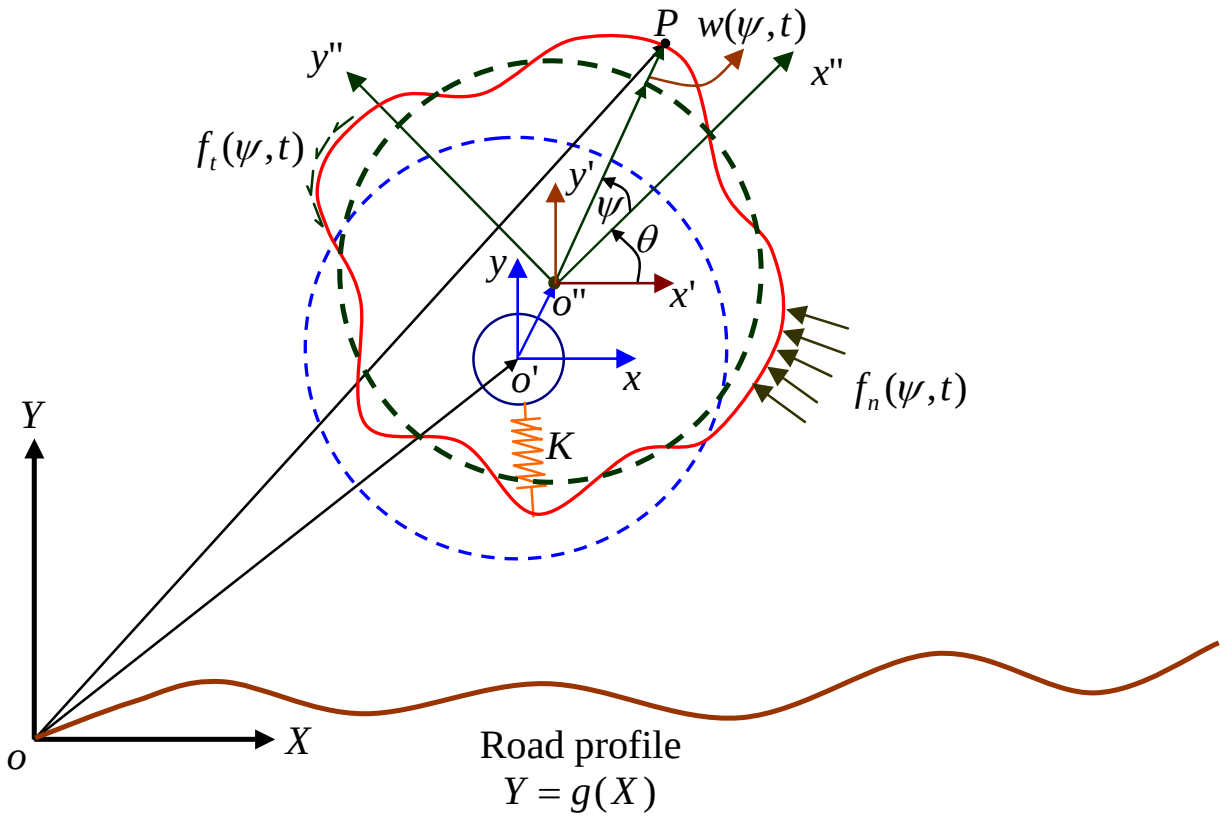

Figure 5.2: Schematic of the flexible wheel

A similar approach was used by Gong (1993) to model common automotive tires rolling on rigid road surfaces. However, to model the dynamics of planetary rovers, the highly compliant terrain has to be considered (Bekker 1969; Wong 2010). To capture the terrain compression under the rover wheel, the soft soil is modelled using a hyperelasto-plastic foundation (as presented in section 4.2.3) which interacts with the outer surface of the flexible ring tire. Furthermore, the Janosi-Hanamoto equation (see Eqn 2.7) is used to represent the tangential force generated in the tire contact patch. The contact forces are then represented by a line load that is applied to the flexible wheel in the wheel/soil interface. Moreover, the proposed rover wheel model is normalized to reduce simulation time and prepare the equations of motion for possible future parameter studies. The following sections present a detailed derivation of the system equations and the non-dimensional equivalent of said equations.

5.2 Equations of motion

To derive the equations of motion of the deformable planetary rover wheel, a physical system as shown in the schematic of Figure 5.2 is considered during the modelling process. The problem is reduced to planar motion of a tire with a wheel hub mass M and moment of inertia J. The hub is subjected to external forces F_{hX}, F_{hY} in X and Y directions and a torque T_h in θ direction, which is considered positive in the counterclockwise direction. These external loads represent the interaction between the wheel, the rover and the driving torque, respectively. The tread of the planetary rover tire is connected to the wheel hub through a continuum of radial springs of stiffness K. For clarity, only one spring is illustrated in the schematic of Figure 5.2. The wheel has a mass density of $\rho\, A\, R$, and a flexural rigidity EI, where ρ is the density, A is the area of the cross section of the sheet metal representing the tire tread, and R is the mean radius. The wheel is subjected to external radial $f_n(\psi, t)$ and tangential $f_t(\psi, t)$ forces. The only external forces acting on the flexible part of the tire are the contact forces generated in the interface between the tire tread and the ground $g(X)$.

A floating reference frame and Lagrange's equations are used to formulate the equations of motion. The rotational coordinate θ is assumed to be common for the hub and the wheel, i.e, no relative rotation between wheel and hub is allowed. The translational motion of the hub is given by x and y and that of the wheel is given by x' and y'. The continuous radial deformation is defined by $w(\psi, t)$, where ψ is the angular coordinate in the rotating coordinate frame $x''-y''$. Four coordinate systems are used in the formulation. The inertial frame $X-Y$, a frame connected to the wheel hub $x-y$ that measures the translation of the hub, a frame connected to the center of the flexible wheel $x'-y'$ that measures the translation of the tread relative to the hub, and a rotating frame $x''-y''$ connected to the center of the wheel is used to measure its rotation. The location vector $\mathbf{p} = \overline{OP}$ defines the position of a point P with arc length $d\psi$. Its components in the inertial frame $X-Y$ can be written as

$$\mathbf{p} = \left\{ \begin{array}{c} x + x' \\ y + y' \end{array} \right\} + \mathbf{R} \left\{ \begin{array}{c} [R + w(\psi, t)] \cos\psi \\ [R + w(\psi, t)] \sin\psi \end{array} \right\} \tag{5.1}$$

where $\mathbf{R}$ is the rotation matrix and is given by

$$\mathbf{R} = \left[\begin{array}{cc} \cos\theta & -\sin\theta \\ \sin\theta & \cos\theta \end{array} \right] \tag{5.2}$$

By differentiating the above expression with respect to time, the velocity vector $\dot{\mathbf{p}}$ of the

point P resolved in $X-Y$ frame is derived as

$$\dot{\mathbf{p}} = \begin{Bmatrix} \dot{x}+\dot{x}' \\ \dot{y}+\dot{y}' \end{Bmatrix} + \dot{\theta}\frac{\partial \mathbf{R}}{\partial \theta}\begin{Bmatrix} [R+w(\psi,t)]\cos\psi \\ [R+w(\psi,t)]\sin\psi \end{Bmatrix} + \mathbf{R}\begin{Bmatrix} [\dot{w}(\psi,t)]\cos\psi \\ [\dot{w}(\psi,t)]\sin\psi \end{Bmatrix} \tag{5.3}$$

To use Lagrange's principle, expressions for the kinetic and potential energy are required. The kinetic energy of the system can be determined with the following equation:

$$T = \frac{1}{2}M\dot{x}^2 + \frac{1}{2}M\dot{y}^2 + \frac{1}{2}J\dot{\theta}^2 + \frac{1}{2}\rho AR\int_0^{2\pi}\dot{p}_X^2 d\psi + \frac{1}{2}\rho AR\int_0^{2\pi}\dot{p}_Y^2 d\psi \tag{5.4}$$

Assuming Euler-Bernoulli beam theory with inextensibility constraint (Nelson 1962; Gong 1993), the potential energy expression consists of three parts: the strain energy stored in the radial springs, the strain energy due to the bending of the flexible wheel tread and the potential energy stored in the mass of the overall tire system. All of these together result in the following expression

$$\begin{aligned} V = \; & \frac{1}{2}\frac{EI}{R^3}\int_0^{2\pi}\left(\frac{\partial^2 w}{\partial\psi^2}+w\right)^2 d\psi + g\,\rho\,A\,R\int_0^{2\pi}p_Y(\psi,t)d\psi \\ & + \frac{1}{2}K\int_0^{2\pi}(x'+w\cos\psi)^2+(y'+w\sin\psi)^2 d\psi + g\,M\,y \end{aligned} \tag{5.5}$$

The solution of the elastic deformation $w(\psi,t)$ of the flexible wheel around the rigid body motion is expanded as the Fourier series of the fundamental shapes of the circular Euler-Bernoulli beam and can be written as

$$w(\psi,t) = \sum_{k=1}^{N} a_k(t)\sin(k\psi) + b_k(t)\cos(k\psi) \tag{5.6}$$

It should be noted that the control variable k of this series starts from 1 which eliminates the rigid body modes from the solution of the flexible wheel. This is due to the fact that the rigid body motion of the flexible wheel is modelled using the coordinates x' and y' of the corresponding body-fixed reference frame. The first ten flexible modes of the circular beam according to Eqn 5.6 are shown in Figure 5.3.

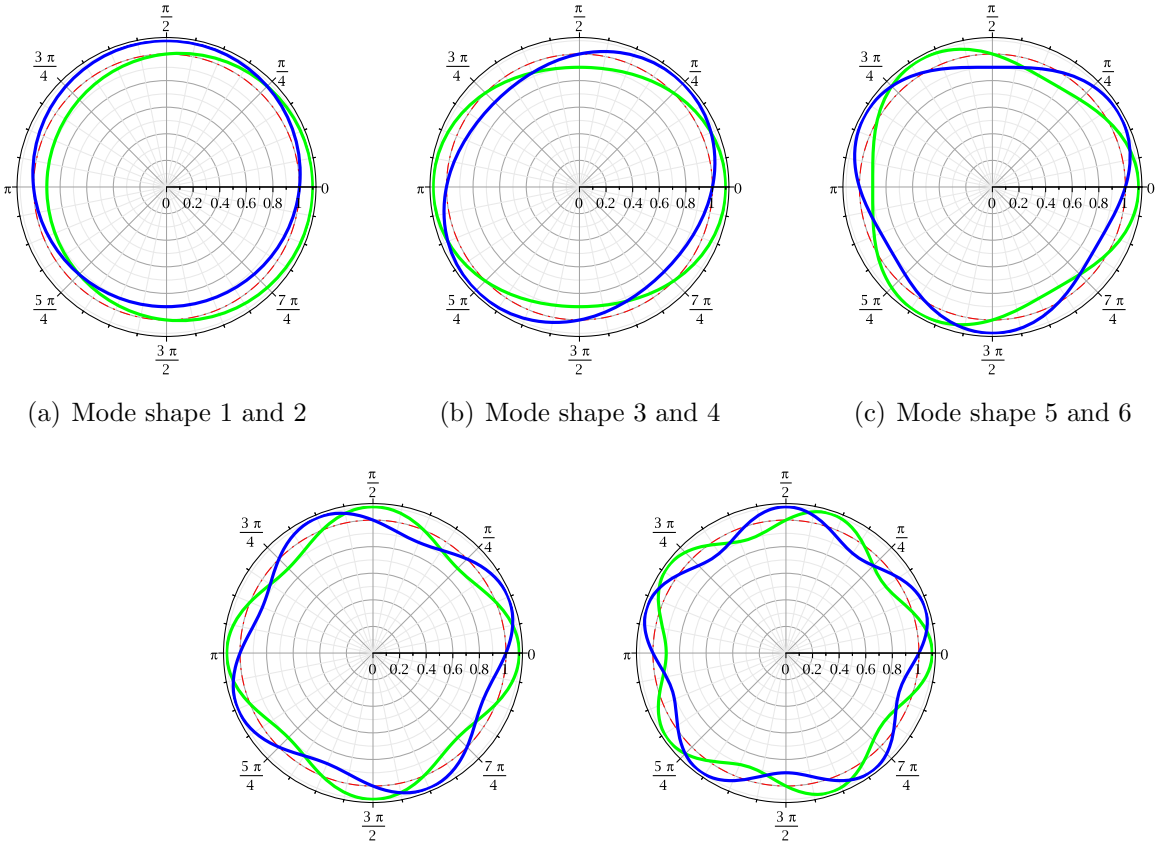

(a) Mode shape 1 and 2 (b) Mode shape 3 and 4 (c) Mode shape 5 and 6

(d) Mode shape 7 and 8 (e) Mode shape 9 and 10

Figure 5.3: Set of considered mode shapes for $k = 1..5$

Substituting Eqn 5.6 into the kinetic and potential energy and considering the Lagrangian $L = T - V$, the equations of motion derived from Lagrange's principle can be written as

$$\frac{d}{dt}\left(\frac{\partial L}{\partial \dot{x}}\right) - \left(\frac{\partial L}{\partial x}\right) = Q_x \tag{5.7}$$

$$\frac{d}{dt}\left(\frac{\partial L}{\partial \dot{y}}\right) - \left(\frac{\partial L}{\partial y}\right) = Q_y \tag{5.8}$$

$$\frac{d}{dt}\left(\frac{\partial L}{\partial \dot{x}'}\right) - \left(\frac{\partial L}{\partial x'}\right) = Q_{x'} \tag{5.9}$$

$$\frac{d}{dt}\left(\frac{\partial L}{\partial \dot{y}'}\right) - \left(\frac{\partial L}{\partial y'}\right) = Q_{y'} \tag{5.10}$$

$$\frac{d}{dt}\left(\frac{\partial L}{\partial \dot{\theta}}\right) - \left(\frac{\partial L}{\partial \theta}\right) = Q_{\theta} \tag{5.11}$$

$$\frac{d}{dt}\left(\frac{\partial L}{\partial \dot{a}_k}\right) - \left(\frac{\partial L}{\partial a_k}\right) = Q_{ak}, \;\; k = 1, 2, ..., N \tag{5.12}$$

$$\frac{d}{dt}\left(\frac{\partial L}{\partial \dot{b}_k}\right) - \left(\frac{\partial L}{\partial b_k}\right) = Q_{bk}, \;\; k = 1, 2, ..., N \tag{5.13}$$

First of all, the $X - Y$ components of radial $f_n(\psi, t)$ and tangential $f_t(\psi, t)$ forces must be obtained using the following rotation transformation

$$\left\{ \begin{array}{c} F_X(\psi, t) \\ F_Y(\psi, t) \end{array} \right\} = \mathbf{R} \left\{ \begin{array}{c} F_n(\psi, t) \\ F_t(\psi, t) \end{array} \right\} \tag{5.14}$$

The generalized forces Q_x, Q_y, $Q_{x'}$, $Q_{y'}$, Q_θ, Q_{ak}, and Q_{bk} can be obtained from the virtual work

$$\delta W = \int_0^{2\pi} \left[F_X(\psi, t)\, F_Y(\psi, t)\right] \, \delta \mathbf{p} \; d\psi + F_{hX}\delta x + F_{hY}\delta y + T_h \delta\theta \tag{5.15}$$

Using Eqn 5.1, the variations of $\delta\mathbf{p}$ can be related to variations in δx , δy, $\delta x'$, $\delta y'$, $\delta\theta$, δa_k, and δb_k as

$$\begin{aligned} \delta \mathbf{p} = & \left\{ \begin{array}{c} \delta x + \delta x' \\ \delta y + \delta y' \end{array} \right\} + \frac{\partial \mathbf{R}}{\partial \theta} \left\{ \begin{array}{c} [R + w(\psi, t)] \cos\psi \\ [R + w(\psi, t)] \sin\psi \end{array} \right\} \delta\theta \\ & + \mathbf{R} \left\{ \begin{array}{c} \left[\sum_{k=1}^{N} \delta a_k(t) \sin(k\psi) + \delta b_k(t) \cos(k\psi)\right] \cos\psi \\ \left[\sum_{k=1}^{N} \delta a_k(t) \sin(k\psi) + \delta b_k(t) \cos(k\psi)\right] \sin\psi \end{array} \right\} \end{aligned} \tag{5.16}$$

Substituting Eqn. 5.16 into Eqn. 5.15, the expression for the virtual work becomes

$$\delta W = Q_x \delta x + Q_y \delta y + Q'_x \delta x' + Q'_y \delta y' + Q_\theta \delta\theta + Q_{ak}\delta a_k + Q_{bk}\delta b_k \tag{5.17}$$

where the generalized forces Q_x, Q_y, $Q_{x'}$, $Q_{y'}$, Q_θ, Q_{ak}, and Q_{bk} can be found as

$$Q_x = F_{hX} + \int_0^{2\pi} F_X(\psi,t)d\psi \tag{5.18}$$

$$Q_y = F_{hY} + \int_0^{2\pi} F_Y(\psi,t)d\psi \tag{5.19}$$

$$Q_{x'} = \int_0^{2\pi} F_X(\psi,t)d\psi \tag{5.20}$$

$$Q_{y'} = \int_0^{2\pi} F_Y(\psi,t)d\psi \tag{5.21}$$

$$\begin{aligned} Q_\theta &= T_h - \int_0^{2\pi} F_X(\psi,t)\left[R + w\left(\psi,t\right)\right]\sin\left(\psi+\theta\right)d\psi \\ &+ \int_0^{2\pi} F_Y(\psi,t)\left[R + w\left(\psi,t\right)\right]\cos\left(\psi+\theta\right)d\psi \end{aligned} \tag{5.22}$$

$$\begin{aligned} Q_{ak} &= \int_0^{2\pi} F_X(\psi,t)\ \sin(k\psi)\cos\left(\psi+\theta\right)d\psi \\ &+ \int_0^{2\pi} F_Y(\psi,t)\ \sin(k\psi)\sin\left(\psi+\theta\right)d\psi \end{aligned} \tag{5.23}$$

$$\begin{aligned} Q_{bk} &= \int_0^{2\pi} F_X(\psi,t)\ \cos(k\psi)\cos\left(\psi+\theta\right)d\psi \\ &+ \int_0^{2\pi} F_Y(\psi,t)\ \cos(k\psi)\sin\left(\psi+\theta\right)d\psi \end{aligned} \tag{5.24}$$

5.2.1 Contact modelling

To derive expressions for the distributed forces $f_X(\psi, t)$ and $f_Y(\psi, t)$ due to contact of the wheel with the ground, a Winkler foundation model with hyperelastic springs is chosen to represent the deformation of the soft soil. For simplicity, we assume a flat terrain profile at a constant height $g(X) = h$. Contact between the wheel and the road occurs when the flexible wheel penetrates into the road. Mathematically, the contact condition can be expressed as:

$$\Delta(\psi, t) \geq 0 \tag{5.25}$$

the function $\Delta(\psi, t)$ is obtained as

$$\begin{aligned} \Delta(\psi, t) = h - \; & y + y' + \sin\theta \left[R + w(\psi, t)\right] \cos\psi \\ & + \cos\theta \left[R + w(\psi, t)\right] \sin\psi \end{aligned} \tag{5.26}$$

The normal contact force acts in the Y direction and is given by

$$f_Y(\psi, t) = K_f \Delta(\psi, t)^n (1 + C_f \dot{\Delta}(\psi, t)) H(\Delta(\psi, t)) \tag{5.27}$$

where $H(\Delta(\psi, t))$ is the Heaviside step function and n is the nonlinear foundation exponent. The parameters K_f and C_f are the foundation stiffness and damping factor respectively. This representation of the distributed contact force is equivalent to the hyperelastic soil models discussed in section 2.2.2 assuming that $\Delta(\psi, t)$ and $f_Y(\psi, t)$ represent the sinkage and the normal pressure distribution, respectively. It should be noted that the damping respresented in the classic Hunt-Crossley manner is included to allow the wheel to settle. However, when it reaches a steady state in which the vertical dynamics vanish, the damping does not contribute to the normal contact force.

By replacing the foundation stiffness K_f with an equivalent Bekker sinkage modulus and n with the corresponding sinkage exponent, this type of distributed normal force model is equivalent to a classic Bekker soil model. It should be noted that the foundation model is not limited to the use of Bekker's pressure-sinkage relation but that other soil models can be implemented by simply replacing the distributed force in Eqn 5.27 with the corresponding pressure-sinkage relation. Furthermore, the plastic behaviour of soil is implemented by adding a contact condition that is dependent on the derivative of the Δ-function $\dot{\Delta}(\psi, t)$ which represents the penetration rate. Under compression, the soil behaves as shown in Eqn 5.27; however, in case of relaxation when the penetration rate is negative, the soil behaves in a linear manner up to a certain amount of soil rebound as it was shown for the 3rd version of the rigid wheel presented in section 4.2.3 of the previous chapter. Under the

consideration of all contact conditions, this addition to the foundation model results in the following equations.

For $\Delta(\psi,t) \geq 0$ and $\dot{\Delta}(\psi,t) \geq 0$:

$$f_Y(\psi,t) = k_{Bekker}\Delta(\psi,t)^n(1 + C_f\dot{\Delta}(\psi,t))H(\Delta(\psi,t)) \tag{5.28}$$

For $\Delta(\psi,t) \geq (1-\gamma)\Delta_0(t)$ and $\dot{\Delta}(\psi,t) \leq 0$:

$$f_Y(\psi,t) = k_{Bekker}\frac{\Delta_0(t)^{(n-1)}}{\gamma}\left(\Delta(\psi,t) - (1-\gamma)\,\Delta_0(t)\right)(1 + C_f\dot{\Delta}(\psi,t))H(\Delta(\psi,t)) \tag{5.29}$$

where $\Delta_0(t)$ is the soil compression occurring at the location where the soil transitions from compression into relaxation. For a wheel that has settled to steady state, there is only one transition point at the lowest point of the wheel. Hence, $\Delta_0(t)$ equals the maximum sinkage over the contact patch $\Delta_{max}(t)$.

For the calculation of the tangential contact force generated in the wheel/soil interface, the Janosi-Hanamoto equation (as shown in Eqn 2.7) is assumed and the shear deformation j along the contact patch is calculated by integrating the contact velocity $\Gamma(\psi,t)$ over the circumferential wheel domain. Hence, the distributed tangential force function can be calculated using Eqn 5.30.

$$f_X(\psi,t) = \tau_{max}\left(1 - e^{-\frac{j_x}{K_x}}\right) f_Y(\psi,t)\ \mathrm{sign}(\Gamma(\psi,t)) \tag{5.30}$$

$$\text{with}\quad \tau_{max} = C + f_Y(\psi,t)\tan\phi \tag{5.31}$$

where

$$j_x(\psi,t) = \int_0^{2\pi}\Gamma(\psi,t)\frac{d\psi}{\dot{\theta}} \tag{5.32}$$

$$\Gamma(\psi,t) = \begin{cases} \dot{p}_y(\psi,t) & \text{for } \Delta(\psi,t) \geq 0 \\ 0 & \text{for } \Delta(\psi,t) \leq 0 \end{cases} \tag{5.33}$$

Hence, the function $\Gamma(\psi,t)$ is simply the velocity of the contact patch in the X direction. This concludes the calculation of the contact forces using a hyperelasto-plastic foundation model for the normal forces and the Janosi-Hanamoto equation to calculate the tangential forces due to soil shear. Before the flexible wheel model is simulated and compared against the single wheel test bed results from DLR, the equations of motion are normalized which is shown in the following section.

5.2.2 Model Normalization

To reduce simulation time and prepare the system equations for future parameter studies or possible parameter optimization simulations, the equations of motions are normalized by using a new set of non-dimensional generalized coordinates.

$$\hat{x} = \frac{x}{R},\ \hat{y} = \frac{y}{R},\ \hat{x'} = \frac{x'}{R},\ \hat{y'} = \frac{y'}{R},\ \hat{a_k} = \frac{a_k}{R},\ \text{and } \hat{b_k} = \frac{b_k}{R}.$$

It should be noted that θ remains unscaled. Furthermore, the following non-dimensional parameters are introduced as

$$\hat{M_1} = \frac{MR^2}{\alpha T^{*^2}}, \hat{M_2} = \frac{MR}{\alpha}, \hat{M_3} = \frac{\rho A R^2}{\alpha},\ \hat{J} = \frac{J}{\alpha T^{*^2}}, \hat{K} = \frac{KR^2}{\alpha},\ \text{and } \hat{t} = \frac{t}{T^*}, \tag{5.34}$$

where the normalization parameter α and the time scale T^* are chosen as follows to simplify the energy expression.

$$\alpha = \frac{EI}{R} \text{ and } T^* = \sqrt{\rho A R^3 \alpha} \tag{5.35}$$

Considering the new generalized coordinates and the introduced non-dimensional parameters, the kinetic and potential energies can be written as

$$\hat{T} = \frac{1}{2}\hat{M_1}\dot{\hat{x}}^2 + \frac{1}{2}\hat{M_1}\dot{\hat{y}}^2 + \frac{1}{2}\hat{J}\dot{\theta}^2 + \frac{1}{2}\int_0^{2\pi} \dot{\hat{p}}_X^2 d\psi + \frac{1}{2}\int_0^{2\pi} \dot{\hat{p}}_Y^2 d\psi \tag{5.36}$$

$$\begin{aligned}\hat{V} &= \frac{1}{2}\int_0^{2\pi}\left(\frac{\partial^2 \hat{w}}{\partial \psi^2} + \hat{w}\right)^2 d\psi + \frac{1}{2}\hat{K}\int_0^{2\pi}(\hat{x}' + \hat{w}\cos\psi)^2 + (\hat{y}' + \hat{w}\sin\psi)^2 d\psi \\ &\quad + g\,\hat{M_2}\,\hat{y} + g\,\hat{M_3}\int_0^{2\pi}\hat{p}_Y(\psi, t)d\psi\end{aligned} \tag{5.37}$$

where

$$\hat{w}(\psi, t) = \sum_{k=1}^{N} \hat{a}_k(t)\sin(k\psi) + \hat{b}_k(t)\cos(k\psi),\ \hat{\mathbf{p}} = \frac{1}{R}\mathbf{p},\ \text{and } \dot{\hat{\mathbf{p}}} = \frac{T^*}{R}\dot{\mathbf{p}} \tag{5.38}$$

To formulate the normalized equations of motion using Lagrange's equations, the external wheel hub forces are scaled as

$$\hat{F}_{hX} = \frac{F_{hX}R}{\alpha}, \quad \hat{F}_{hY} = \frac{F_{hY}R}{\alpha}, \quad \text{and} \quad \hat{T}_h = \frac{T_h}{\alpha} \tag{5.39}$$

and the external contact forces applied to the flexible wheel can be normalized by introducing the following non-dimensional stiffness and damping factors of the Winkler foundation model:

$$\hat{K}_r = \frac{K_r R^2}{\alpha}, \quad \hat{C}_r = \frac{C_r R}{T^*} \tag{5.40}$$

where the penetration $\Delta(\psi, t)$ and the relative contact velocities $\dot{\Delta}(\psi, t)$ and $\Gamma(\psi, t)$ are scaled according to the non-dimensional location $\hat{\mathbf{p}}$ and velocity vector $\dot{\hat{\mathbf{p}}}$ of point P shown in Eqn. 5.38. The equations of motion can now be derived by applying the same method of Lagrange's equations as previously used for the unscaled planetary rover tire model. To verify this normalization procedure, a comparison between the scaled and the unscaled set of equations of motion is provided in Appendix B.

This procedure results in a set of nondimensional equations of motion which can be used for more effectively for possible parameter identification or sensitivity studies. Furthermore, the dimesionless system allows for faster simulation times (Petersen et al. 2011). However, to fully use to the advantage of a volumetric modelling approach, the closed-form solution of a volumetric contact force as derived in the previous chapters has to be applied. This requires the determination of the deformed tire states beforehand for which a quasi-static approach is proposed and explained in the following section. Both the full set of the equations of motion of the flexible wheel and the reduced set derived from the quasi-static approach are simulated and compared against each other as well as experimental results from a single wheel test bed.

5.3 Quasi-Deformable Volumetric Tire Model

To use the volumetric contact model approach in a flexible planetary rover wheel model, the deformation states of the wheel and the soil have to be determined. For that purpose, the quasi-static solution of the flexible wheel equations is determined assuming that the rigid body motion has settled to a known constant velocity state. Furthermore, it is assumed that the flexible modes are not in motion, which means that the velocities and accelerations of all flexible degrees of freedom are set to zero. Once the deformed geometries have

been determined and the new contact interface has been defined, the penetration volume and its properties required for the proposed hypervolume model can be calculated. From the derivation of the equations of motion as shown in the previous sections, the system equations of the wheel freely rolling on the soft soil yield

$$\mathbf{M}\left(\dot{\mathbf{q}}, \mathbf{q}, t\right) \ddot{\mathbf{q}} = \mathbf{F}\left(\dot{\mathbf{q}}, \mathbf{q}, t\right) \tag{5.41}$$

where $\mathbf{M}\left(\dot{\mathbf{q}}, \mathbf{q}, t\right)$ is the mass matrix and the right hand side $\mathbf{F}\left(\dot{\mathbf{q}}, \mathbf{q}, t\right)$ includes the internal and external forces as well as the contact forces generated in the wheel soil interface. The generalized coordinates can be separated into two subsets, one for the rigid body motion of the wheel hub $\mathbf{q}_r$ and another set for the flexible modes of deformable circular beam $\mathbf{q}_f$. It should be noted that the two coordinates of the frame that capture the relative motion of the ring to the wheel hub are included into the set of flexible modes.

For the quasi-static solution it is assumed that the rover moves slowly enough that the influence of the system interia on the solution can be neglected. Hence, the acceleration terms on the left hand side vanish and the system equations yield

$$\mathbf{F}\left(\dot{\mathbf{q}}_r, \mathbf{q}_r, \dot{\mathbf{q}}_f, \mathbf{q}_f, t\right) \;=\; 0 \tag{5.42}$$

assuming that the rigid states of the wheel hub are known and that the flexible modes have settled to a steady state $\dot{\mathbf{q}}_f = 0$, one can solve the nonlinear system of equations numerically to yield to a quai-static solution.

$$\mathbf{q}_f = f(\dot{\mathbf{q}}_r, \mathbf{q}_r) \tag{5.43}$$

Once a solution is reached, the deformed shape of the wheel is assumed to be the new shape of the wheel and compared against the terrain geometry. For this instant, the updated geometry is assumed to be not deformable which means that the contact problem has be reduced to a rigid wheel in contact with the soft terrain. This allows us to apply the theory and the contact model as derived in the previous chapter. The flexible and the quasi-flexible planetary rover wheel have been simulated and compared against the single wheel tests from DLR.

5.4 Single-Wheel Simulation and Results

For validation purposes, both the flexible and the quasi-flexible wheel model are simulated in a single wheel test. The results are compared against experimental data from a single

wheel testbed (Scharringhausen et al. 2009a). For these experiments, a flexible wheel (radius $R = 125mm$, width $b = 100mm$) with a vertical wheel load of $70N$ was translated at a velocity of $v_x = 10mm/s$ through fine and dry quartz sand. Numerous measurements were taken by prescribing the angular velocity of the tested wheel in order to create wheel slip varying from 5% to 95%. For the experiment, the longitudinal slip of the flexible wheel is defined as

$$s_{long} = 1 - \frac{v_x}{R_l \, \omega_y} \tag{5.44}$$

where R_l is the loaded radius of the wheel and is defined as the distance between the wheel hub and the location of point $\mathbf{p}$ under the wheel in the vertical direction.

The simulation results of the two different flexible wheel models are presented in a drawbar pull plot and directly compared against the experimental results from DLR. The plot can be seen in Figure 5.4 below.

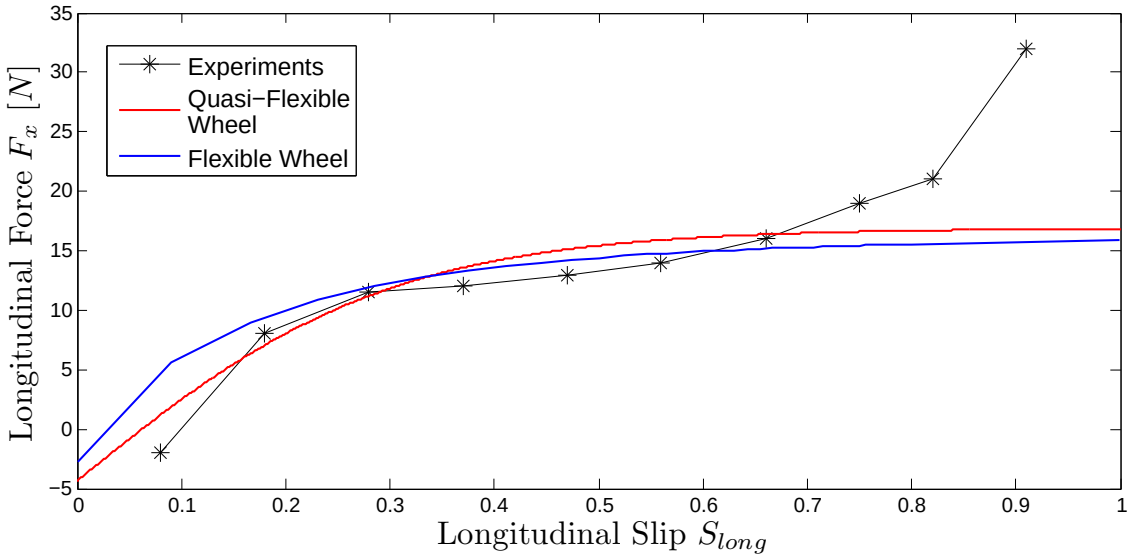

Figure 5.4: Flexible and quasi-flexible volumetric wheel model in comparison with single wheel test results

It can be seen in the plot of the drawbar pull versus longitudinal slip that the flexible and quasi-flexible wheel show a decent match with the experimental results for the most part of the tested longitudinal slip interval. Toward the end of the plot where the longitudinal slip is greater than 75% the models deviate from the experimental results. The

experiments show a large increase of traction force in this slip region. This sudden increase is a phenomenon likely due to the tread geometry of the wheel which is not specifically represented in the tangential soil force model used for the two versions of the flexible planetary rover wheel. The grousers utilized in the single wheel experiments are modelled by assuming an increased effective wheel radius (Wong 2010). Due to this assumption and the simplicity of the curve fit functions of the shear force models in both flexible wheel models (see Eqns 2.7 and 4.30), the drawbar pull force cannot follow the sudden traction increase.

Chapter 6

Planetary Rover Simulation Results

In previous chapters, we defined the theory of the hyperelastic foundation model and how it can be utilized in rigid and flexible planetary rover wheel models including the phenomena of large soil deformation problems. In this chapter, the developed theory and models are tested on a full vehicle model and verified through experimental results. The vehicle used for this purpose is the Juno Rover of the Canadian Space Agency (CSA) and the following sections explain in detail the architecture and design of the Juno Rover. A multibody dynamics model of the rover is created including the developed wheel models. This full vehicle model is used to identify crucial model parameters by comparing simulation results against experimental data obtained from a drawbar pull test. As will be demonstrated in 3D terrain simulations, the developed theory and planetary rover wheel models are validated through irregular terrain experiments.

6.1 Juno Rover

For all of the following simulations and experiments, the Juno Rover of the Canadian Space Agency is considered. A picture of the rover can be seen in Figure 6.1.

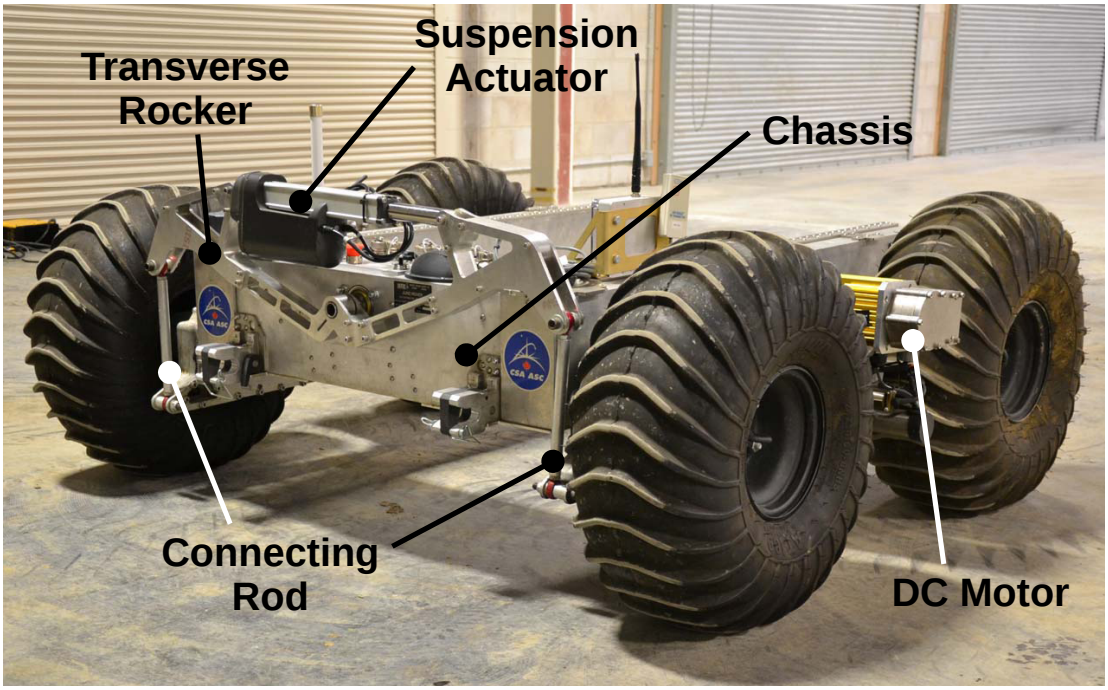

Figure 6.1: Juno Rover

The Juno rover is a skid-steered four wheel vehicle with a dependent walking beam suspension system. The rover is built by Ontario Drive and Gear Ltd. and Neptec Design Group Ltd. as part of a joint development project led by the Canadian Space Agency. The configuration can be seen in the picture of Figure 6.1 as it shows the rear of the rover. Two DC motors drive the rover, one attached to each of the main rockers. The wheels on each side are driven by a 1:1 chain wheel drive that is powered by the motor through a two gear transmission with gear ratios of 1:129 and 1:32 for the lower gear and the higher gear, respectively. This way, each side can be driven individually, whereas the two wheels on each side are constrained to the same angular velocity. The total mass of the rover is 317.7 kg including the 22" wheels, each of which weigh 9.6 kg. The wheels on the Juno prototype are lugged ARGO tires on a steel rim and it should be mentioned that the presented diameter of the wheels includes the dimensions of the tire tread or lugs on the tire.

The rover mechanism can be described as a dependent three rocker suspension. A schematic of the suspension mechanism is shown in Figure 6.2.

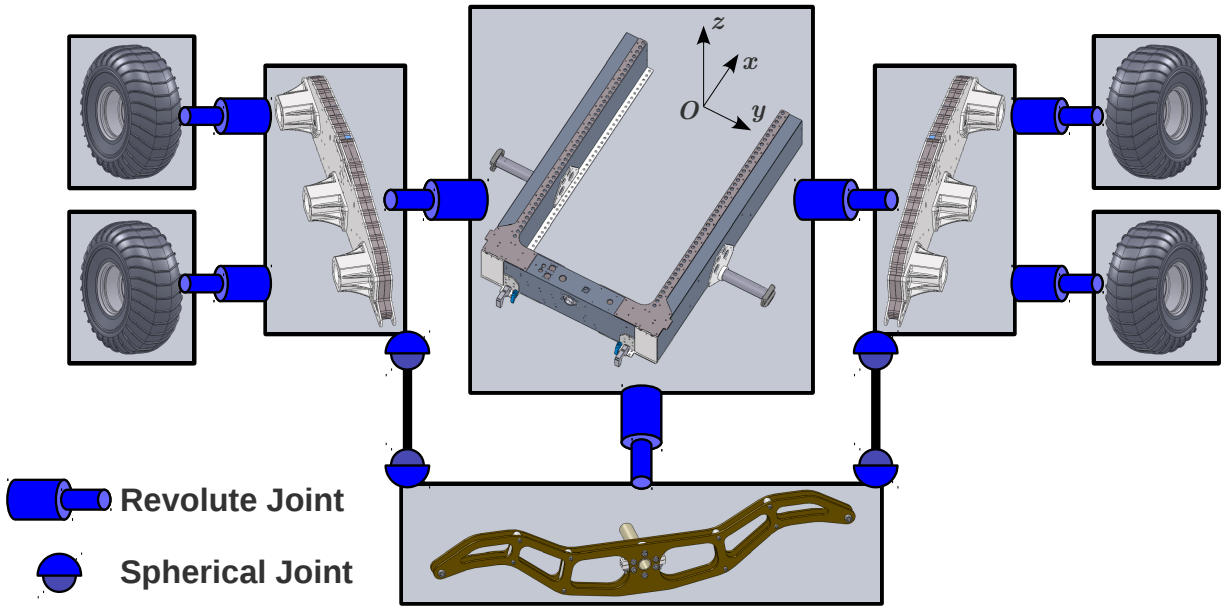

Figure 6.2: Juno Rover Architecture

The two wheels on each side are connected to the main rockers. A transverse rocker attached to the rear end of the rover chassis constrains the movement of the two main rockers through a connecting rod on each side. Through this dependent rocker suspension, the rover load gets evenly distributed from left to right when climbing an obstacle. Additionally, the rover chassis always stays relatively level during such a climbing manoeuvre. In fact, the roll and pitch angle is only half of what the suspension system experiences. Furthermore, with the dependent suspension system, an actuator can be used to adjust the suspension system. This actuator was implemented on the transverse rocker in the most recent prototype of the rover (see Figure 6.1) and it can then be used to tilt the rover chassis to gain further advantages for climbing possible rock obstacles. The overall dimensions are approximately $1.4m$ in longitudinal x-direction, $1.5m$ in lateral y-direction, and $0.6m$ in vertical z-direction, where the effective track width and wheel base are approximately $1.2m$ and $0.85m$, respectively.

6.1.1 Experiments with Juno Rover

Two experiments with the rover on a compliant terrain were performed to identify parameters and validate the developed planetary rover wheel models in a two step verification

process. Firstly, a drawbar pull test which shows the traction capabilities of the rover was performed. The results from this experiment are used to identify the wheel/soil contact model parameters; all other parameters (e.g. mass and dimensions) were measured directly. Secondly, the rover was driven over an irregular terrain and the results of this experiment are compared against simulations of the rover on a 3-dimensional terrain to validate the wheel models and the identified model parameters.

For this two step validation process, data from different sensors and measuring equipment was collected. The rover itself is equipped with a number of sensors and measuring devices. In addition, a total station was used to track the global rover position via a prism that is attached to the rover. The recorded measurements for the presented experiments also include the positions of the motor encoders, the current drawn by the motors, and the data from an inertial measurement unit (IMU). Furthermore, for the drawbar pull test and the irregular terrain experiment, a load cell was used to measure the drawbar pull and a LIDAR scanner was used to scan the 3-dimensional terrain surface. The load cell was attached to the rear of the rover to record the applied resistive force, whereas the LIDAR scanner was used to scan the surface before and after each experiment. The experimental procedure and the results for the drawbar pull test and the irregular terrain experiment are discussed in detail in sections 6.2.1 and 6.3.1, respectively.

6.1.2 Multibody Dynamics Model

For the simulation of the two previously explained experiments, a multibody dynamics model of the full vehicle is developed. The equations of motions for the Juno rover are derived based on a graph-theoretical modelling approach using the simulation toolbox MapleSim.

As it can be observed from the architecture shown in Figure 6.2, the multibody system (MBS) consists of ten rigid bodies (including the rods connecting the transverse rocker with the walking beams), seven revolute joints, and four spherical joints. This results in a model with 13 degrees of freedom (DOFs). It should be noted that there are two uncontrolled DOFs allowing the connecting rods to spin freely around their axial direction. However, no further constraining of these DOFs is necessary as no numerical problem has been observed due to these DOFs. The model is derived with the choice of 25 generalized coordinates and velocity, which requires the definition of twelve algebraic constraint equations. A figure of the developed rover model can be seen in Figure 6.3.

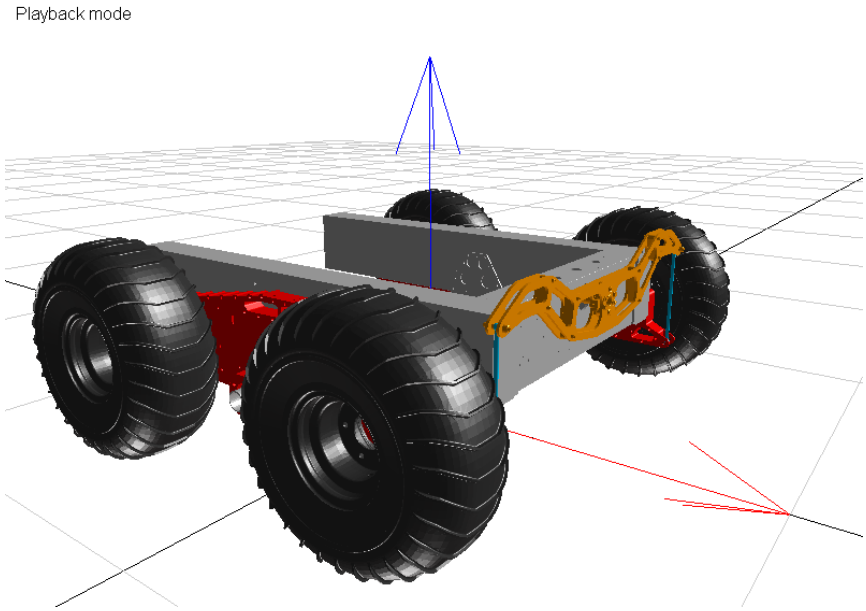

Figure 6.3: Juno rover model as implemented in MapleSim

The developed tire models are included into the equations by applying the tire forces and moments to the coordinates of the corresponding tire bodies. Furthermore, motor torques and the resistive force measured during the drawbar pull test are included as external loads and directly applied to the wheel revolute joints and the rover chassis, respectively.

During the experiments with the Juno rover, only small deformations on the ARGO tires were observed. Therefore, the deformable tire model does not add extra fidelity to this particular application. For the following simulations, the wheel loads applied to the MBS of the rover mechanism are based on the rigid wheel modelling approach as presented in chapter 4.

6.2 Identification of Wheel/Soil Interaction Model Parameters

Besides the inertia and geometry parameters of the wheel, the implemented planetary rover wheel model includes the four soil foundation parameters $\mathbf{a} = [k, \eta, \gamma, K_{v_x}]$. While the inertia and geometry parameters can be easily measured, the listed soil parameters

are difficult to obtain. To tune these parameters, a drawbar pull test is performed and the results are compared against the simulation results of the rover. By minimizing the difference between the experimental and simulation results, an unconstrained optimization procedure is used to approach a set of realistic model parameters. It was observed during the drawbar pull test that the terrain properties varied significantly over the prepared track; however, for simplicity, a homogeneous soil with averaged soil parameters was identified.

The drawbar pull force and the wheel drive torques are measured and applied as simulation inputs to the vehicle model, where matching the forward velocity and the wheel spin measurements define the optimization objective. The results of these measurements are included in a basic optimization routine and the missing parameters are identified through an iterative process by minimizing the residual of kinematic errors. For this purpose, the following cost function $\Omega(\mathbf{a})$ is defined. It consists of the sum of the weighted squared residuals of longitudinal velocity of the rover and the individual wheel spins assuming that $v_{x,i}$, $\omega_{y,i}$ are known at any measured instant of time t_i from the experiments.

$$\Omega(\mathbf{a}) = \sum_{i=1}^{n_{sim}} w_1\, res_{v_x}(\mathbf{a})^2 + w_2\, res_{\omega_y,right}(\mathbf{a})^2 + w_3\, res_{\omega_y,left}(\mathbf{a})^2 \tag{6.1}$$

$$\text{with} \quad res_{v_x}(\mathbf{a}) = \frac{1}{R}\left(v_{x,i} - v_{x,sim}(t_i)\right) \tag{6.2}$$

$$res_{\omega_y,left}(\mathbf{a}) = \left[\omega_{y,i} - \omega_{y,sim}(t_i)\right]_{left} \tag{6.3}$$

$$res_{\omega_y,right}(\mathbf{a}) = \left[\omega_{y,i} - \omega_{y,sim}(t_i)\right]_{right} \tag{6.4}$$

where $res_{v_x}(\mathbf{a})$, $res_{\omega_y,right}(\mathbf{a})$, and $res_{\omega_y,left}(\mathbf{a})$ are the residuals of the forward velocity, the wheel spins of the right side and the wheel spins of the left side, respectively, and w_1, w_2, and w_3 are the weights to these residuals, respectively. The summation limit n_{sim} is the number of time steps in the simulation performed in each iteration of the optimization. It should be noted that this number may vary from one iteration step to another. The residual res_{v_x} of the forward velocity is divided by the nominal wheel radius R so that the terms in the objective function are of the same units. The presented cost function defines the quadratic performance measure and the resulting least squares problem is solved using an unconstrained nonlinear optimization method based on the Nelder-Mead algorithm. The weights are chosen to eliminate numerical significance based on the numerical difference of the forward velocity and the wheel spin, where the forward velocity and the combined wheel spins from both sides are assumed to be of equal significance.

$$w_1 = \frac{\omega_{y,i}}{\frac{v_{x,i}}{R} + \omega_{y,i}},\ w_2 = \frac{1}{2}\frac{\frac{v_{x,i}}{R}}{\frac{v_{x,i}}{R} + \omega_{y,i}},\ \text{and}\ w_2 = \frac{1}{2}\frac{\frac{v_{x,i}}{R}}{\frac{v_{x,i}}{R} + \omega_{y,i}}$$

It should be noted that the weights are different for each parameter identification procedure depending on the desired forward velocity and wheel spin measured from the corresponding set of experimental results. The following sections explain the procedure and the results of the drawbar pull experiment, and discuss the identified parameters.

6.2.1 Drawbar Pull Experiments

For this particular experiment the rover is operated on flat and uncompacted soft soil. To achieve these conditions, the terrain within the test area was prepared before every run of the drawbar pull test. During each of these runs, the rover is forced to move at a constant speed through an applied force that provides enough resistance to provoke longitudinal slip. The rover is driven at a constant throttle setting and slowed down to a constant speed through a human-controlled resistive force applied to the rear end of the rover chassis. By controlling the applied drag force, the goal was to force the rover to settle at a constant slip condition. The rover may start outside the prepared terrain test area to allow for said settling process. In addition to the measurement equipment of the rover and the total station, a load cell was used to record the applied resistive force during each iteration of the experiment. The following list summarizes the crucial measurements that were taken during this experiment:

- Rover IMU — chassis acceleration (three axis)
- Motor — current measurement (left and right side)
- Motor encoder — angular velocity (left and right side)
- Total station — rover position (through prism attached to rover chassis)
- Load cell — drawbar pull force

In total, three runs with individual data sets are considered and a parameter identification process for each of these data sets is conducted. The results of each drawbar pull test run as well as the corresponding optimization routines are explained in detail in the following sections. The resulting parameter sets are compared with each other.

First Drawbar Pull Experiment

The first drawbar pull test was performed over a period of approximately $22s$ on an even and flat terrain. Due to difficulties in controlling the forward velocity of the rover to a

constant speed with the applied force, the results of a period of $10s$ (starting at $8s$) were used, during which the rover had reached nearly steady-state conditions. Furthermore, due to the assumption of constant soil parameters, the average values of each measurement over this $10s$ period were taken and applied to the optimization routine. Figure 6.4 shows the measured drawbar pull force and drive torque that define the simulation inputs to the rover model.

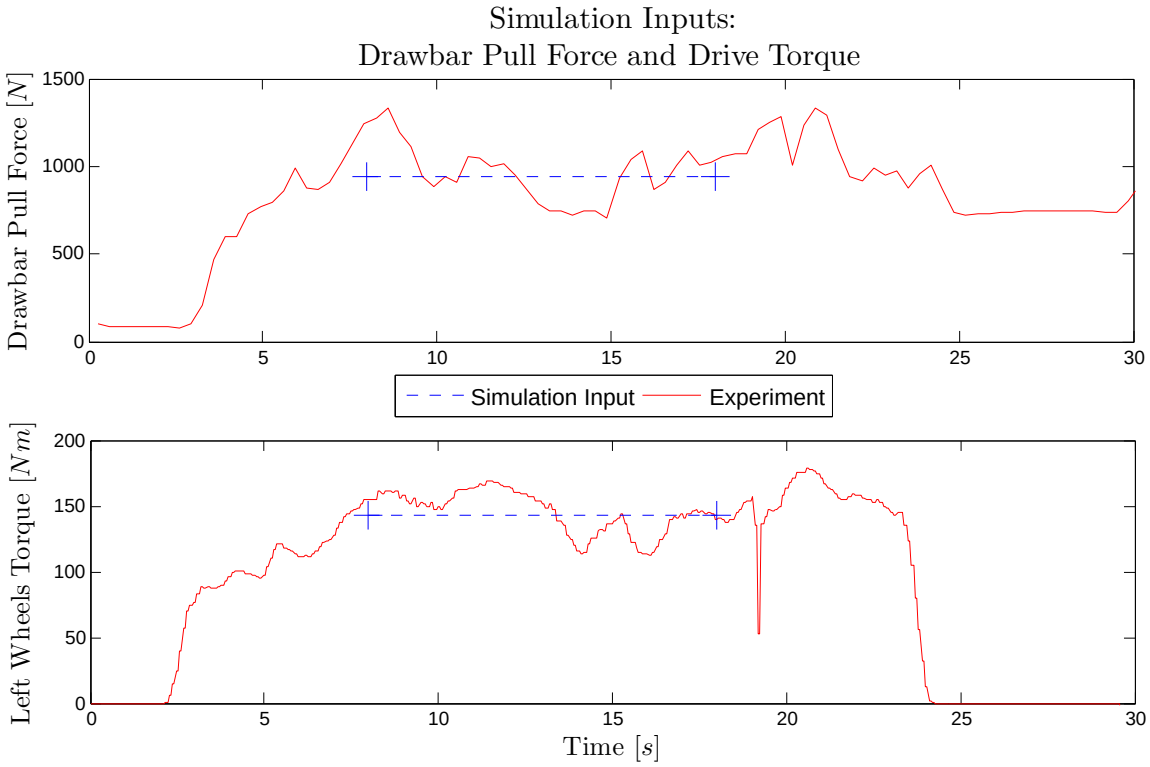

Figure 6.4: Optimization inputs from experimental data of the 1st drawbar pull test

The plots show the recorded drawbar pull force and the measured drive torque as well as the averaged values that are applied to the vehicle model. Considering these simulation inputs, the goal of the optimization is to reach the measured wheel spin and forward velocity of the rover by changing the parameters **a**. Figure 6.5 shows the measured longitudinal velocity and wheel spin that define the optimization objectives.

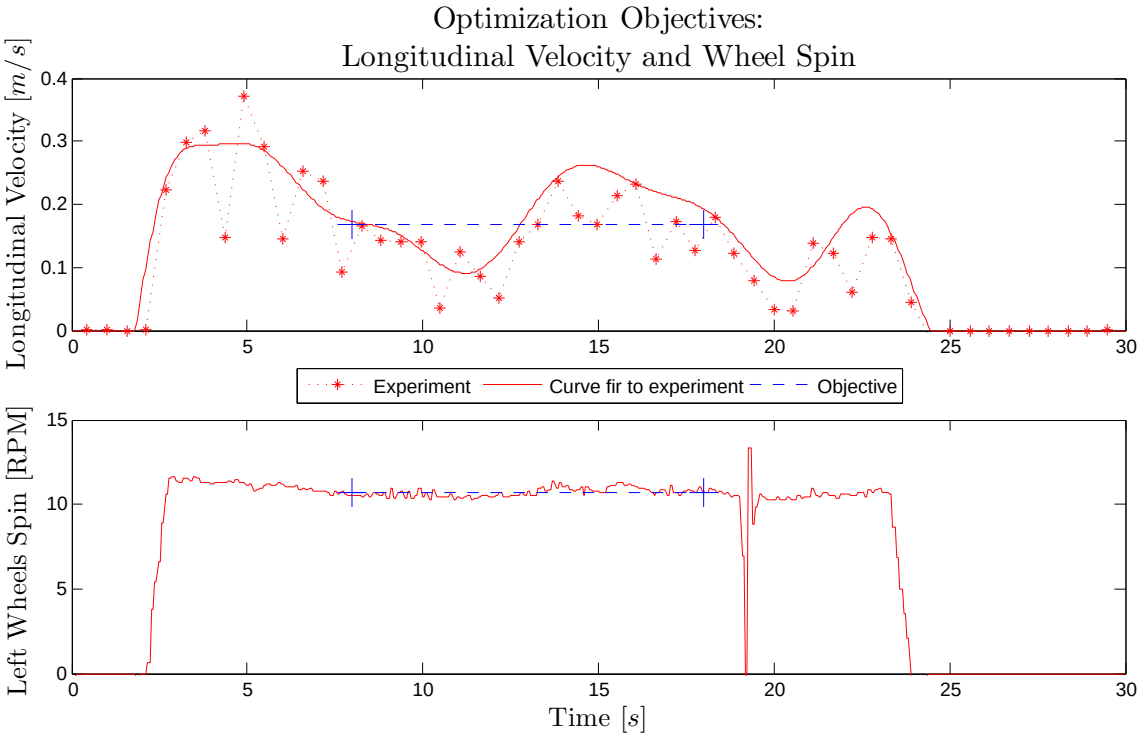

Figure 6.5: Optimization objectives from experimental data of the 1st drawbar pull test

The plots show the longitudinal velocity determined from the total station measurements and the wheel spin determined from the motor encoder recordings as well as the averaged values that are considered during the optimization routine. This concludes the required experimental data to identify the missing parameters using the cost function shown in Eqn 6.1. Table 6.1 shows the initial and final values of the soil parameters **a** for the first drawbar pull test.

Table 6.1: Wheel and soil model parameters for 1st drawbar pull experiment

Model Parameter	Initial Value	Final Value
Foundation Stiffness k $[N/m^{2+\eta}]$	$2.5E10^5$	$2.07E0^5$
Nonlinearity Exponent η	0.5	0.583
Foundation Rebound γ [%]	0.15	0.0674
Traction Modulus K_{v_x}	0.5	0.689

The initial parameters were chosen based on the weight of the rover and an estimation of the required traction force. The results of the final simulation using the found soil parameters can be seen in Figure 6.6.

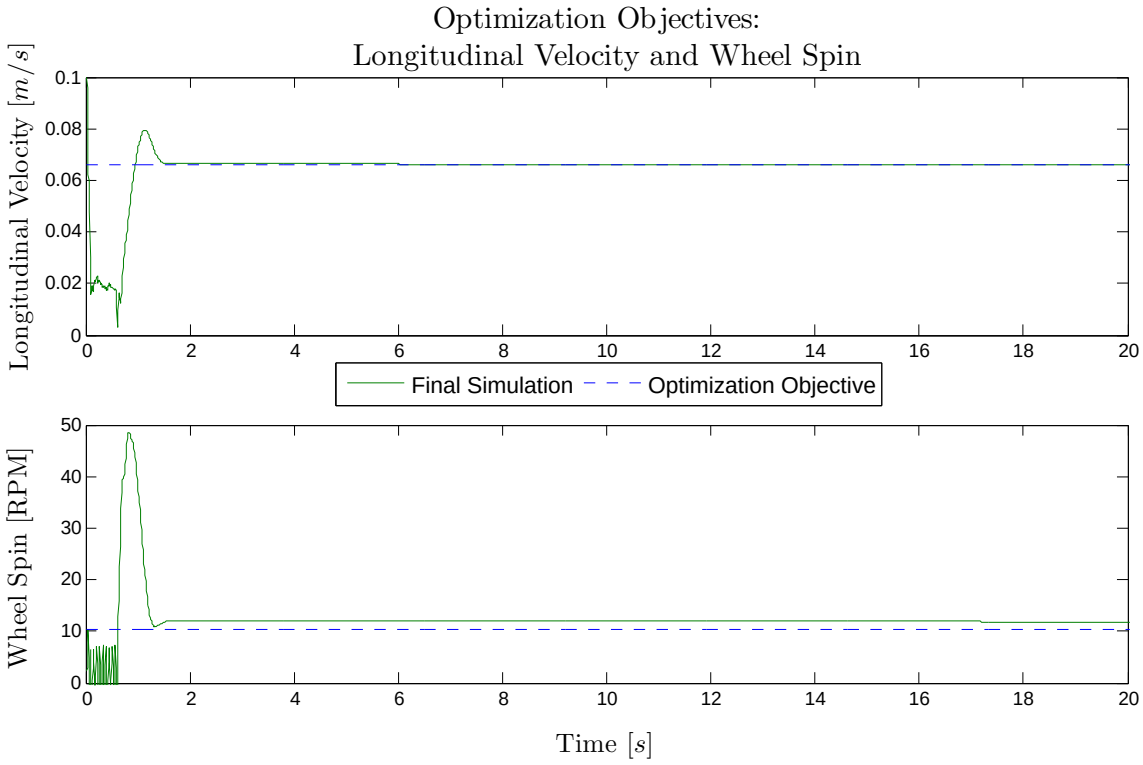

Figure 6.6: Simulation results using found parameters

After a settling phase of $10s$ that is implemented to damp out the vertical motion and to initialize the longitudinal velocity, the rover is driven by the measured wheel torque in a forward dynamic simulation by constantly applying the experimentally determined drawbar pull. Using the final parameter values, it can be observed in the plots of Figure 6.6 that the forward velocity is matched accurately whereas the wheel spin of the model reaches a slightly higher value than the desired one. The difference between the actual and the desired wheel spin is plausible as the implemented traction model is very insensitive to changes in longitudinal slip at the measured slip conditions that the optimization routine is attempting to reach. Hence, the found parameters are acceptable. Once these parameters have been confirmed by the other drawbar pull experiments, they can tested in a forward dynamic simulation of the rover on a 3-dimensional terrain.

Second Drawbar Pull Experiment

The second run of the drawbar pull test was performed over a period of approximately $35s$. Figure 6.7 shows the measured drawbar pull force and drive torque that define the simulation inputs to the rover model.

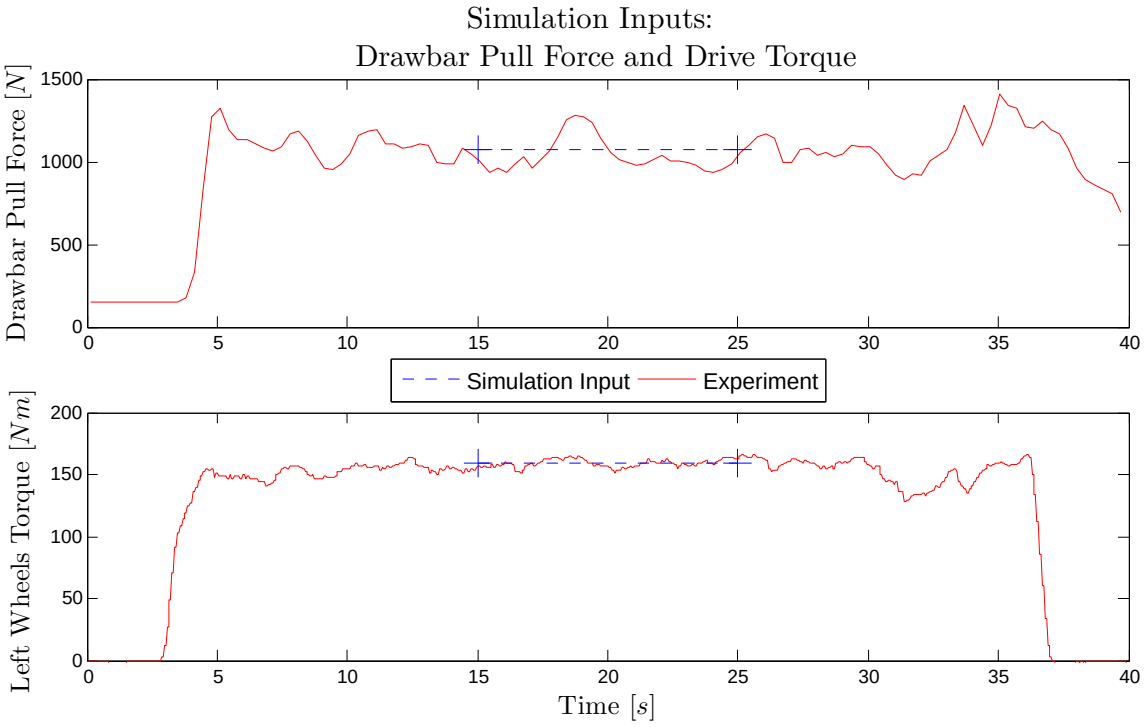

Figure 6.7: Optimization inputs from experimental data of the 2nd drawbar pull test

Figure 6.8 shows the measured longitudinal velocity and wheel spin that define the optimization objectives. In this iteration, the rover seems to be moving steadily over a time period of approximately $10s$ (starting at $15s$). Hence, the average values of the measurements over this time period are considered for the simulation and the optimization procedure.

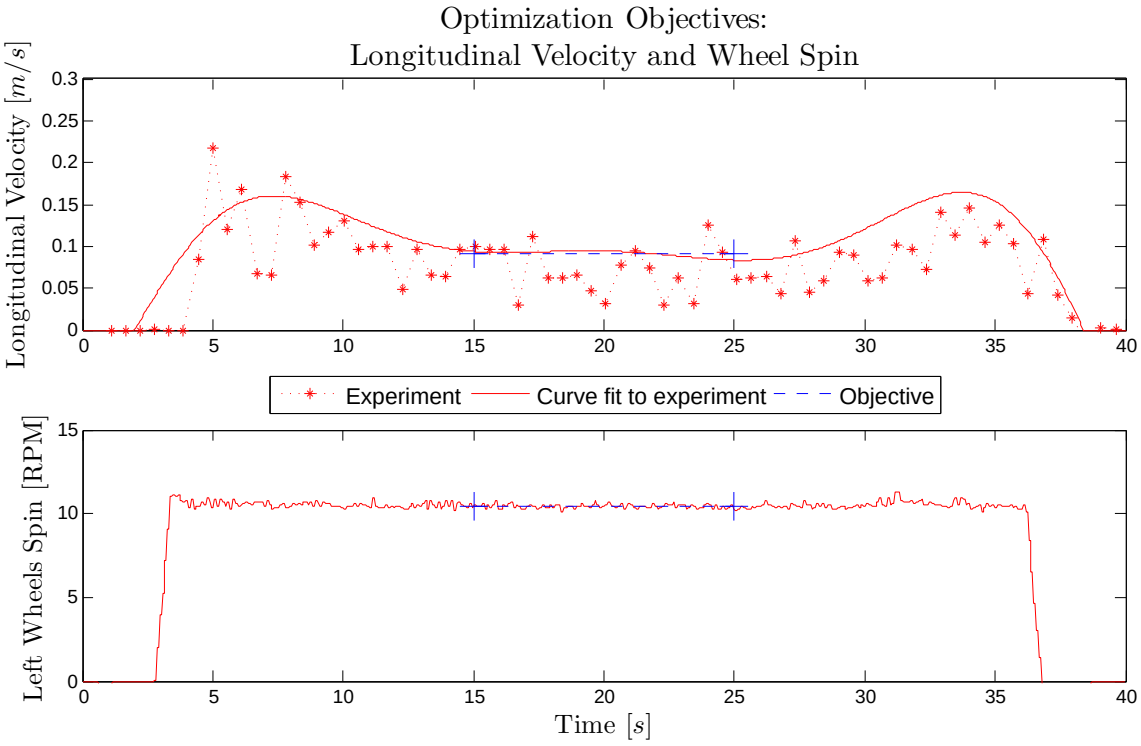

Figure 6.8: Optimization objectives from experimental data of the 2nd drawbar pull test

Using the same initial parameters as in the previous experiment and the averaged values for the simulation inputs and optimization objectives shown in Figure 6.7 and 6.8 respectively, this parameters identification routine settled to the values that can be observed in Table 6.2.

Table 6.2: Wheel and soil model parameters for 2nd drawbar pull experiment

Model Parameter	Initial Value	Final Value
Foundation Stiffness k $[N/m^{2+\eta}]$	$2.5E10^5$	$1.58E10^5$
Nonlinearity Exponent η	0.5	0.501
Foundation Rebound γ [%]	0.15	0.0813
Traction Modulus K_{v_x}	0.5	0.819

Third Drawbar Pull Experiment

This third and last run of the drawbar pull test was performed over a period of approximately $32s$. The measured drawbar pull force and drive torque of this experiment that are applied to the rover model can the seen in Figure 6.9.

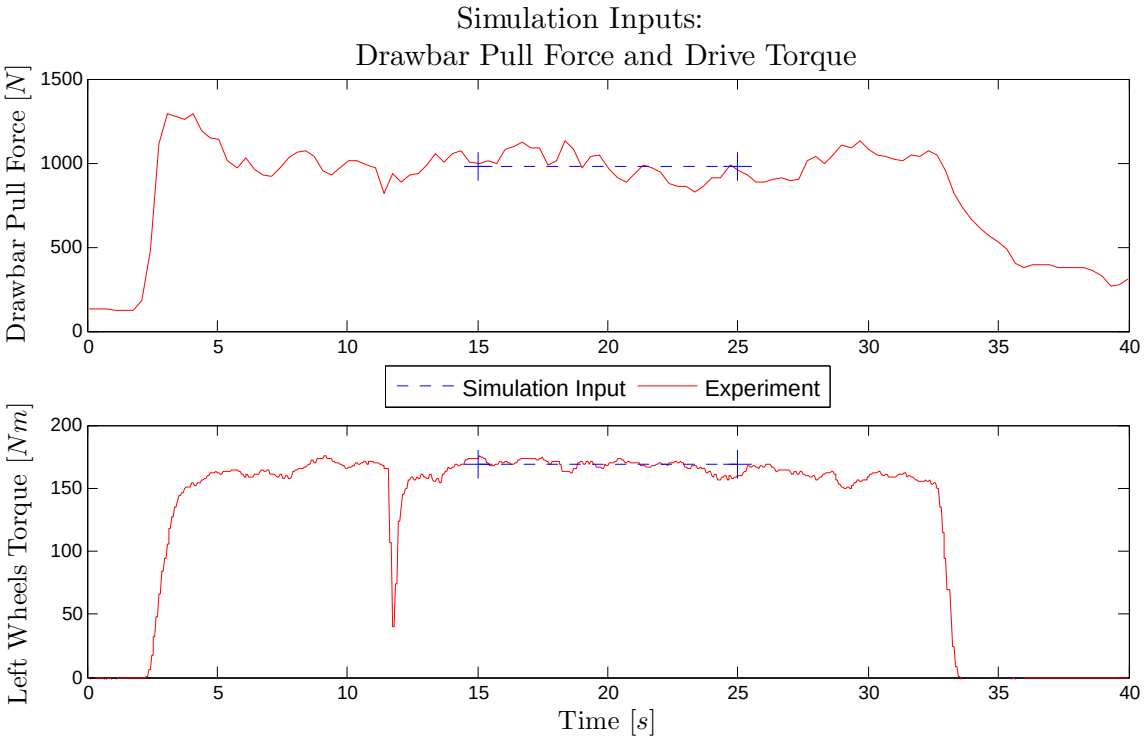

Figure 6.9: Optimization inputs from experimental data of the 3rd drawbar pull test

The measured longitudinal velocity and wheel spin that define the optimization objectives are illustrated in Figure 6.10. For this experiment, the time period of $10s$ (starting at $15s$) is considered to determine the average values of the simulation inputs and the optimization objectives.

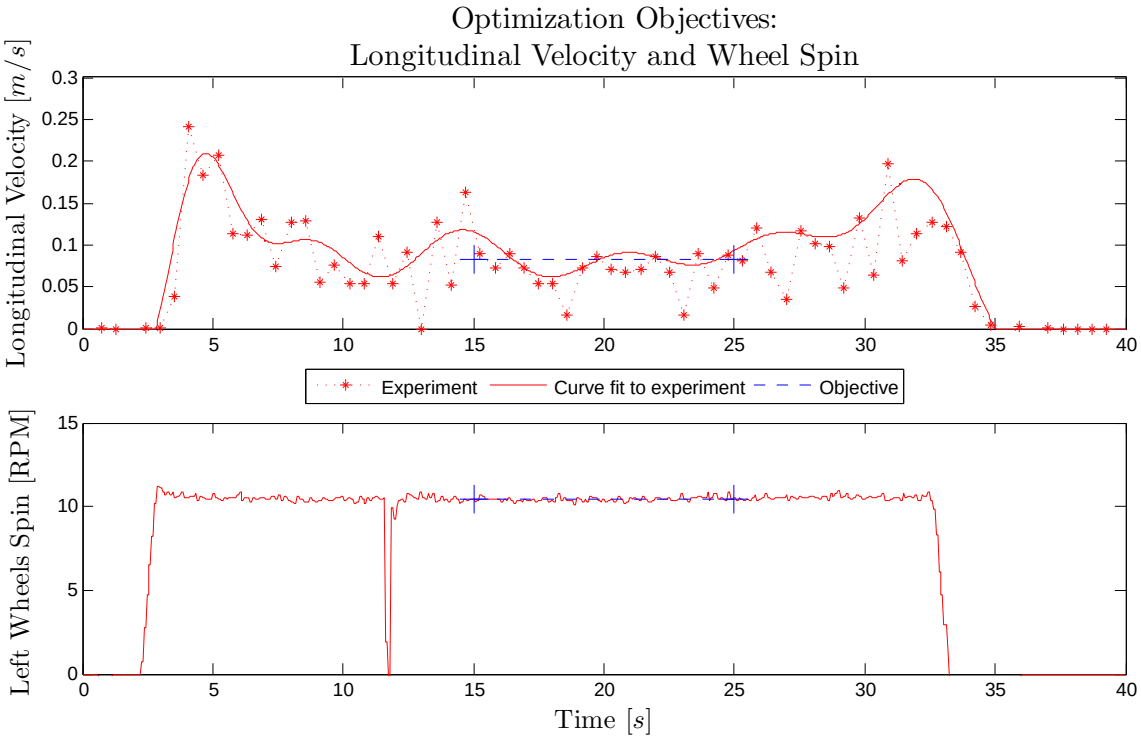

Figure 6.10: Optimization objectives from experimental data of the 3rd drawbar pull test

Again, the optimization routine is initialized with the same values of the model parameters and the unconstrained parameters identification routine reaches the final values listed in Table 6.3.

Table 6.3: Wheel and soil model parameters for 3rd drawbar pull experiment

Model Parameter	Initial Value	Final Value
Foundation Stiffness k $[N/m^{2+\eta}]$	$2.5E10^5$	$1.47E10^5$
Nonlinearity Exponent η	0.5	0.533
Foundation Rebound γ [%]	0.15	0.0834
Traction Modulus K_{v_x}	0.5	0.794

The previous sections have shown that the three different experiments and the corresponding parameter identification routines lead to varying sets of model parameters, albeit

very similar ones. Each of these parameter sets define a slightly different planetary rover wheel model. These models with the individual sets of parameters are then considered to find the best curve fit to the data points taken from the experiments. The traction force ratio of the resulting wheel model is plotted over the longitudinal slip ratio and can be seen in Figure 6.11.

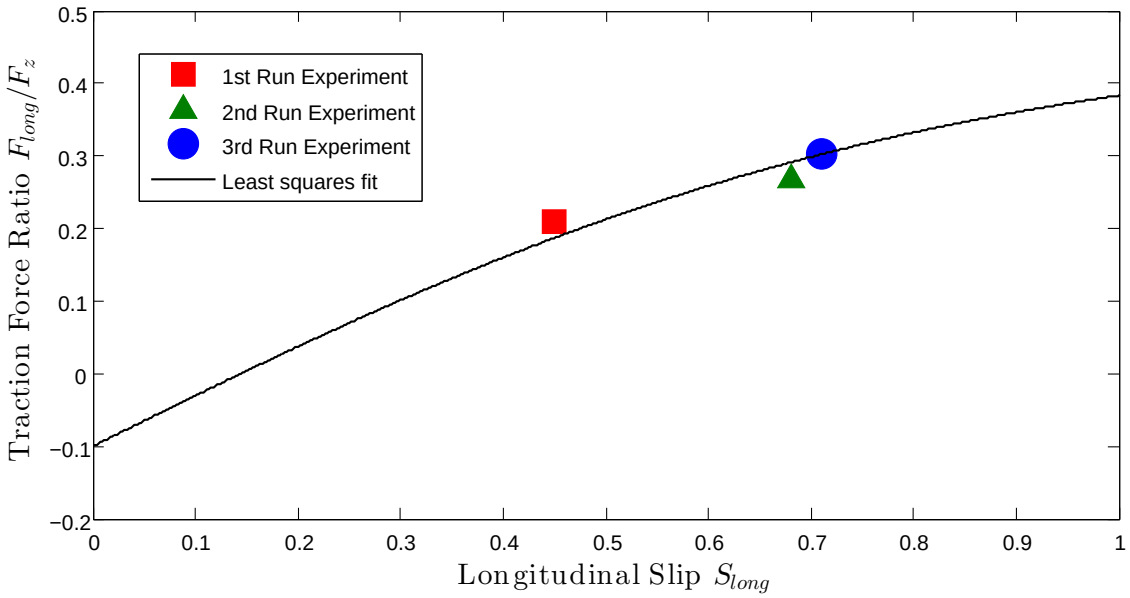

Figure 6.11: Comparison of the identified model parameters

The curve in the plot of Figure 6.11 shows the characteristic behaviour of the developed planetary rover wheel model. To further validate the proposed modelling approach, the tire model with the identified parameters is simulated in a rover manoeuvre on an irregular 3-dimensional terrain and compared against experimental results. For that purpose, the parameters identified using the 2nd data set are used in the following simulations. Due to the fact that the measurements of the kinematic data show the best steady state conditions, this data set is assumed to be the most trustworthy.

6.3 Validation via Dynamic Simulation on 3D Terrain

To verify the parameters and validate the planetary rover wheel model, an experiment is performed in which the rover is commanded to move over uneven terrain. The results of

this experiment are compared against the simulation results from the Juno rover model on a 3-dimensional terrain. The experiment and the comparison of the results with the simulation outcome are discussed in the following section 6.3.1.

To validate the developed volumetric wheel/soil contact model and to verify the found model parameters, a final simulation of the rover on 3-dimensional terrain is performed. For this purpose, the LIDAR scan data from the irregular terrain is added to the MapleSim implementation of the CSA Juno rover model. The terrain data is used as an additional input to the volumetric rover wheel model and a forward dynamics simulation using the found wheel/soil interaction model parameters is run.

6.3.1 Irregular Terrain Experiments

For the 3-dimensional terrain experiment, the rover was operated on irregular uncompacted soft soil. An appropriate area of roughly 20 m^2 was prepared. The experiment was performed by applying a constant throttle setting of 45 % to the DC motors of the rover and by letting the rover drive freely over an irregular terrain including a mound of approximately $0.5m$ in height. During the experiment, the following data sets were recorded: the IMU data of the rover, the left and right side wheel spins, and the motor torques. Moreover, the total station position data of the rover was also recorded. The following list summarizes the crucial measurements that were taken during this experiment and the equipment needed:

- Rover IMU — chassis accelerations and angular rates
- Motor — current measurement (left and right side)
- Motor encoder — angular velocity (left and right side)
- Total station — rover position (through prism attached to rover chassis)
- LIDAR scanner — irregular terrain surface scan

It should be noted that apart from the measurement equipment on the rover and the total station, the terrain was scanned before the vehicle manoeuvring using the LIDAR system. Figure 6.12 shows a plot of the raw scan data that was used for the simulation of this experiment.

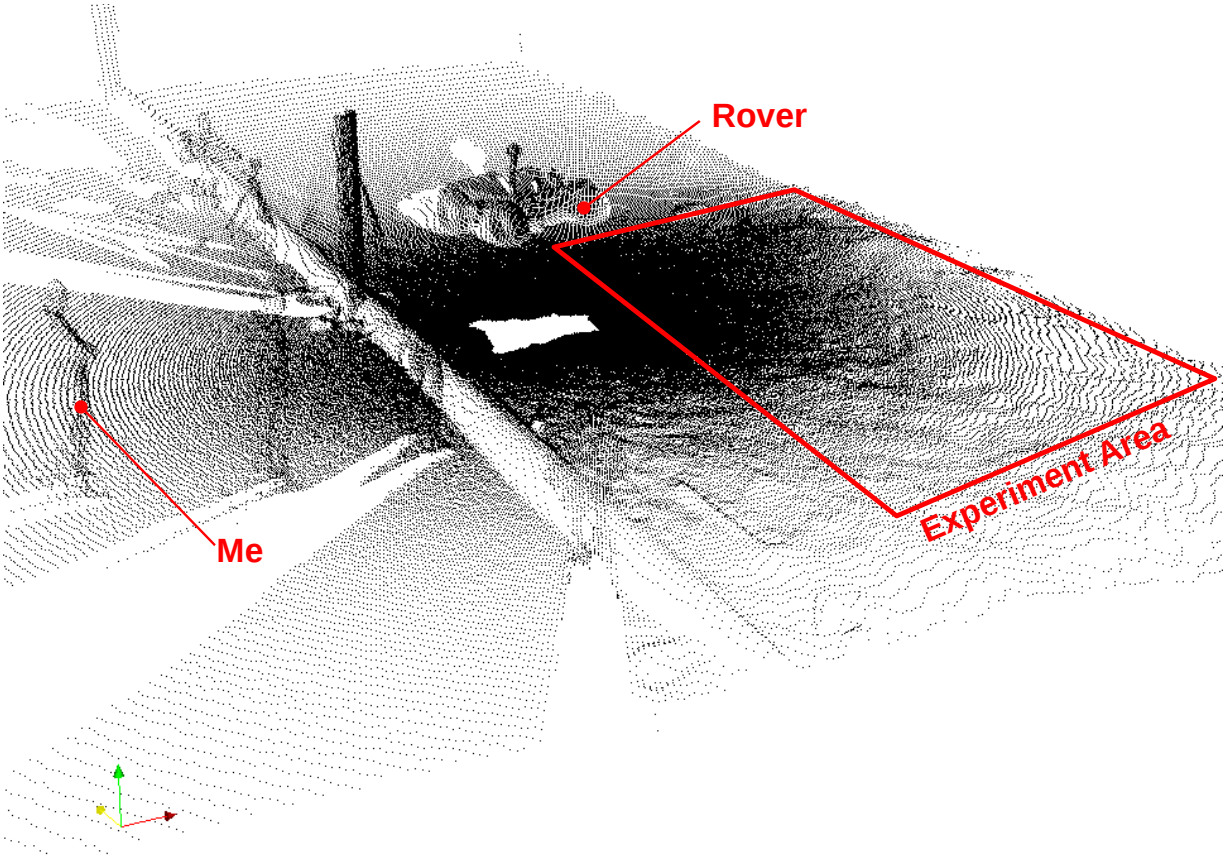

Figure 6.12: Raw LIDAR scan data

The irregularly scattered LIDAR scan data is used to create a numerical representation of the uneven terrain that can be used in the simulation of the Juno rover. Therefore, raw data is cut down and transformed into an elevation function of the horizontal x and y-coordinates. A surface plot of this elevation function representing the 3-dimensional terrain is shown in Figure 6.13.

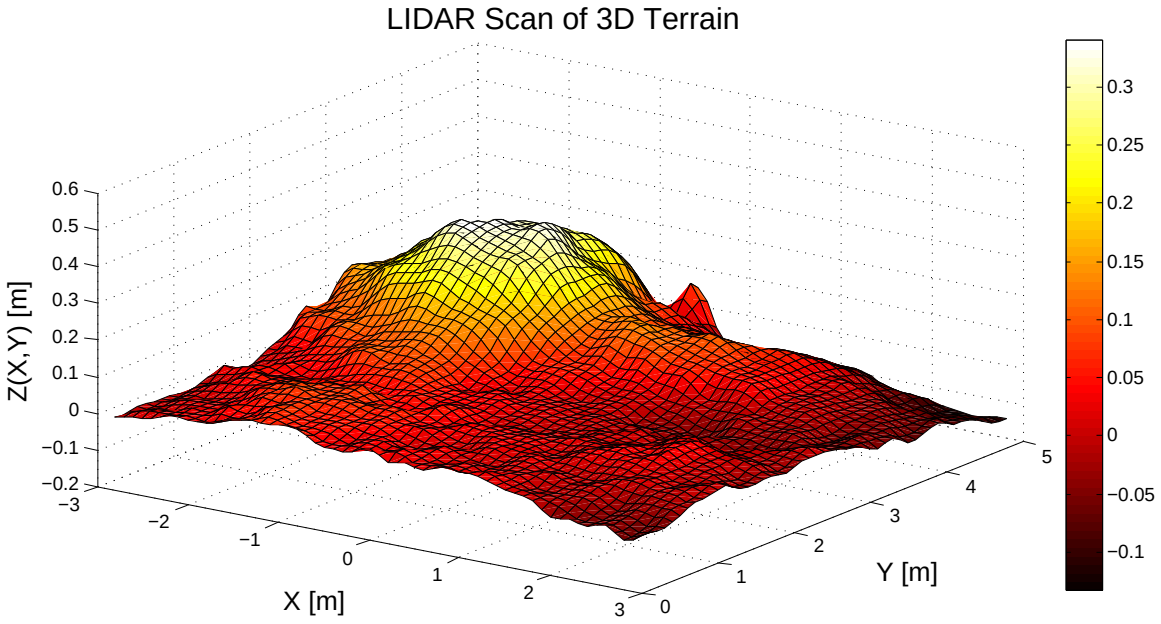

Figure 6.13: Scanned 3D Terrain of Experiment

The presented elevation $z(x, y)$ and the surface normal function $\mathbf{n}_S(x, y)$ that returns a unit vector of the surface normal direction are implemented into the rover wheel model in MapleSim to extend this model with 3-dimensional terrain capabilities. Knowing the surface normal $\mathbf{n}_S$, the tangential directions are determined based on the orientation of the wheel hub frame. With the assumption of a locally flat terrain, the local contact problem is calculated using the hypervolume model as previously explained. All resulting forces and moments are transformed into the wheel hub frame and applied accordingly. To compare the virtual results against the experimentally obtained data, the rover is simulated in a forward dynamics simulation using a simple PID controller on motor torques to force the rover to follow the measured kinematical data. Two different simulations are executed: one controlling the forward velocity of the rover and another one controlling the wheel spin. The following sections discuss the results of these simulations as a final step of this validation process.

3D terrain simulation controlling the wheel spin

It should be noted that the simulated rover has to go through a settling phase. As a result, the virtual rover starts with an initial velocity unlike the actual rover that starts from

rest. This is the reason for the initial difference in the plots. Figures 6.14 to 6.16 show the results of the simulation directly compared against the measurements taken during the 3-dimensional terrain experiment. The results of the longitudinal dynamics can be seen in the position and velocity plot of Figure 6.14.

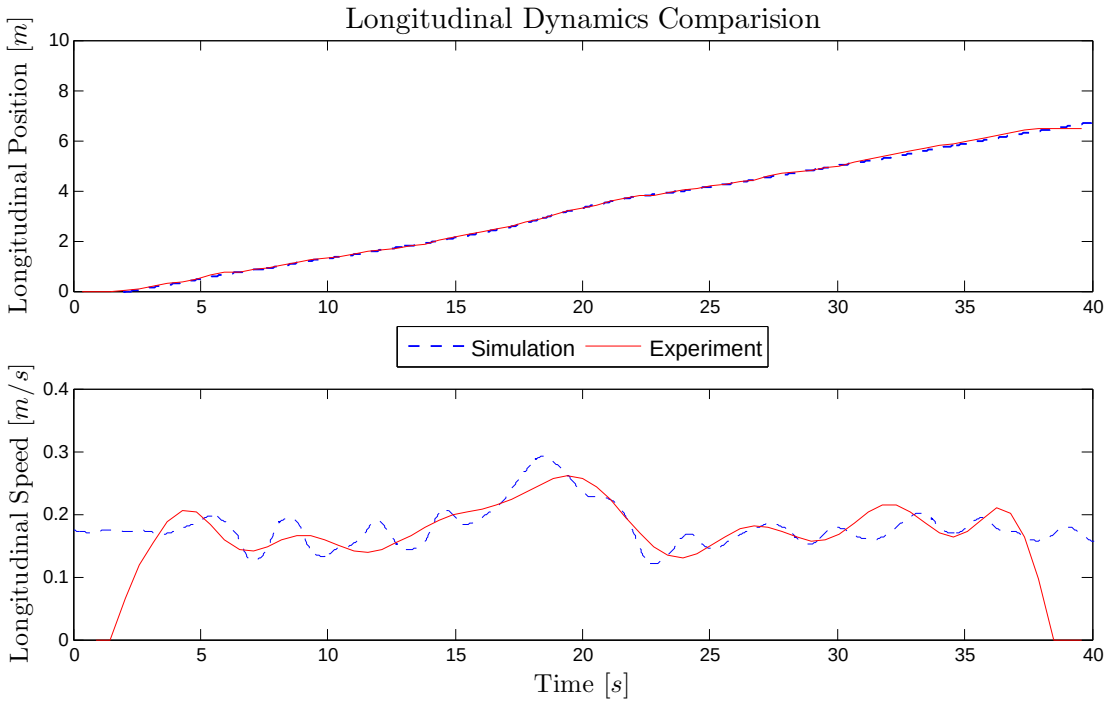

Figure 6.14: Comparison of longitudinal dynamics

The velocity plot shows the performance of the PID controller and it reveals that the forward velocity of the simulated rover fluctuates around the measured longitudinal speed. However, the overall performance appears to be reasonable which can be seen in the position plot of Figure 6.14.

The results of the right and left side wheel spin can be seen in Figure 6.15.

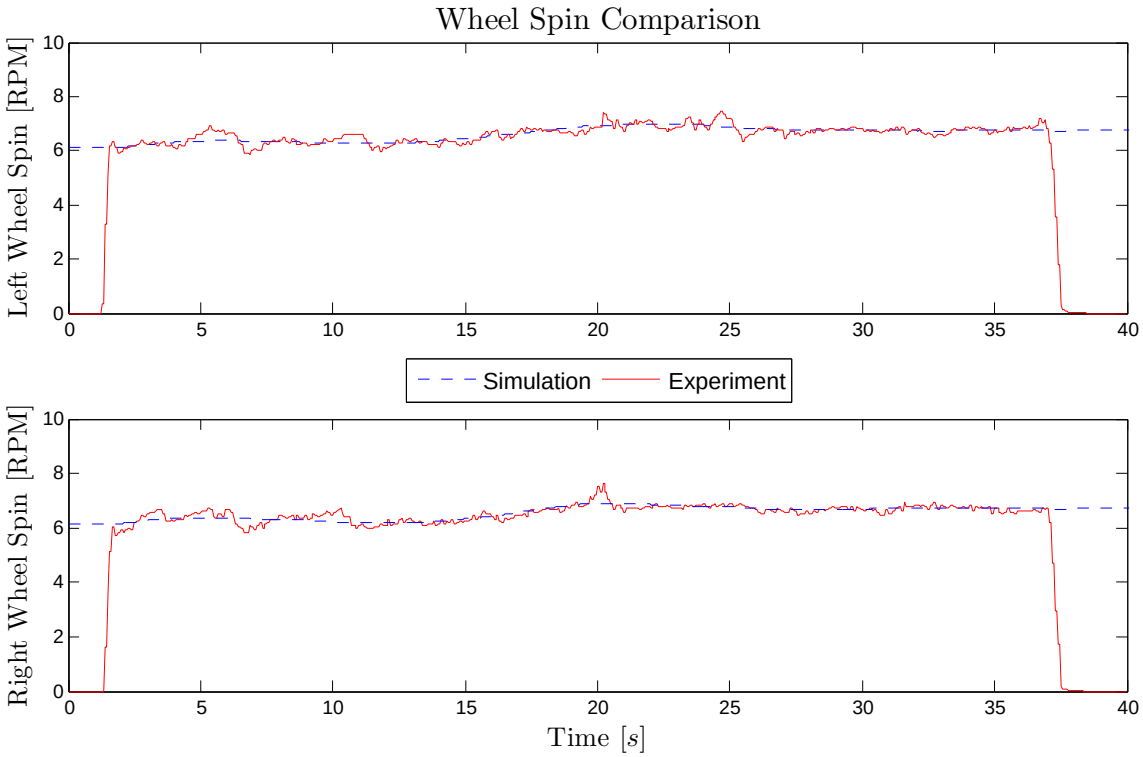

Figure 6.15: Comparison of wheel spin

It can be seen in both plots of Figure 6.15 that the angular spin of the right and left side wheels match the experiments within a reasonable range. This means that the rover undergoes similar slip conditions during the span of the experiment.

Finally, the results of the right and left drive torques as applied to the right and left set of wheels are illustrated in Figure 6.16.

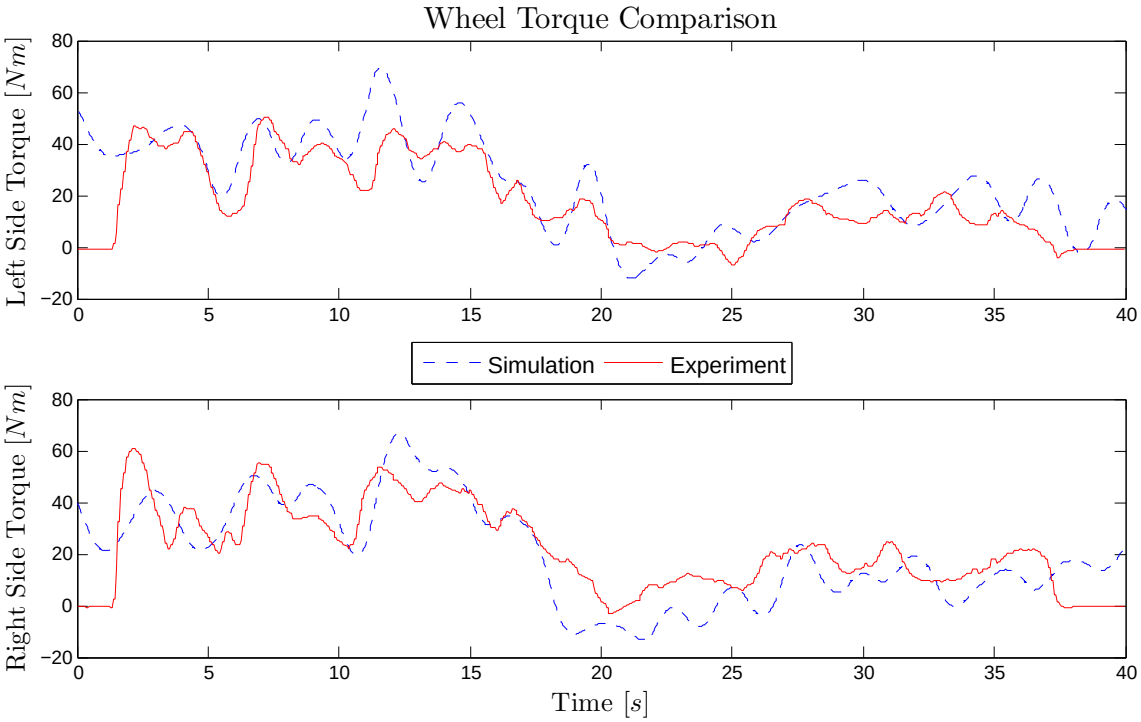

Figure 6.16: Comparison of drive torques

In the plots of the drive torques, the total of the two wheel torques of each side is shown as it was supplied by the DC motors. It can be observed that the torques mostly agree with the experiments. The differences between the measured and the simulated drive torques can be related to a few error sources. The main reason is certainly the fact that the actual soil properties vary over the span of the terrain, whereas the assumption of homogeneous soil properties was utilized in the presented wheel/soil interaction model. Also, due to limited accuracy of the LIDAR system, there are slight differences between the actual and the numerically implemented terrain, which means that especially local bumps in the terrain may not be perfectly aligned with the simulated version. Finally, due to the performance of the PID controller, the torque fluctuates around the desired torque as seen in the longitudinal velocity plot. That being said, both plots in Figure 6.16 show a similar characteristic torque profile, which validates the volumetric planetary rover wheel with the identified soil foundation parameters.

3D terrain simulation controlling the forward velocity

To further match the velocity of the simulated vehicle with the experiments of the rover, a second forward dynamics simulation is run. For this simulation, the forward velocity of the chassis is calculated using the measurements of the prism velocity, the angular rate of the chassis and the orientation (roll, pitch, yaw) of the chassis. The plots of the recorded experimental data used for this calculation can be seen in Figure 6.17.

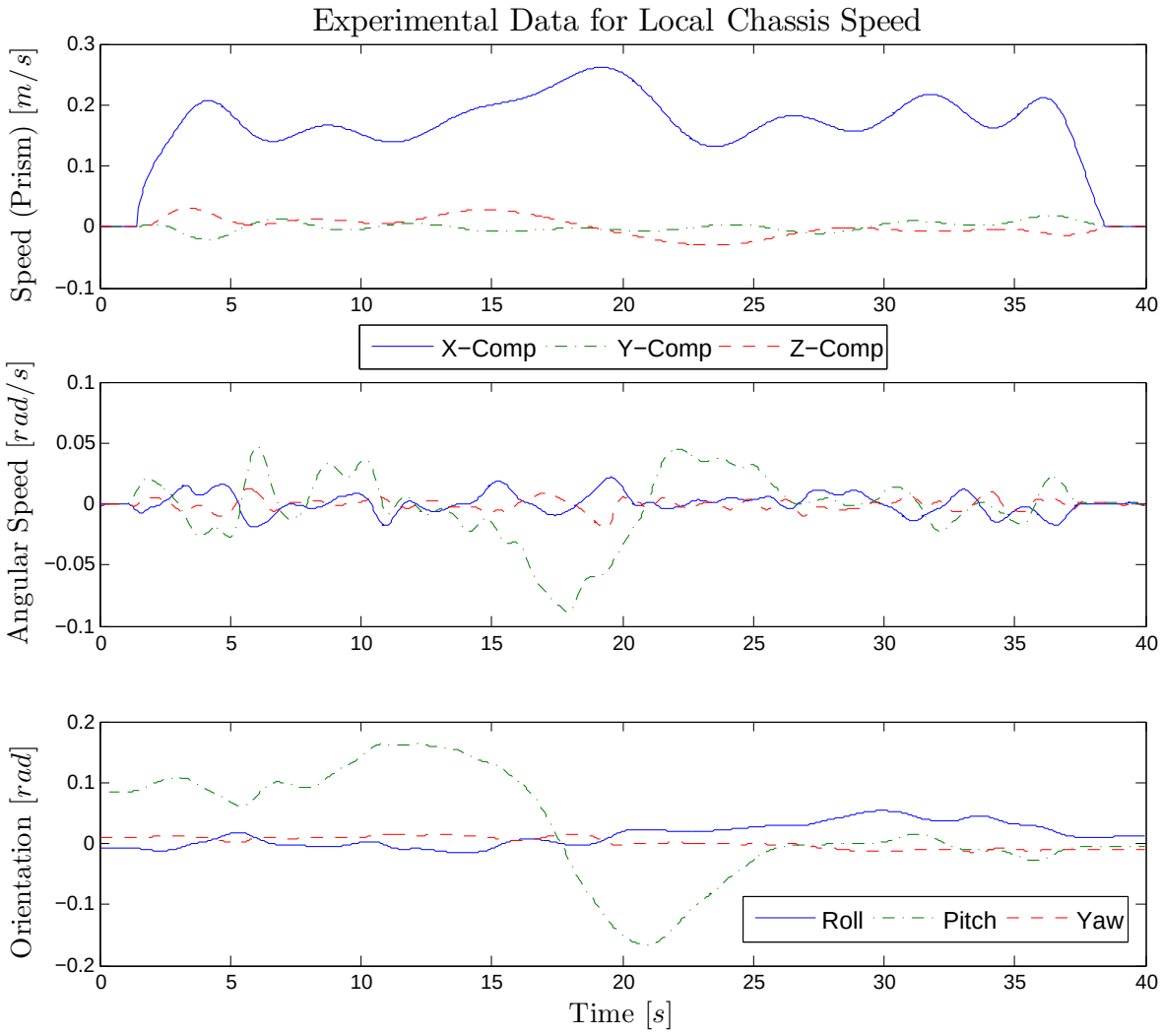

Figure 6.17: Experimental data used to calculate longitudinal speed of chassis

The resulting longitudinal velocity of the rover center of mass that defines the desired velocity of the rover to follow can be seen in the plot of Figure 6.18. Also seen in the plot is the parametrized function of a 10th order polynomial that is used as the actual control input in the simulation.

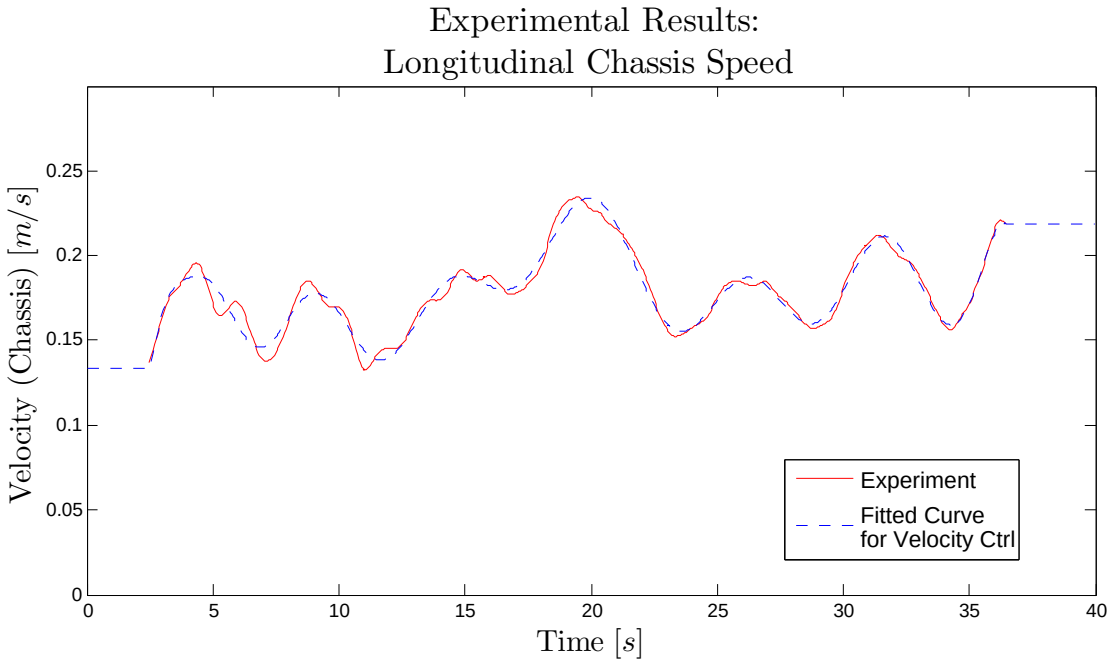

Figure 6.18: Determined longitudinal speed of chassis and fitted curved used in simulation

The results of the simulated longitudinal velocity of rover center of mass and the velocity calculated from the experimental results are illustrated in Figure 6.19. Also shown in this figure is the comparison of the directly measured prism velocity against the simulated value.

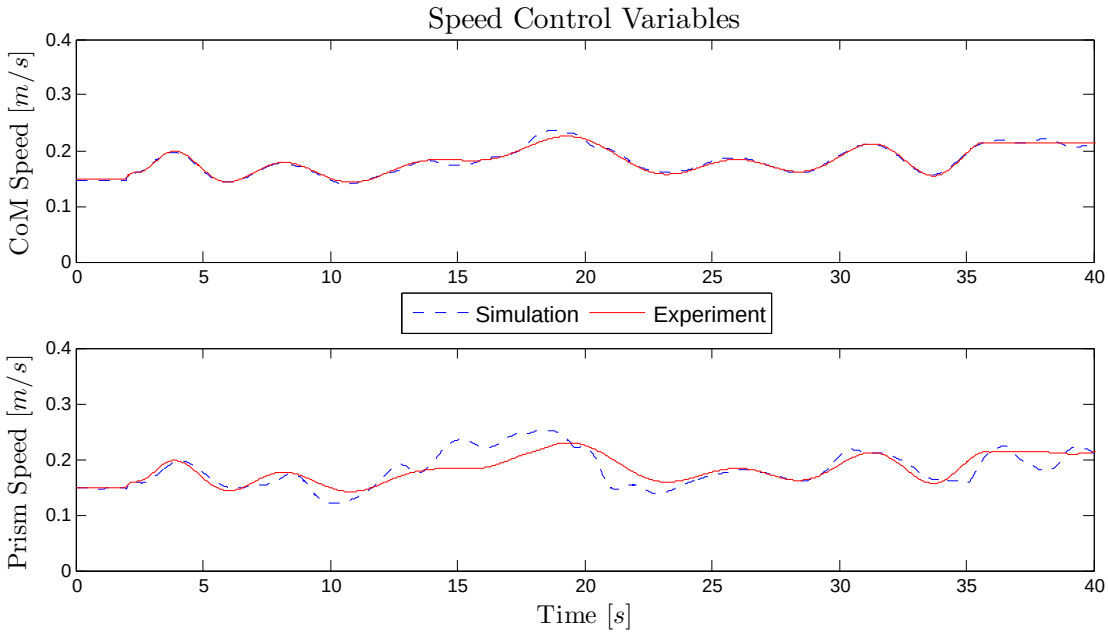

Figure 6.19: Comparison of longitudinal speed of chassis and prism

The plot shows differences in the prism velocity when the rover is at the highest elevation of the 3-dimensional terrain even though the rover tightly follows the desired control velocity prescribed in the simulation. This difference is due to the difference in the actual terrain and the numerically implemented terrain and the resulting difficulty in synchronizing the data with the calculation over the entire simulation time. Similar synchronization issues can be observed in the plot of the drive torques shown in Figure 6.20

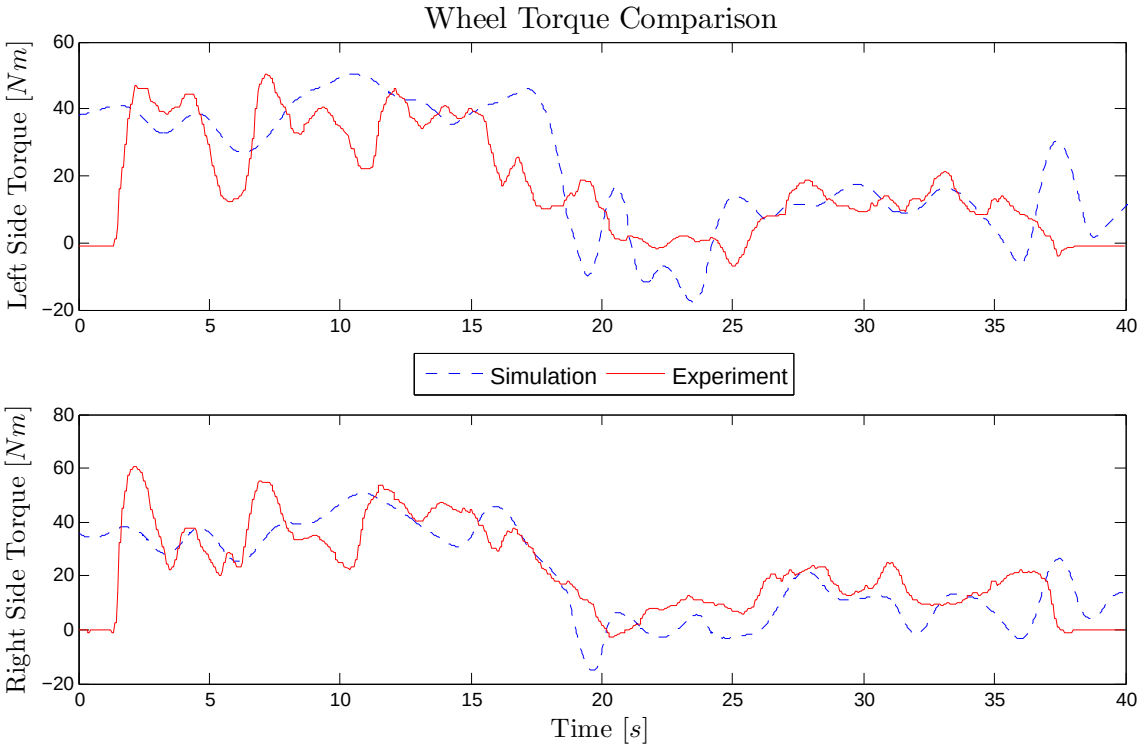

Figure 6.20: Comparison of drive torques

It can be seen in the drive torque plots that the overall value reveals a slightly better match than in the results of the previous simulation in which the wheel spin was controlled. Even if the simulated torque value is quantitatively closer to the actual value, the torque profiles do not follow the actual torque qualitatively as well as the torque profiles of the wheel spin controlled rover. This further confirms slight synchronization errors. However, the two simulations show sufficient evidence to conclude the validity of the developed volumetric planetary rover wheel model including the soil parameters that were identified using the drawbar pull experiments.

Chapter 7

Conclusions

In this project, a volumetric approach is proposed to model planetary rover wheels of many types and shapes moving on soft soil. A nonlinear volumetric contact model is developed with respect to established terramechanics theories. Then it is applied to a rigid and flexible formulation of a planetary rover wheel model. The developed models are verified and validated through full rover experiments on a 3-dimensional irregular terrain.

7.1 Contributions

To predict the forces in the interface of a planetary rover wheel and soft terrain materials, a novel terramechanics contact model based on hypervolumetric properties of the interfering contact geometries is developed. The proposed model is an extension to the linear elastic foundation theory to allow for large deformation and nonlinearities in the soil. In this model, the normal contact force is shown to be proportional to the hypervolume of interpenetration. Due to the fact that the hypervolume centroid is the point of action of the generated contact forces, an expression of the contact normal can be easily found based on the centroid coordinates. Due to the difficulty of analytically solving for the hypervolumetric properties, an exponential model based on a linear curve-fit in logarithmic domain is proposed. This model can be further simplified for known geometries. The two remaining model parameters, which are purely dependent on the geometry of the colliding objects, can then be found through simple numerical experiments. The obtained closed-form solution of the contact force can then be applied in multibody dynamics simulation of planetary rovers to gain a significant computational advantage. Finally, in combination

with numerical methods to solve for the hypervolumetric properties of the contact problem, the model allows for the use of complex contact geometries including lugged tires on irregular soft soil.

This closed-form solution of the nonlinear foundation is used for the development of a rigid wheel/soil interaction model by applying the proposed hypervolume expressions to the geometry of an undeformed planetary rover wheel. It is shown that many pressure-sinkage models from the terramechanics literature can be used in combination with the hypervolumetric contact model to determine the normal tire forces. Inspired by Hanamoto's approach, a volumetric approach based on Mohr-Coulomb failure criterion is used to derive a volumetric expression of the traction force. Classical terramechnics approaches are compared against the volumetric model to show validity of the foundation assumption crucial to the volumetric contact modelling approach. The resulting normal and tangential contact forces are transformed into components of the ISO wheel hub system by calculating the normal direction vector from the hypervolume centroid. This concludes the rigid wheel model which is verified by comparing the predicted wheel forces against experimental results from a single wheel test bed.

To apply the developed theory to a flexible planetary rover wheel, the deformation state of the wheel and the terrain has to be determined. For that purpose, a continuous distributed parameter model is proposed. To capture the deformation of a flexible wheel, a formulation based on Euler-Bernoulli curved beam equations in contact with a hyperelastic foundation is derived. Assuming generalized coordinates according to Lagrange's principle, the equations of motion for the compliant wheel can be derived. Commonly used terramechanics terrain properties are applied to the foundation to allow for a realistic contact force prediction. To validate this distributed parameter model of a flexible rover wheel, the determined contact forces are compared against single wheel experiments. This comparison verified the use of the volumetric approach. The quasi-static solution to the flexible wheel equations is assumed to be the deformed geometry of the wheel which can be directly applied to the hypervolumetric planetary rover wheel formulation derived for a rigid wheel. Once again, this approach is validated through comparison with the experimental results gained from single wheel tests.

The final significant contribution of this work is the experimental validation of the developed hypervolumetric planetary rover wheel model. The developed theories were implemented into MapleSim in a multibody dynamics model of a full vehicle based on the architecture of the Juno rover from the CSA. The validity of the volumetric approach was verified using two separate experiments, the first experiment being a drawbar pull test on even and soft soil. The second experiment is a rover driving manoeuvre on a 3-dimensional irregular terrain. The traction force measurements from the drawbar pull experiment are

used to identify the missing model parameters which are related to the soil foundation. The results from the second irregular terrain experiment are directly compared against the results of a forward dynamics simulation which finally validates the implemented rover wheel model.

7.2 Recommendations for Future Work

For future research on this topic, it is recommended to further validate the theories of the hypervolumetric planetary rover wheel model to gain more insight into the model parameters, their sensitivity and how they affect the dynamics of the rover. Ideally, a set of three separate experiments is recommended to fully understand the impact of all geometry and material parameters. These experiments are a pressure-sinkage test to verify the normal contact forces, a traction test on a single wheel to investigate the longitudinal forces, and finally, a full vehicle experiment such as the presented experiments of the Juno rover to ultimately validate the planetary rover wheel model. To obtain optimal results, the three experiments should be performed for various wheel/soil pairings where the vehicle parameters are kept the same through each set of experiments. This process will help to develop a more general tire model.

Regarding the volumetric traction model, more development of the tangential soil force model is recommended. Rather than using Hanamoto's shear stress distribution equation which has been shown to be of limited success for planetary rover simulations, a longitudinal force model based on relative contact velocity and driving speed can be developed. Inspired by the on-road tire models such as the "Magic Formula" tire, slip-based wheel soil traction models based on terramechanics theories can be developed. These tire formulations have been shown to work for HIL simulations and, considering the rather slow operating modes of a rover, such a steady-state tire modelling approach is assumed to be sufficient for this purpose.

To broaden the field of application of the developed wheel models, the implementation into a rover simulation environment in combination with Gonthier's linear volumetric contact model for hard-hard contacts is recommended. This will allow for the simulation of a rover driving on a soft soil and rigid rock composite which is a common characteristic of lunar or Martian regolith. Appropriate experiments that are required for validation have already been performed on the Juno rover.

Finally, the hypervolumetric contact models can be implemented on parallel computing systems to allow for faster simulations of more complex geometries. With the help of

graphical modelling methods and the use of contact detection algorithms similar to those used in gaming, the calculation of the volumetric properties can be performed numerically. One promising approach is volume voxelization which can be parallelized to integrate for the volume properties. These properties can then be efficiently calculated using clusters of high performance CPUs and/or high level GPUs. This will allow for the use of complex planetary rover wheel geometries in contact with any shape of rock or soft terrain material such as Martian regolith.

References

Abd El-Gawwad et al. 1999a Abd El-Gawwad, K. A. ; Crolla, D. A. ; A., Soliman A. M. ; El-Sayed, F. M.: Off-road tyre modelling I: the multi-spoke tyre model modified to include the effect of straight lugs. In: *Journal of Terramechanics* 36 (1999), pp. 3 – 24

Abd El-Gawwad et al. 1999b Abd El-Gawwad, K. A. ; Crolla, D. A. ; A., Soliman A. M. ; El-Sayed, F. M.: Off-road tyre modelling II: effect of camber on tyre performance. In: *Journal of Terramechanics* 36 (1999), pp. 25 – 38

Abd El-Gawwad et al. 1999c Abd El-Gawwad, K. A. ; Crolla, D. A. ; A., Soliman A. M. ; El-Sayed, F. M.: Off-road tyre modelling III: effect of angled lugs on tyre performance. In: *Journal of Terramechanics* 36 (1999), pp. 63 – 75

Abd El-Gawwad et al. 1999d Abd El-Gawwad, K. A. ; Crolla, D. A. ; A., Soliman A. M. ; El-Sayed, F. M.: Off-road tyre modelling IV: extended treatment of tyre-terrain interaction for the multi-spoke model. In: *Journal of Terramechanics* 36 (1999), pp. 77 – 90

Andrews and Kesavan 1973a Andrews, G. C. ; Kesavan, H. K.: The Principle of Orthogonality: A More General Form of the Prnciple of Virtual Work. In: *Proceeding of the 4th Canadian Congress of Applied Mechanics* (1973)

Andrews and Kesavan 1973b Andrews, G. C. ; Kesavan, H. K.: The Vector-Network Model: A New Approach to Vector Dynamics. In: *Mechanism and Machine Theory* 10 (1973), pp. 57 – 75

Azimi et al. 2011a Azimi, A. ; Hirschkorn, M. ; Ghotbi, B. ; Kövecses, J. ; Angeles, J. ; Radziszewski, P. ; Teichmann, M. ; Courchesne, M. ; Gonthier, Y.: Terrain modelling in simulation-based performance evaluation of rovers. In: *Canadian Aeronautics and Space Journal* 57 (2011), No. 1, pp. 24–33

Azimi et al. 2011b Azimi, A. ; Kovecses, J. ; Angeles, J.: Wheel-soil interaction model for rover simulation based on plasticity theory. In: *Intelligent Robots and Systems (IROS), 2011 IEEE/RSJ International Conference on* IEEE (Proceedings), 2011, pp. 280–285

Baciu and Kesavan 1995 Baciu, G. ; Kesavan, H. K.: From Particle-Mass to Multibody Systems: Graph-Theoretic Modeling. In: *IEEE Transactions on Systems, Man, and Cybernetics — Part A: Systems and Humans* 27 (1995), No. 2, pp. 244 – 250

Barnes et al. 2006 Barnes, D. ; Battistelli, E. ; Bertrand, R. ; Butera, F. ; Chatila, R. ; Del Biancio, A. ; Draper, C. ; Ellery, A. ; Gelmi, R. ; Ingrand, F. et al.: The ExoMars rover and Pasteur payload Phase A study: an approach to experimental astrobiology. In: *International Journal of Astrobiology* 5 (2006), No. 03, pp. 221–241

Bauer et al. 2005a Bauer, R. ; Barfoot, T. ; Leung, W. ; Ravindran, G.: Dynamic Simulation Tool Development for Planetary Rovers. In: *International Journal of Advanced Robotic Systems* 6 (2005), No. 1, pp. 311 – 314

Bauer et al. 2005b Bauer, R. ; Leung, W. ; Barfoot, T.: Experimental and Simulation Results of Wheel-Soil Interaction for Planetary Rovers. In: *Proceedings of the 1st IEEE/RSJ International Conference on Intelligent Robots and Systems — IROS* (2005)

Bekker 1960 Bekker, M. G.: *Off-The-Road Locomotion.* Ann Arbor, USA : University of Michigan Press, 1960

Bekker 1962 Bekker, M. G.: *Theory of Land Locomotion - The Mechanics of Vehicle Mobility.* Ann Arbor, USA : University of Michigan Press, 1962

Bekker 1969 Bekker, M. G.: *Introduction to Terrain-Vehicle Systems.* Ann Arbor, USA : University of Michigan Press, 1969

Biggs et al. 1998 Biggs, N. L. ; Lloyd, E. K. ; Wilson, R. J.: *Graph Theory 1736 - 1936.* Reissued paperback edition. Oxford, UK : Clarendon Press, 1998

Blundell and Harty 2004 Blundell, M. ; Harty, D.: *The Multibody Systems Approach to Vehicle Dynamics.* Oxford, UK : Elsevier Butterworth-Heinemann, 2004

Boos and McPhee 2011 Boos, M. ; McPhee, J.: Volumetric contact dynamics models and experimental validation of normal forces for simple geometries ASME (Proceedings), 2011

Boos and McPhee 2012 Boos, M. ; McPhee, J.: Friction Modelling and Validation for a Volumetric Contact Dynamics Model ASME (Proceedings), 2012

Boos and McPhee 2013 Boos, M. ; McPhee, J.: Volumetric Modeling and Experimental Validation of Normal Contact Dynamic Forces. In: *Journal of Computational and Nonlinear Dynamics* 8 (2013), pp. 021006

Boosinsuk and Yong 1984 Boosinsuk, P. ; Yong, R. N.: Soil compliance influence on tyre performance. In: *Proceedings of the 8st International Conference on Terrain-Vehicle Systems* (1984)

Chan and Sandu 2007 Chan, B.J. ; Sandu, C.: A Novel Wheel-Soil Interaction Model for Off-road Vehicle Dynamics Simulation ASME (Proceedings), 2007

Chandrashekar et al. 1992 Chandrashekar, M. ; Roe, P. ; Savage, G. J.: Graph-Theoretic Models — A Unifying Modelling Approach. In: *Proceedings of the 23rd Annual Pittsburgh Conference on Modelling and Simulation* 18 (1992), pp. 2217 – 2222

Chandrashekar and Savage 1997 Chandrashekar, M. ; Savage, G. J.: Engineering Systems: Analysis, Design and Control. In: *Course Notes, Systems Design Engineering, University of Waterloo* (1997)

Crolla and El-Razaz 1987 Crolla, D. A. ; El-Razaz, A. S. A.: A Review of the Combined Lateral and Longitudinal Force Generation of Tyres on Deformable Surface. In: *Journal of Terramechanics* 24 (1987), No. 3, pp. 199 – 225

Davis 1974 Davis, D. C.: A Radial-Spring Terrain-Enveloping Tire Model. In: *Vehicle System Dynamics* 3 (1974), pp. 55 – 69

Favaedi et al. 2011 Favaedi, Y. ; Pechev, A. ; Scharringhausen, M. ; Richter, L.: Prediction of tractive response for flexible wheels with application to planetary rovers. In: *Journal of Terramechanics* 48 (2011), pp. 199 – 213

Fervers 2004 Fervers, C. W.: Improved FEM simulation model for tire-soil interaction. In: *Journal of Terramechanics* 41 (2004), pp. 87 – 100

Ghotbi et al. 2011 Ghotbi, B. ; Azimi, A. ; Kövecses, J. ; Angeles, J.: Sensitivity Analysis of Mobile Robots for Unstructured Environments ASME (Proceedings), 2011

Gilardi and Sharf 2002 Gilardi, G. ; Sharf, I.: Literature survey of contact dynamics modelling. In: *Mechanics and Machine Theory* 32 (2002), pp. 1213–1239

Gong 1993 Gong, S.: *A Study of In-Plane Dynamics of Tires*, Delft University of Technology, The Netherlands, PhD Dissertation, 1993

Gonthier et al. 2008a Gonthier, Y. ; Lange, C. ; McPhee, J.: Using volume metrics as an alternative to penalty or finite element methods for modelling contacts. In: *Proceeding of 8th World Congress on Computational Mechanics and 5th European Congress on Computational Methods in Applied Sciences and Engineeering* (2008)

Gonthier et al. 2008b Gonthier, Y. ; McPhee, J. ; Lange, C.: On the implementation of Coulomb friction in a contact model based on volumetric properties. In: *Proceeding of ASME Design Engineering Technical Conferences and 6th International Conference on Multibody Systems, Nonlinear Dynamics and Control* (2008)

Gonthier et al. 2005 Gonthier, Y. ; McPhee, J. ; Lange, C. ; Piedboeuf, J. C.: A contact modeling method based on volumetric properties. In: *Proceeding of 2005 ASME Design Engineering Conference and 5th International Conference on Multibody Systems, Nonlinear Dynamics and Control* (2005)

Gonthier 2007 Gonthier, Yves: *Contact Dynamics Modelling for Robotic Task Simulation*, Department of Systems Design Engineering, University of Waterloo, Dissertation, 2007

Grahn 1992 Grahn, M.: Prediction of Sinkage and Rolling Resistance for Off-Road Vehicle Considering Penetration Velocity. In: *Journal of Terramechanics* 28 (1992), No. 4, pp. 339 – 347

Grecenko 1967 Grecenko, A.: Binomic Slip-Thrust Equation for Tractors on Predominantly Frictional Soils. In: *Journal of Terramechanics* 4 (1967), No. 4, pp. 37 – 54

Harnisch 2005 Harnisch, C.: *AS2TM Tire Model User's Manual*. AESCO GbR (Proceedings), 2005

Harnisch and Lach 2002 Harnisch, C. ; Lach, B.: Off road vehicles in a dynamic three-dimensional realtime simulation. In: *Proceedings of the 14th International Conference of the International Society for Terrain-Vehicle Systems* (2002)

Harnisch et al. 2003 Harnisch, C. ; Lach, B. ; Jakobs, R.: ORSIS – news and further developments. In: *Proceedings of the 9th European Conference of the International Society for Terrain-Vehicle Systems* (2003)

Harnisch et al. 2005 Harnisch, C. ; Lach, B. ; Jakobs, R. ; Troulis, M. ; Nehls, O.: A new tyre-soil interaction model for vehicle simulation on deformable ground. In: *Vehicle System Dynamics* 43 (2005), pp. 384 – 394

Haug 1989 Haug, E. J.: *Computer-Aided Kinematics and Dynamics of Mechanical Systems*. Boston : Allyn and Bacon, 1989

Hirschkorn et al. 2006 Hirschkorn, M. ; McPhee, J. ; Birkett, S.: Dynamic Modeling and Experimental Testing of a Piano Action Mechanism. In: *Journal of Computational and Nonlinear Dynamics* 1 (2006), pp. 47 – 55

Hopkins and Wilson 1997 Hopkins, B. ; Wilson, R. J.: The Truth about Königsberg. In: *The College Mathematics Journal* 27 (1997), No. 2, pp. 244 – 250

Iagnemma and Dubowsky 2004a Iagnemma, K. ; Dubowsky, S.: *Mobile robots in rough terrain: Estimation, motion planning, and control with application to planetary rovers*. Vol. 12. Springer, 2004

Iagnemma and Dubowsky 2004b Iagnemma, K. ; Dubowsky, S.: Traction control of wheeled robotic vehicles in rough terrain with application to planetary rovers. In: *The International Journal of Robotics Research* 23 (2004), No. 10-11, pp. 1029–1040

Iagnemma et al. 2004 Iagnemma, K. ; Kang, S. ; Shibly, H. ; Dubowsky, S.: Online terrain parameter estimation for wheeled mobile robots with application to planetary rovers. In: *Robotics, IEEE Transactions on* 20 (2004), No. 5, pp. 921–927

Iagnemma et al. 2011 Iagnemma, K. ; Senatore, C. ; Trease, B. ; Arvidson, R. ; Bennett, K. ; Shaw, A. ; Zhou, F. ; Van Dyke, L. ; Lindemann, R.: Terramechanics Modeling of Mars Surface Exploration Rovers for Simulation and Parameter Estimation. In: *ASME International Design Engineering Technical Conference & Computers and Information Engineering Conference IDETC/CIE 2011*, 2011

Ishigami 2008 Ishigami, G.: *Terramechanics-based analysis and control for lunar/planetary exploration robots*, Department of Aerospace Engineering, Tohoku University, Japan, PhD Dissertation, 2008

Ishigami et al. 2007 Ishigami, G. ; Miwa, A. ; Nagatani, K. ; Yoshida, K.: Terramechanics-based model for steering maneuver of planetary exploration rovers on loose soil. In: *Journal of Field Robotics* 24 (2007), No. 3, pp. 233–250

Janosi 1961 Janosi, Z.: An Analysis of Pneumatic Tire Performance on Deformable Soils. In: *Proceedings of the 1st International Conference on Terrain-Vehicle Systems* (1961)

Janosi and Hanamoto 1961 Janosi, Z. ; Hanamoto, B.: Analytical Determination of Drawbar Pull as a Function of Slip for Tracked Vehicles in Deformable Soils. In: *1st International Conference on Terrain-Vehicle Systems ISTVS, Torino, Italy*, 1961

Johnson 1985 Johnson, K. L.: *Contact Mechanics*. Cambridge, UK : Cambridge University Press, 1985

Kecskeméthy and Hiller 1994 Kecskeméthy, A. ; Hiller, M.: An object-oriented approach for an effective formulation of multibody dynamics. In: *Computer Methods in Applied Mechanics and Engineering* 115 (1994), pp. 287 – 314

Khot et al. 2007 Khot, L. R. ; Salokhe, V. M. ; Jayasuriya, H. P. W. ; Nakashima, H.: Experimental validation of distinct element simulation for dynamic wheel-soil interaction. In: *Journal of Terramechanics* 44 (2007), pp. 429 – 437

Koenig and Blackwell 1960 Koenig, H. E. ; Blackwell, W. A.: Linear Graph Theory-A Fundamental Engineering Discipline. In: *IRE Transaction on Education* 3 (1960), No. 2, pp. 42 – 49

Krenn and Hirzinger 2008a Krenn, R. ; Hirzinger, G.: Contact Dynamics Simulation for Space Robotics Applications. In: *Proceedings of the IEEE/RSJ 2008 International Conference on Intelligent Robots and Systems — IROS* (2008)

Krenn and Hirzinger 2008b Krenn, R. ; Hirzinger, G.: Simulation of Rover Locomotion on Sandy Terrain — Modeling, Verification and Validation. In: *Proceedings of the 10th Workshop on Advanced Space Technologies for Robotics and Automation — ASTRA 2008* (2008)

Li and Sandu 2007 Li, L. ; Sandu, C.: On the impact of cargo weight, vehicle parameters, and terrain characteristics on the prediction of traction for off-road vehicles. In: *Journal of Terramechanics* 44 (2007), pp. 221 – 238

Li and Sandu 2008 Li, L. ; Sandu, C.: Analysis of Wheel-Soil Interaction under Combined Slip Condition. In: *SAE Technical Paper Series* (2008), No. 2008-01-0779

Lyasko 2010 Lyasko, M.: LSA model for sinkage predictions. In: *Journal of Terramechanics* 47 (2010), No. 1, pp. 1–19

McPhee 1996 McPhee, J.: On the Use of Linear Graph Theory in Multibody System Dynamics. In: *Nonlinear Dynamics* 9 (1996), pp. 73 – 90

McPhee 1997 McPhee, J.: A Unified Graph — Theoretic Approach to Formulating Multibody Dynamics Equations in Absolute or Joint Coordinates. In: *Journal of the Franklin Institute* 334 (1997), No. 3, pp. 431 – 445

McPhee 1998 McPhee, J.: Automatic Generation of Motion Equation for Planar Mechanical Systems using the new Set of "Branch Coordinates". In: *Mechanical Machine Theory* 33 (1998), No. 6, pp. 805 – 823

McPhee 2005 McPhee, J.: *Advances in Computational Mulitbody Systems*. Chapter: Unified Modelling Theories for the Dynamics of Multidisciplinary Multibody Systems, pp. 125 – 152, Spring Science + Business Media B.V., 2005

McPhee and Redmond 2006 McPhee, J. ; Redmond, S.: Modelling multibody systems with indirect coordinates. In: *Computer Methods in Applied Mechanics and Engineering* 195 (2006), pp. 6942 – 6957

McPhee et al. 2004 McPhee, J. ; Schmitke, C. ; Redmond, S.: Dynamic Modelling of Mechatronic Multibody Systems With Symbolic Computing and Linear Graph Theory. In: *Mathematical and Computer Modelling of Dynamical Systems* 10 (2004), No. 1, pp. 1 – 23

Meirion-Griffith and Spenko 2011 Meirion-Griffith, G. ; Spenko, M.: A modified pressure-sinkage model for small, rigid wheels on deformable terrains. In: *Journal of Terramechanics* 48 (2011), pp. 149 – 255

Millard et al. 2008 Millard, M. ; McPhee, J. ; Kubica, E.: *Mulitbody Dynamics — Computational Methods and Application*. Chapter: Multi-Step Forward Dynamic Gait Simulation, pp. 25 – 44, Spring Science + Business Media B.V., 2008

Morency 2007 Morency, Kevin: *Automatic Generation of Real-Time Simulation Code for Vehicle Dynamics using Linear Graph Theory and Symbolic Computing*, Department of Systems Design Engineering, University of Waterloo, Masterthesis, 2007

MSC.Software Corp. 2005 MSC.Software Corp. (Proceedings): *ADAMS/Tire Manual*. 2005

Muegge 1996 Muegge, B. J.: *Graph-Theoretic Modelling and Simulation of Planar Mechatronic Systems*, Department of Systems Design Engineering, University of Waterloo, Master Thesis, 1996

Nakashima and Oida 2004 Nakashima, H. ; Oida, H.: Algorithm and implementation of soil-tire contact analysis code based on dynamic FE-DE method. In: *Journal of Terramechanics* 41 (2004), pp. 127 – 137

Nelson 1962 Nelson, F. C.: In-plane vibration of simply supported circular ring segment. In: *Int. J. Mech. Sci.* 4 (1962), No. 1, pp. 517–527

Nikravesh 1988 Nikravesh, P. E.: *Computer-Aided Analysis of Mechanical Systems*. Engelwood Cliffs, New Jersey : Prentice-Hall, 1988

Oida 1979 Oida, A.: Study on equation of shear stress displacement curves. In: *Report No. 5* (1979)

Onafeko and Reece 1967 Onafeko, O. ; Reece, A. R.: Soil Stresses and Deformation Beneath Rigid Wheels. In: *Journal of Terramechanics* 4 (1967), No. 1, pp. 59 – 80

Pacejka 2006 Pacejka, H. B.: *Tire and Vehicle Dynamics*. Warrendale, PA, USA : SAE Inc., 2006

Patel et al. 2010 Patel, N. ; Slade, R. ; Clemmet, J.: The ExoMars rover locomotion subsystem. In: *Journal of Terramechanics* 47 (2010), pp. 227–242

Petersen and McPhee 2010 Petersen, W. ; McPhee, J.: A volumetric contact model approach for off-road tire/soil dynamic simulation ASME (Proceedings), 2010

Petersen and McPhee 2011 Petersen, W. ; McPhee, J.: A study of volumetric contact modelling approaches in rigid tire simulation for planetary rover application. In: *International Journal of Vehicle Design* (2011)

Petersen and McPhee 2012 Petersen, W. ; McPhee, J.: Identification of volumetric wheel/soil interaction model parameters from planetary rover experiments. In: *12th European Conference on Terrain-Vehicle Systems ISTVS, Pretoria, South Africa*, 2012

Petersen et al. 2011 Petersen, W. ; Vyasarayani, C.P. ; McPhee, J.: Flexible planetary rover tire model with volumetric wheel/soil interface. In: *17th International Conference on Terrain-Vehicle Systems ISTVS, Blacksburg, Virginia, USA*, 2011

Pfeiffer and Glocker 1996 Pfeiffer, F. ; Glocker, C.: *Multibody Dynamics with Unilateral Contacts*. New York : Wiley, 1996

Pinot et al. 2012 Pinot, E. ; Naranjo, S. ; Sandu, C. ; Jayakumar, P. ; Ross, B.: Soft Soil Tire Model Development and Experimental Testing. In: *12th European Conference on Terrain-Vehicle Systems ISTVS, Pretoria, South Africa*, 2012

Pinto 2012 Pinto, E.J.: *A Three Dimensional Discretized Tire Model For Soft Soil Applications*, Virginia Polytechnic Institute and State University, Master Thesis, 2012

Reece 1965 Reece, A.R.: Principles of soil–vehicle mechanics. In: *ARCHIVE: Proceedings of the Institution of Mechanical Engineers, Automobile Division 1947-1970* 180 (1965), No. 1965, pp. 45–66

Reece 1964 Reece, R.: Theory and practice of off-the-road locomotion. In: *The Institution of Agricultural Engineers Annual Conference* (1964)

Samin et al. 2007 Samin, J. C. ; Bruls, O. ; Collard, J. F. ; Sass, L. ; Fisette, P.: Multiphysics modeling and optimization of mechatronic multibody systems. In: *Multibody System Dynamics* 18 (2007), pp. 345 – 373

Samin and Fisette 2003 Samin, J. C. ; Fisette, P.: *Symbolic Modeling of Multibody Systems*. Dordrecht, Netherlands : Kluwer Academic Publishers, 2003

Sandhu et al. 2010 Sandhu, S. ; Millard, M. ; McPhee, J. ; Brekke, D.: 3D dynamic modelling and simulation of a golf drive. In: *Procedia Engineering* 2 (2010), No. 2, pp. 3243–3248

Sandhu and McPhee 2010 Sandhu, S.S. ; McPhee, J.: A Two-Dimensional Nonlinear Volumetric Foot Contact Model ASME (Proceedings), 2010

Sass et al. 2004 Sass, L. ; McPhee, J. ; Schmitke, C. ; Fisette, P. ; Grenier, D.: A Comparison of Different Methods for Modelling Electromechanical Multibody Systems. In: *Multibody System Dynamics* 12 (2004), pp. 209 – 250

Savage 1997 Savage, G. J.: Solution of large nonlinear engineering systems through subsystems. In: *Advances in Engineering Systems* 28 (1997), pp. 247 – 258

Sayers and Han 1996 Sayers, M. W. ; Han, D.: Generic multibody vehicle model for simulating handling and braking. In: *Vehicle System Dynamics* 25 (1996), No. Suppl., pp. 599 – 613

Schäfer et al. 2010 Schäfer, B. ; Gibbesch, A. ; Krenn, R. ; Rebele, B.: Planetary rover mobility simulation on soft and uneven terrain. In: *Vehicle System Dynamics* 48 (2010), No. 1, pp. 149–169

Scharringhausen et al. 2009a Scharringhausen, M. ; Beermann, D. ; Krömer, O. ; Richter, L.: Single-Wheel Tests for Planetary Applications at DLR Bremen. In: *11th European Regional Conference of ISTVS, Bremen*, 2009

Scharringhausen et al. 2009b Scharringhausen, M. ; Beermann, D. ; Krömer, O. ; Richter, L.: A Wheel-Soil Interaction Model for Planetary Application. In: *11th European Regional Conference of ISTVS, Bremen*, 2009

Scherrer and McPhee 2003 Scherrer, M. ; McPhee, J.: Dynamic Modelling of Electromechanical Multibody Systems. In: *Multibody System Dynamics* 9 (2003), pp. 87 – 115

Schiehlen 1986 Schiehlen, W.: *Technische Dynamik*. Stuttgart, Germany : Teubner, 1986

Schimd and Ludewig 1991 Schimd, I. C. ; Ludewig, J.: Improved calculation of sinkage of a wheel on soft ground. In: *Proceedings of the 5th International Conference on Terrain-Vehicle Systems* (1991)

Schmid 1995 Schmid, I. C.: Interaction of Vehicle and Terrain Results from 10 Years at IKK. In: *Journal of Terramechanics* 32 (1995), No. 1, pp. 3 – 26

Schmitke and McPhee 2003 Schmitke, C. ; McPhee, J.: A Procedure for Modeling Multibody Systems Using Subsystem Models. In: *International Journal for Multiscale Computational Engineering* 1 (2003), No. 2, pp. 139 – 159

Schmitke and McPhee 2005 Schmitke, C. ; McPhee, J.: Forming Equivalent Subsystem Components to Facilitate the Modelling of Mechatronic Multibody Systems. In: *Multibody System Dynamics* 14 (2005), pp. 81 – 109

Schmitke and McPhee 2007 Schmitke, C. ; McPhee, J.: Using linear graph theory and the principle of orthogonality to model multibody, multi-domain systems. In: *Advanced Engineering Informatics* 22 (2007), pp. 147 – 160

Schmitke et al. 2008 Schmitke, C. ; Morency, K. ; McPhee, J.: Using graph theory and symbolic computing to generate efficient models for multi-body vehicle dynamics. In: *Journal of Multi-body Dynamics* 222 (2008), pp. 339 – 352

Schmitke 2004 Schmitke, Chad: *Modelling Multibody Multi-Domain Systems Using Subsystems and Linear Graph Theory*, Department of System Design Engineering, University of Waterloo, Dissertation, 2004

Schreiber and Kutzbach 2007 Schreiber, M. ; Kutzbach, H. D.: Comparison of different zero-slip definitions and a proposal to standardize tire traction performance. In: *Journal of Terramechanics* 44 (2007), pp. 75 – 79

Schwanghart 1968 Schwanghart, H.: Lateral Forces on Steered Tyres in Loose Soil. In: *Journal of Terramechanics* 5 (1968), No. 1, pp. 9 – 29

Seeni et al. 2010 Seeni, A. ; Schafer, B. ; Hirzinger, G.: Robot Mobility Systems for Planetary Surface Exploration–State-of-the-Art and Future Outlook: A Literature Survey. In: *Aerospace technologies advancements. Intech Publ* (2010), pp. 189–208

Senatore and Iagnemma 2011 Senatore, C. ; Iagnemma, K. D.: Direct shear behaviour of dry, granular soils for low normal stress with application to lightweight robotic vehicle modelling. In: *17th International Conference on Terrain-Vehicle Systems ISTVS, Blacksburg, Virginia, USA*, 2011

Seshu and Reed 1961 Seshu, S. ; Reed, M. B.: *Linear graphs and Electrical Networks*. Addison-Wesley, 1961 (Addison-Wesley series in the Engineering Sciences)

Shabana 1989 Shabana, A. A.: *Dynamics of Multibody Systems*. New York : Wiley, 1989

Shabana 1994 Shabana, A. A.: *Computational Dynamics*. New York : Wiley, 1994

Shi et al. 2001 Shi, P. ; McPhee, J. ; Heppler, G.: Dynamics of Flexible Multibody Systems Using Virtual Work and Linear Graph Theory. In: *Mechanical Structures & Machines* 29 (2001), No. 1, pp. 43 – 64

Shibly et al. 2005 Shibly, H. ; Iagnemma, K. ; Dubowsky, S.: An equivalent soil mechanics formulation for rigid wheels in deformable terrain, with application to planetary exploration rovers. In: *Journal of Terramechanics* 42 (2005), No. 1, pp. 1–13

Trent 1955 Trent, H. M.: Isomorphisms between oriented linear graphs and lumped physical systems. In: *Journal of the Acoustical Society of America* 35 (1955), No. 3, pp. 198 – 207

Uchida and McPhee 2007 Uchida, T. ; McPhee, J.: Dynamics Modelling and Simulation of the Centaur Skid-Steered All-Terrain Vehicle. In: *Proceedings of the CANCAM 2007* (2007)

Volpe et al. 1996 Volpe, R. ; Balaram, J. ; Ohm, T. ; Ivlev, R.: Rocky 7: A next generation mars rover prototype. In: *Advanced Robotics* 11 (1996), No. 4, pp. 341–358

Wittenburg 1977 Wittenburg, J.: *Dynamics of Systems of Rigid Bodies*. Stuttgart, Germany : Teubner, 1977

Wong 1991 Wong, J. Y.: Some recent Developments in Vehicle-Terrain Interaction Studies. In: *Journal of Terramechanics* 28 (1991), No. 4, pp. 269 – 288

Wong 1993 Wong, J. Y.: *Theory of Ground Vehicles*. New York, NY, USA : John Wiley & Sons Inc., 1993

Wong and Reece 1967a Wong, J. Y. ; Reece, A. R.: Prediction of Rigid Wheel Performance Based on the Analysis of Soil-Wheel Stresses Part I. Preformance of Driven Rigid Wheels. In: *Journal of Terramechanics* 4 (1967), No. 1, pp. 81 – 98

Wong and Reece 1967b Wong, J. Y. ; Reece, A. R.: Prediction of Rigid Wheel Performance Based on the Analysis of Soil-Wheel Stresses Part II. Preformance of Towed Rigid Wheels. In: *Journal of Terramechanics* 4 (1967), No. 2, pp. 7 – 25

Wong 1967 Wong, J.Y.: Behaviour of soil beneath rigid wheels. In: *Journal of Agricultural Engineering Research* 12 (1967), No. 4, pp. 257–269

Wong 2010 Wong, J.Y.: *Terramechanics and Off-Road Vehicle Engineering — Terrain Behaviour, Off-Road Vehicle Performance and Design*. 3rd. Elsevier Ltd., 2010

Yong and Fattah 1967 Yong, R. N. ; Fattah, E. A.: Prediction of wheel-soil interaction and performance using the finite element method. In: *Journal of Terramechanics* 13 (1967), No. 4, pp. 227 – 240

Yong and Fattah 1975 Yong, RN ; Fattah, EA: Influence of contact characteristics on energy transfer and wheel performance on soft soil. In: *5th International Conference on Terrain-Vehicle Systems ISTVS, Detroit, Michigan, USA* Vol. 2, 1975, pp. 241–310

Appendix A

Derivation of Plasticity Intersection Volume

To determine the intersection volume $V_{int,plastic}$ for a cylindrical wheel in contact with a soft plastic soil, the intersection volumes of four wheels of different sizes are numerically calculated and plotted over the soil rebound coefficient γ. The sizes vary from a wheel radius of $R = 10..30$ $[cm]$ and a wheel width of $b = 10..15$ $[cm]$. The results of this process can be seen in Figure A.1.

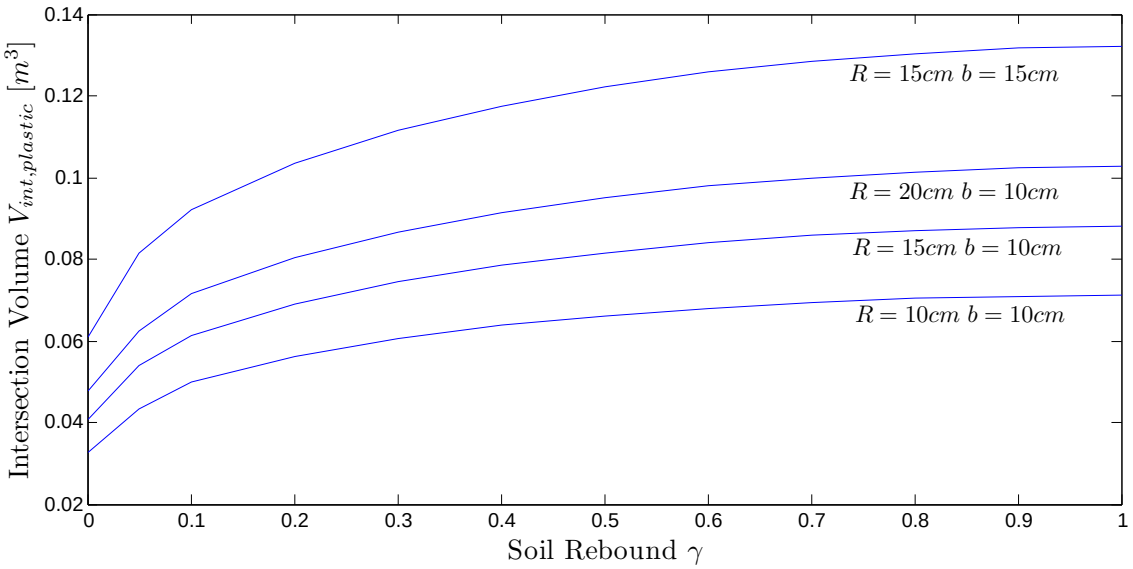

Figure A.1: Intersection volume of a wheel in contact with plastic soil

As expected, the larger the size of the wheel, the greater the intersection volume. All curves show the same characteristic behaviour with respect to the amount of soil rebound. When normalizing the plotted volume functions with the corresponding maximum intersection volume, which represents an ideal elastic soil with no rebound, the curves collapse into one function. The results can be observed in Figure A.2.

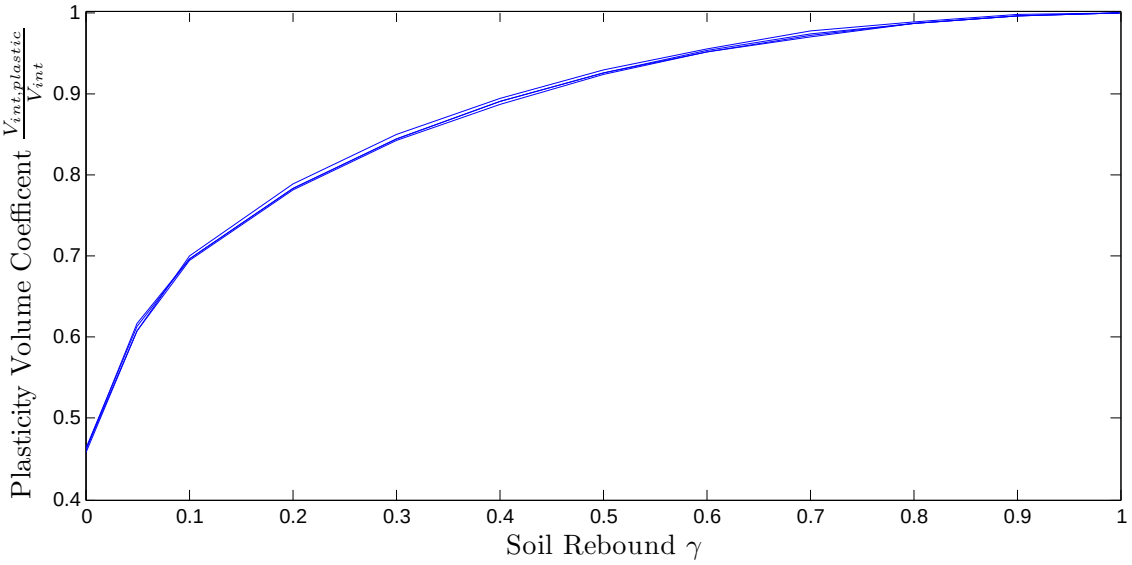

Figure A.2: Normalized intersection volume of a wheel in contact with plastic soil

This leads to the assumption that the plastic intersection volume parameter $V_{int,plastic}$ can be calculated as a function of the dimensionless soil rebound γ multiplied with the intersection volume of an ideal elastic soil V_{int} as shown in Eqn A.1. Through curve-fitting the function plotted in Figure A.2 by using the square root of the soil rebound parameter $\sqrt{\gamma}$ as the basis, the plastic intersection volume $V_{int,plastic}$ of a cylindrical wheel can be calculated with Eqn A.2.

$$V_{int,plastic} = f(\gamma)\, V_{int} \tag{A.1}$$

$$= (-0.345\gamma + 0.897\sqrt{\gamma} + 0.458)\, V_{int} \tag{A.2}$$

This curve-fit model is compared against the numerically calculated intersection volume for a plastic soil and the results can be seen in Figure A.3.

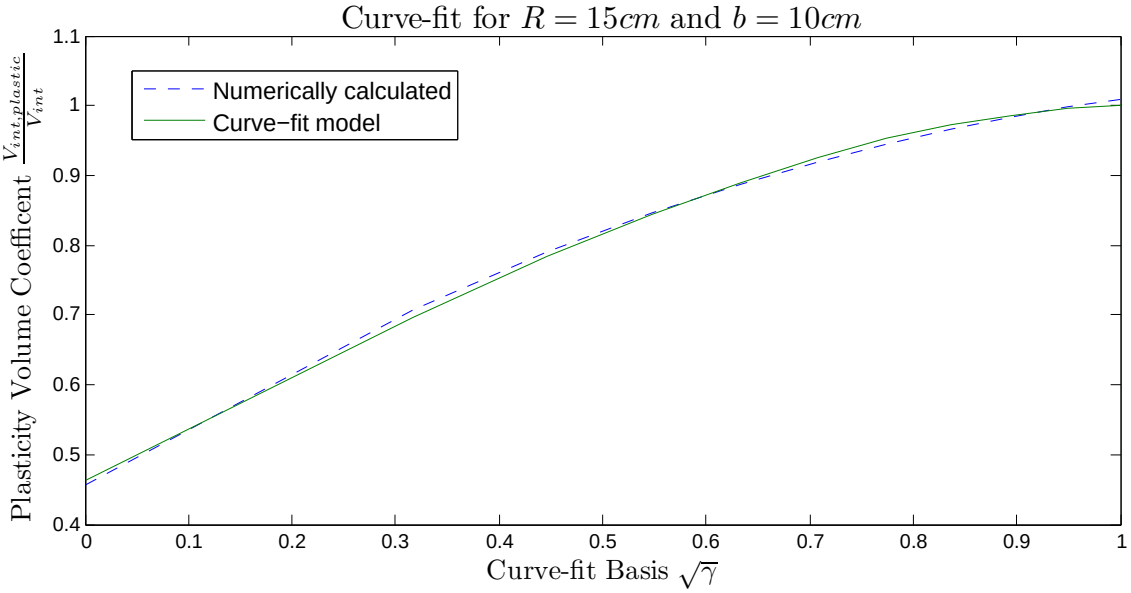

Figure A.3: Plastic intersection volume function

Appendix B

Normalized Modes of Flexible Wheel Model

A single wheel simulation is performed using both the scaled and unscaled equations of motions. The results of the unscaled system are compared against the normalized tire model to ensure that the non-dimensional model can be used to simulate the same flexible wheel system as the unscaled tire model. A driving scenario with a constant forward velocity and no slippage was simulated and the results of the first 4 mode shape coordinates can be seen in the plots of Figure B.1. The illustrated results plots show an obvious congruence between the two models, which verifies that the normalized set of equations can be used to represent equations of motion of the flexible wheel.

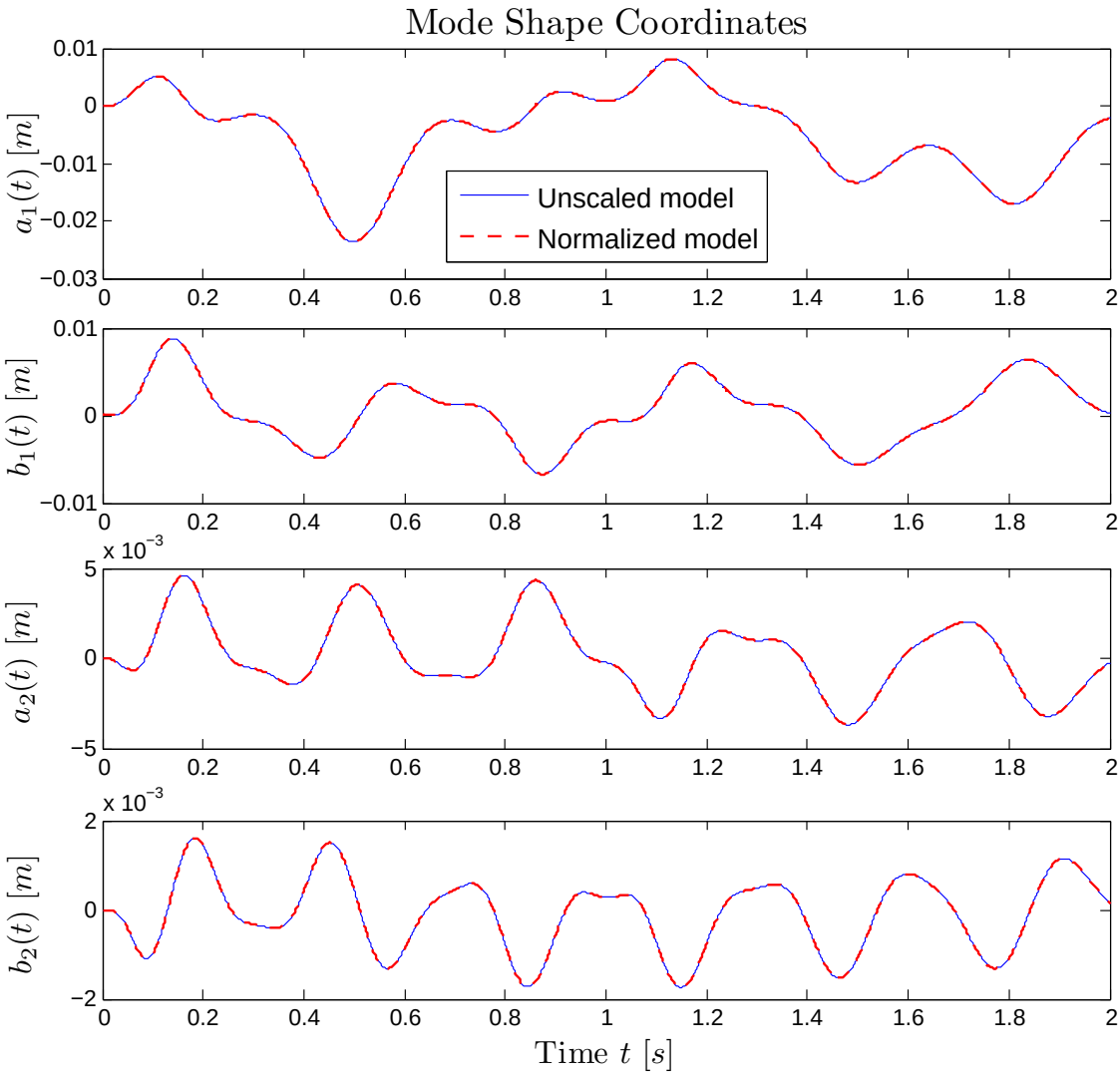

Figure B.1: Modes 1–4 of normalized and unscaled flexible tire model during single wheel simulation